High Power Solid State Single Frequency MOPA for Gravitational Wave Detection

Doctoral Thesis

Von der Fakultät für Mathematik und Physik

der Gottfried Wilhelm Leibniz Universität Hannover

zur Erlangung des Grades

DOKTOR DER NATURWISSENSCHAFTEN

-Dr. rer. nat.-

genehmigte Dissertation
von

Chandrajit Basu

M.Sc-Physics (5-year Integrated Prog. ; Indian Institute of Technology, Kharagpur),
M.Phil-Optoelectronics (University of Southampton, UK)

born on 25th June 1981 in Alipurduar, India

2012

Referent: Prof. Dr. Karsten Danzmann
Korreferent: Prof. Dr. Uwe Morgner
Tag der Promotion: 23.07.2012

To Bandhubhai (grandpa) and Dida (granny).

Abstract

The gravitational wave detectors (GWD) based on the principle of Michelson interferometer (MI) demand highly stable single frequency linearly polarized laser sources with very high TEM_{00} mode contents. Driven by the success of the state-of-the art solid state injection locked aLIGO laser systems and keeping in mind the probable further power requirements of the third generation of GWD, a scalable high power solid state single frequency master oscillator power amplifier (MOPA) system was developed and characterized within the scope of this PhD thesis.

The solid state single pass MOPA system comprises a commercial non planar ring oscillator (NPRO), a pre-amplifier system with six $Nd:YVO_4$ based stages and the main amplifier system with four identical Nd:YAG based stages. Each of the Nd:YAG amplifier stages was pumped at $\sim$ 200 W. The amplifier system was characterized at different Gaussian seed sizes (diameter $\sim$ 930 μm, $\sim$ 1500 μm and $\sim$ 1900 μm). At a seed power of $\sim$ 60 W and seed diameter of $\sim$ 1500 μm, a linearly polarized cw output power of $\sim$ 177 W at 1064 nm, with $\sim$ 83.5% TEM_{00} mode content was achieved from the MOPA system. The mode content measurements were performed using a non-confocal ring resonator based instrument. It was shown through simulations that gain saturation was not responsible for the degradation of TEM_{00} mode content in the amplifier output ($\sim$ 83.5% for a seed diameter of $\sim$ 1500 μm), as compared to that of the seed ($\sim$ 89.5%).

Noise is a critical issue for the GWD. Hence relative intensity noise (RIN) measurements were performed over a range 1 Hz-100 kHz. Variation of the amplifier output RIN with seed power was observed experimentally in both the pre-amplifier system and the amplifier system. Although the MOPA system and the injection locked aLIGO laser system are quite different in principle, the RIN characterization of the MOPA system, performed at 160 W linearly polarized output power level, showed a similar noise spectrum to that of the free running (non-stabilized) aLIGO laser system. A simulation was performed to understand the pump and seed noise transfer onto the amplifier output RIN. It was understood that the amplifier output RIN could not be attributed to the pump and seed RINs only and rather some additional sources of noise should also be taken into account and investigated further.

Thermally induced defocus and spherical aberrations in the Nd:YAG amplifier system were experimentally studied using a commercial Shack-Hartmann wavefront sensor (SHWS). A 976 nm diode laser source was used as a probe. The measurement of thermal lens power at $\sim$ 200 W of pump power was found to be in good agreement with simulations. Also, 3rd order spherical aberration was measured at different probe beam sizes. The absolute experimental Zernike spherical aberration coefficients (C_{40}) were found to be higher than the simulated values. However, the trend of variation with probe beam size matched well with the simulated trend. Using the simulated C_{40} coefficients, estimation of TEM_{00} mode contents of the aberrated beams were performed through Gaussian overlap integral calculations. Furthermore, the scaling of Zernike defocus coefficient with pupil size was correlated to the variation of thermal lens power with probe beam size. Such scaling was also verified in case of Zernike spherical aberration coefficients obtained through experiments as well as from a simulation software (LZH Rod Designer). To the best of my knowledge, the validity and significance of such scaling of Zernike coefficients with pupil size, in the context of thermal lens characterization of an end pumped Nd:YAG amplifier system have been shown for the first time.

Key words: Single frequency, Solid state, MOPA, Nd:YAG, intensity noise, aberration, TEM_{00} mode content, Zernike coefficients, pupil size scaling

Kurzzusammenfassung

Gravitationswellen-Detektoren (GWD), die auf dem Prinzip eines Michelson-Interferometers (MI) basieren, erfordern hochstabile einfrequente linear polarisierte Laserstrahlquellen mit einem sehr hohen Anteil transversal grundmodiger Strahlung. Getrieben durch den Erfolg der gegenwärtigen Lasersysteme für „advanced LIGO" (aLIGO) und unter der Annahme, dass für die dritte Generation von GWD höhere Ausgangsleistungen notwendig sein werden, wurde im Rahmen dieser Arbeit ein skalierbares einfrequentes Verstärkersystem (MOPA, Master Oscillator Power Amplifier) entwickelt und charakterisiert.

Das MOPA-System wird im Einfachdurchgang betrieben und verwendet als Master Oszillator einen kommerziellen nicht-planaren Ringoszillator (NPRO), dessen Strahlung durch einen sechsstufigen $Nd:YVO_4$ Vorverstärker und anschließend durch den Hauptverstärker transmittiert wird, welcher aus- vier identischen Nd:YAG-Kristallen besteht. Jeder dieser Nd:YAG-Kristalle wurde bei einer Leistung von etwa 200 W gepumpt. Der Verstärkeraufbau wurde für verschiedene Strahlgrößen (Durchmesser: etwa 930 µm, 1500 µm und 1900 µm) charakterisiert. Bei einer Seedleistung von etwa 60 W und einem Laserstrahldurchmesser von etwa 1500 µm wurde eine linear polarisierte Grundmode-Ausgangsleistung von 177 W mit einem TEM_{00}-Gehalt von 83,5% erreicht. Der Grundmodegehalt wurde mit einem auf einem nicht-konfokalen Ringresonator basierendem Messinstrument gemessen. Es wurde durch Simulationen gezeigt, dass die Verstärkungssättigung nicht dafür verantwortlich ist, dass der TEM_{00}-Gehalt hinter dem Verstärkerausgang (83,5% für einen Seedstrahldurchmesser von etwa 1500 µm) geringer ist als der des Seedstrahles (~ 89,5%).

Rauschen ist ein kritischer Punkt für die GWD. Daher wurde das relative Intensitätsrauschen (RIN) in einem Bereich von 1 Hz bis 100 kHz gemessen. Die Änderung des RIN bei Variation der Seedleistung wurde experimentell sowohl im Vorverstärker, als auch im Verstärkersystem beobachtet. Obwohl die MOPA-Systeme und die injektionsgekoppelten aLIGO Lasersysteme prinzipiell unterschiedlich aufgebaut sind, zeigte die RIN-Charakterisierung des MOPA-Systems bei 160 W linear polarisierter Ausgangsleistungsleistung ein ähnliches Rauschspektrum wie der freilaufende (nicht stabilisierte) aLIGO Laser. Zum Verständnis der Übertragung der Rauscheigenschaften des Pumplichtes und des Seedstrahles auf den Verstärkerausgang wurden Simulationen durchgeführt. Dabei hat sich herausgestellt, dass das RIN am Verstärkerausgang nicht ausschließlich an das Pump- bzw. Seedlichtrauschen gekoppelt ist und daher zusätzliche Rauschquellen in Betracht gezogen und weiter untersucht werden sollten.

Der thermisch induzierte Defokus und die sphärische Aberrationen im Nd:YAG-Verstärker-System wurden unter Verwendung eines kommerziellen Shack-Hartmann Wellenfront Sensors (SHWS) experimentell untersucht. Ein 976 nm Diodenlaser wurde hierfür als Teststrahl verwendet. Die gemessene Brechkraft der thermischen Linse bei einer Pumpleistung von ~ 200 W stand in guter Übereinstimmung mit den ebenfalls durchgeführten Simulationen. Die sphärischen Aberrationen dritter Ordnung wurden ebenfalls bei verschiedenen Teststrahldurchmessern vermessen. Der Wert der hier ermittelten absoluten Zernike-Koeffizienten für die sphärischen Aberrationen (C_{40}) lag höher als die simulierten Werte. Tendenziell stimmt jedoch der Trend bei Veränderung der Teststrahlgröße mit dem simulierten Trend überein. Anhand der simulierten C_{40}-Koeffizienten wurde eine Schätzung der TEM_{00}-Modeninhalte der aberrierten Strahlen vorgenommen, indem das Überlappintegral mit einem idealen Gaußstrahl berechnet wurde. Darüber hinaus wurde die Skalierung der Defokus Zernike-Koeffizienten mit der Pupillengröße korreliert mit der Veränderung der thermischen Linse bei Änderung der Teststrahlgröße. Für die Zernike-Koeffizienten der sphärischen Aberrationen wurde diese Skalierung durch Experimente, sowie Simulationen, wie sie mit Hilfe der Software „LZH Rod-Designer" durchgeführt wurden, verifiziert. Nach meinem Wissen wurde damit erstmals die Skalierung der Zernike-Koeffizienten mit der Pupillengröße im Rahmen der Charakterisierung der thermischen Linse eines endgepumpten Nd:YAG-Verstärkersystems gezeigt.

Schlüsselwörter: Einfrequent, Festkörper, MOPA, Nd:YAG, Intensitätsrauschen, Aberration, TEM_{00}-Moden Inhalt, Zernike-Koeffizienten, Pupillengröße, Skalierung

Table of contents

Ch.1 Gravitational wave detectors: importance of specialty single frequency laser sources

1.1 Introduction

Gravitational waves [1.1] are ripples in the space-time curvature, predicted by Einstein in his General Theory of Relativity. Indirect evidence for the existence of gravitational waves was established from Hulse-Taylor observations [1.2] and since then the quest for direct measurement of gravitational waves gained further momentum resulting in the creation of Michelson interferometer (MI) based modern gravitational wave detectors. At the moment, six such detectors are operating worldwide with the biggest ones under the LIGO [1.3] program managed by Caltech and MIT. Although the principle of measurement that a gravitational wave hitting the detector would create a differential strain ($\Delta L/L$) between the perpendicular arms of an MI and can be detected sounds simple, given the predicted faint strength of such strain ($\sim 10^{-20}$ or smaller [1.4]) the engineering tasks are extremely challenging. LIGO has got the biggest MI detectors ever built on earth. These LIGO detectors with 4 km long perpendicular arms are located at Hanford and Livingston, USA. Europe has got two gravitational wave detectors (GWD) under the VIRGO program [1.5] based in Italy and under the GEO 600 program [1.6] based in Germany. Japan has a detector site under the TAMA program [1.7] and there's a great possibility that another detector site will be inaugurated in near future under the LIGO-India or INDIGO program based in India [1.8].

1.2 The state-of-the art laser sources and future trends

These gravitational wave detectors require highly stable specialty laser sources. A single frequency linearly polarized laser source operating at 1064 nm, with > 165 W of power in the fundamental TEM_{00} mode was required for the state-of-the art lasers [1.9] under the Advanced LIGO (aLIGO) framework. These lasers were built here at the Laser Zentrum Hannover in collaboration with the Albert Einstein Institute (AEI), Hannover, Germany and have already been installed at the LIGO sites during 2011-2012. The single frequency injection locked solid state aLIGO lasers offer more than 200 W of linearly polarized output power [1.9].

aLIGO caters for the 2nd generation of GWD. For the 3rd generation GWD with even better sensitivity, the requirements for the lasers are not yet finalized. A good amount of information concerning future laser sources for GWD can be found in [1.10]. One possibility is that the future GWD will switch to the eye-safe 1550 nm Erbium based laser sources [1.11] operating at around hundreds of watts and essentially replace all the mirror and beamsplitter substrates with silicon which has an extremely low absorption at 1550 nm. On the other hand, to continue with the 1064 nm wavelength, roughly 1 kW of power will be required. The reason for such power scaling from the state of the art 200 W aLIGO laser systems can be explained in terms of the enhancement of signal-to-noise ratio (SNR) of the detectors. The detector shot noise is proportional to the square root of power of the laser beam (signal) concerned. Hence the signal-to-noise ratio (SNR) of a detector read-out in the shot noise limited regime will be proportional to the square root of power ($P/\sqrt{P} = \sqrt{P}$). When it comes to achieving high power levels with good beam quality, fiber lasers are often the most obvious choice. So, an Ytterbium based master oscillator power amplifier (MOPA) system [1.12] could be a leading candidate in the race for power scaling for the 3rd generation GWD. Single frequency fiber based MOPA system with more than 500 W of output power is already known from literature [1.13, 1.14]. However, to the best of my knowledge, intensity/power noise characteristics of most of these single frequency fiber based systems are not known yet, neither their long-term usability are demonstrated unlike the aLIGO laser systems.

Moreover, power scaling in the fiber based systems is often challenged by stimulated Brillouin scattering (SBS). On the other hand, given the success of the solid state aLIGO laser systems, a modular and robust solid state single frequency MOPA system can be a very promising candidate to meet the power requirements of the future GWD. Previously, a solid state zigzag master oscillator power amplifier (MOPA) system with 104 W output power at 1064 nm and 89% TEM_{00} purity was reported by Sridharan et al [1.15]. On the other hand, in a linear geometry, a fundamental mode single frequency MOPA with 64 W output power was demonstrated by Frede et al [1.16].

1.3 Contribution of this thesis

Within the scope of the PhD program, a single frequency solid state MOPA system with ~ 177 W of linearly polarized output power at 1064 nm and >83.5% TEM_{00} mode content was built, as a scalable alternative to the injection locked laser approach adapted in the aLIGO laser systems. The MOPA system utilizes a commercial (Innolight Mephisto^{TM}) non-planar ring oscillator as the single frequency master oscillator source with 2 W of output power. A pre-amplifier system with six $Nd:YVO_4$ based stages was built to scale up the seed power further to maximize power extraction from the main amplifier system having 4 Nd:YAG based stages. The pre-amplifier system and the main amplifier system are discussed in details in chapter 2 and chapter 3 respectively. To investigate the influence of spatially varying gain on the beam quality of a Gaussian beam, a simulation is presented in chapter 3 along with the experimental results on amplifier gain characterization.

The relative intensity noise (RIN) of the MOPA system was thoroughly characterized and discussed in details in chapter 4. The MOPA output RIN has been compared to that of the free running (non-stabilized) aLIGO laser system (see Fig. 4.7). A simulation of RIN transfer from both the seed and pump light sources onto the amplifier output is presented, based on the mathematical approach demonstrated in [1.17], with necessary modifications for a 4-level system.

Unlike the optical fibers, low surface area to volume ratio in solid state active media makes solid state systems more prone to thermal issues degrading the beam quality. Thermal lensing in the Nd:YAG system was studied experimentally and theoretically. Some simulations were performed using the *LZH Rod Designer (LRD) software* [1.18]. The adverse impact of primary spherical aberration on beam quality is discussed both in terms of experiments and simulations in chapter 5.

Finally, the concluding remarks on the thesis and some possible directions for future works are presented in chapter 6.

A list of publications is included at the end.

References Ch. 1

1.1) Web resource: http://www.einstein-online.info/spotlights/gravWav

1.2) Web resource: http://space.mit.edu/LIGO/more.html

1.3) Web resource: http://www.ligo.caltech.edu/

1.4) D Coyne, "Precision Engineering in the Laser Interferometer Gravitational-wave Observatory (LIGO)," Proceedings of the 2nd German-American Frontiers of Engineering Symposium, sponsored by the National Academy of Engineering, Univ. of California, Irvine, April 8-10, 1999 (LIGO-P990006-00-D)

(File URL: http://www.ligo.caltech.edu/docs/P/P990006-00.pdf)

1.5) URL: http://www.ego-gw.it/virgodescription/

1.6) URL: http://www.geo600.org/

1.7) URL: http://tamago.mtk.nao.ac.jp/spacetime/home_e.html

1.8) URL: http://www.gw-indigo.org/tiki-index.php

1.9) L Winkelmann, O Puncken, R Kluzik, C Veltkamp, P Kwee, J Poeld, C Bogan, B Willke, M Frede, J Neumann, P Wessels and D Kracht, "Injection-locked single-frequency laser with an output power of 220W," Applied Physics B, Vol. **102**, 2011, p 529–538

1.10) N Mavalvala, D E McClelland, G Mueller, D H Reitze, R Schabel, B Willke, "Lasers and optics: looking towards third generation gravitational wave detectors," General Relativity and Gravitation **43**, 2011, p 569-592

1.11) V Kuhn, D Kracht, J Neumann and P Weßels, "Er-doped photonic crystal fiber amplifier with 70 W of output power," Optics Letters, Vol. **36**, 2011, p 3030-3032

1.12) M Karow, C Basu, D Kracht, J Neumann and P Weßels, "TEM$_{00}$ mode content of a two stage single-frequency Yb-doped PCF MOPA with 246 W of output power," Optics Express, Vol. **20**, 2012, p 5319-5324

1.13) C Zhu, I-N Hu, X Ma and A Galvanauskas, "Single-frequency and single-transverse mode Yb-doped CCC fiber MOPA with robust polarization SBS-free

511W output," Advanced Solid-State Photonics (ASSP), OSA Technical Digest (CD) (Optical Society of America, 2011), paper AMC5

1.14) C Robin, I Dajani, C Zeringue, B Ward and A Lanari, "Gain-tailored SBS suppressing photonic crystal fibers for high power applications," Proceedings of SPIE 8237, 82371D (2012)

1.15) A K Sridharan, S Saraf, S Sinha and R L Byer, "Zigzag slabs for solid-state laser amplifiers: batch fabrication and parasitic oscillation suppression," Applied Optics, Vol. **45**, 2006, 3340-3351

1.16) M Frede, B Schulz, R Wilhelm, F Seifert, P Kwee, B Willke, D Kracht, "Fundamental mode, single-frequency laser amplifier for gravitational wave detectors," Optics Express, Vol. **15**, 2007, 459-465

1.17) S Novak and A Moesle, "Analytic model for gain modulation in EDFAs; Journal of Lightwave Technology," Vol. **20**, 2002, p 975-985

1.18) R Wilhelm, D Freiburg, M Frede, D Kracht and C Fallnich, "Design and comparison of composite rod crystals for power scaling of diode end-pumped Nd:YAG lasers," Optics Express, Vol. 17, 2009, p 8229-8236

Ch.2 The master oscillator and pre-amplifier stages

2.1 Introduction

The contemporary gravitational wave detectors (GWD) require high power single frequency linearly polarized laser sources operating at 1064 nm. Since it is not easy to have a single frequency oscillator delivering a high power output, the easiest and commonest option is to use a master oscillator power amplifier (MOPA) scheme where the master or seed source is a single frequency oscillator followed by pre-amplifier and amplifier stages. The state-of-the-art injection locked aLIGO laser system [2.1] is a multi-stage system comprising a single frequency master oscillator source, a pre-amplifier and a high power oscillator which is a slave laser frequency-locked to the single frequency master oscillator source. This thesis work is based on the investigation on a MOPA system consisting of a single frequency master oscillator source, a 6-stage Nd:YVO$_4$ based pre-amplifier system and a 4-stage Nd:YAG based amplifier system, as an alternative to the injection locked aLIGO laser system architecture.

In this chapter, the non-planar ring oscillator (NPRO) based single frequency master oscillator source and the Nd:YVO$_4$ based pre-amplifier stages will be discussed. For the GWD applications so far, only the fundamental TEM$_{00}$ mode of a laser beam is usable. Hence, apart from laser power scaling, one has to keep in mind how much power is available in the TEM$_{00}$ mode. So, the TEM$_{00}$ mode content of the NPRO and the pre-amplifier output will be reported as an essential part of this chapter.

2.2 The Non-planar ring oscillator as the master source

A commercial (Innolight Mephisto[TM]) monolithic NPRO [2.2] was used as the master oscillator source in the MOPA system concerned. The output power could be controlled by changing the driving current. The centre frequency was thermally tunable (~ 30 GHz). At the standard operating point, 2 W of output power at 1064 nm was available from this NPRO with a very narrow linewidth <1 kHz (FWHM) [2.3].

It should be noted that the stability of any NPRO system is very sensitive to optical feedback or back reflections and hence it was used in a feedback protected optical configuration with 1 quarter-wave plate, 2 half-wave plates and a Faraday isolator (FI) as shown in Fig. 2.1 below.
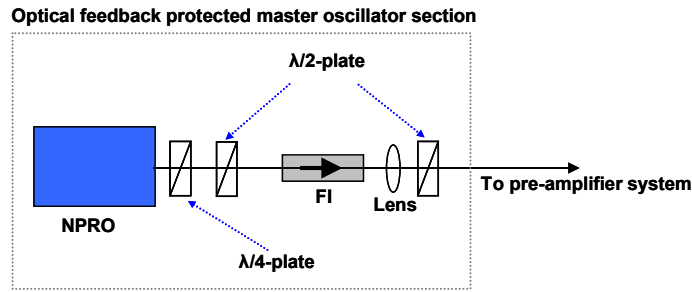

Fig. 2.1 The NPRO with feedback protection optics

It should be noted here that the mode content measurements mentioned in this thesis were performed using a very specialized instrument [2.4] based on a non-confocal ring resonator with three mirrors. This instrument is known as 'Dynamic breadboard -light (version)' and will be referred to as DBBL from hereafter. One of the mirrors is attached to a piezo actuator which changes the resonator length in order to scan for the eigenmodes of the cavity, within one full Free Spectral Range (FSR). The TEM_{00} mode content is computed in the system depending on the relative power of the different eigenmodes transmitted through the ring cavity.

The output from the feedback protected master oscillator section was characterized and found to have only ~ 3% higher order modes. In other words, this beam had roughly 97% TEM_{00} mode content and that was in excellent agreement with previous measurements [2.5]. Fig. 2.2 shows this transverse mode scan over the

full spectral range (FSR). The normalized intensity is presented in logarithmic scale (vertical) for better clarity. The fundamental mode is shown as dominant peaks at 0-FSR and 1- FSR and the higher order modes are shown in between the fundamental mode peaks.
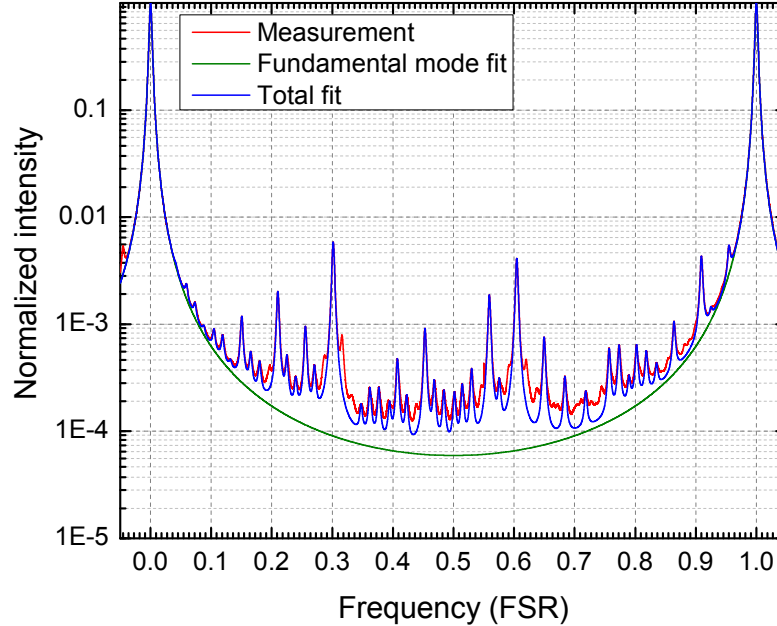

Fig. 2.2 The transverse mode scan (~ 97% TEM_{00} mode content) of the master oscillator source

2.2 The Nd:YVO$_4$ based pre-amplifier system

As compared to fiber amplifiers, very large mode sizes in typical rod type solid state amplifiers demand for high seed power levels to operate at the saturation regime. Hence, it was clear from the beginning that in order to maximize the power extraction from the Nd:YAG amplifier stages (described in chapter 3), pre-amplifier stages offering tens of watts were inevitably required for the MOPA system.

For the pre-amplifier system, Nd:YVO$_4$ crystals were the obvious choice as the active media for a couple of reasons. Nd:YVO$_4$ is naturally birefringent (positive uniaxial) and thermally induced birefringence or depolarization loss is avoidable while maintaining high purity linear polarization in the π-direction [2.6]. Furthermore, Nd:YVO$_4$ has a large emission cross-section (σ_e) for radiation at 1064 nm. Although

the effective flouorescence lifetime (τ_f) is short (~ 90 μs), the product $\sigma_e \cdot \tau_f$ is still larger than that of Nd:YAG and hence Nd:YVO$_4$ offers a lower pump threshold power for CW operation as compared to that of Nd:YAG. Moreover, through years of research on Nd:YVO$_4$ based amplifiers and laser systems at the Laser Zentrum Hannover [2.5], critical technical insight and resources were readily available.

The relevant energy level diagram of Nd:YVO$_4$ is shown in Fig. 2.3 and the most important optical and physical parameters of Nd:YVO$_4$ with Nd^{3+} doping concentration of 1 at. % are listed with widely circulated values in Table 2.1 [2.6-2.8]. However, a range of values for absorption and emission cross-sections is available in literature [2.6-2.9], especially with temperature dependent variation [2.10, 2.11]. It should be noted that in spite of having excellent optical properties outshining Nd:YAG, unfortunately Nd:YVO$_4$ is unsuitable for the high power amplifier stages due to its low thermal conductivity.
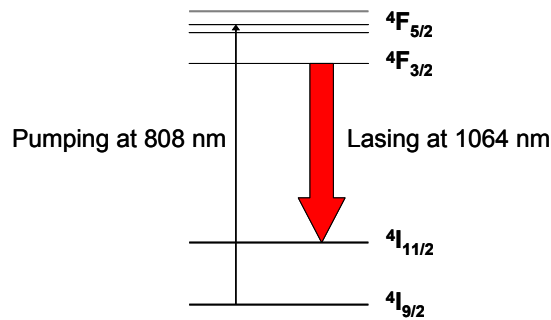

Fig. 2.3 Energy level diagram for pumping at 808 nm and lasing at 1064 in Nd:YVO$_4$

Properties/parameters	Values/description
Crystal structure	Tetragonal
Birefringence	Positive uniaxial
Thermal conductivity (K)	~ 5 W/ m-K
Melting point	1810 °C
Peak pump absorption at (λ_P)	~ 808.5 nm
Laser wavelength (λ_L)	~ 1064.3
Gain bandwidth (Δv_g)	~ 1 nm
Fluorescence lifetime (τ_f)	~ 90 μs
Pump absorption cross-section at 808 nm	60×10^{-20} cm^2
Emission cross section at 1064 nm	250×10^{-20} cm^2

Table 2.1 Some optical and physical parameters of Nd:YVO$_4$ crystal

The pre-amplifier system is schematically shown in Fig. 2.4. It comprises six Nd:YVO$_4$ based stages divided into block A & block B (shown in dotted rectangles in Fig. 2.4). All the Nd:YVO$_4$ crystals are identical. Each of them has 3 mm x 3 mm cross-sections and is 10 mm in length, with 8 mm of it being doped (0.3 at. %) and the rest 2 mm being an undoped end cap [2.5] as shown in Fig. 2.5. Note that the undoped endcaps on both Nd: Nd:YVO$_4$ and Nd:YAG crystals help reduce thermal stress induced bulging of the end facets concerned [2.12]. These Nd:YVO$_4$ crystals are sidewise wrapped in 500 μm thick indium foils and enclosed by water cooled copper blocks.
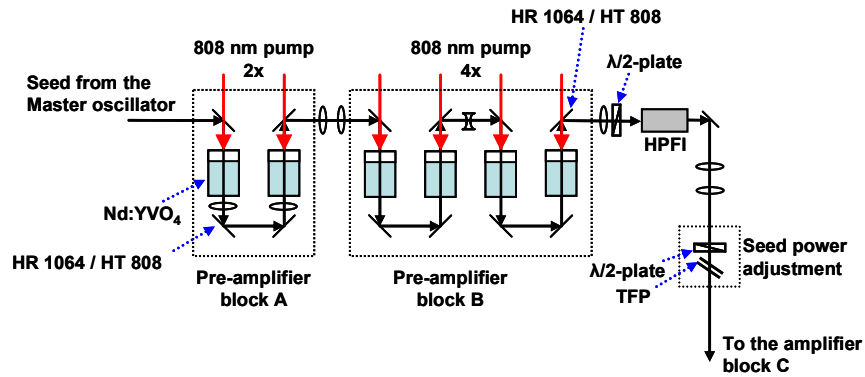
Fig. 2.4 Schematic diagram of the pre-amplifier system
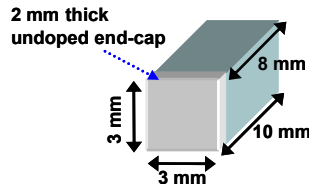
Fig. 2.5 The Nd:YVO$_4$ crystal geometry

Pre-amplifier block A comprises two Nd:YVO$_4$ based stages which were pumped at ~ 33 W and ~ 41 W by individual 808 nm diode laser modules (JENOPTIK JOLD-45-CPXF-1L) coupled to 400 μm (core diameter) fibers. In block A, the pump spot size was ~ 500 μm in diameter for both the crystals.

In pre-amplifier block B, four Nd:YVO$_4$ stages in series are pumped at 50-60 W level by individual fiber (400 μm core diameter) coupled 808 nm diode laser

modules (JENOPTIK JOLD-75-CPXF-2P). In block B, the pump spot size is ~ 600 µm in diameter for all the crystals. The pump spot size was ~ 600 µm in diameter for all the four crystals. Note that in the given geometry, different pump spot sizes between 600 µm to 800 µm could have been used [2.5]. However, at the very first attempt good output power with good beam quality was obtained with the ~ 600 µm pump spot diameter and hence no further variation in the pump optics was pursued.

All the pump diode modules in the pre-amplifier system were water-cooled. Furthermore, since the aforementioned diode modules come with in-built Peltier elements (PTC 100/1000), precise temperature control ($\Delta T \approx \pm 0.1\ ^oC$) could be achieved with external current drivers. So, through temperature tuning of the peak pump wavelength in individual diode modules, output power of the pre-amplifier system as well as that of the Nd:YAG based amplifier system could be optimized. Note that the diode modules were custom designed to offer a linewidth, $\Delta \lambda_p \leq 2.5$ nm (FWHM) around the peak wavelength.

The seed spot size for all the stages in the pre-amplifier system was experimentally adjusted for optimum beam quality and maximum power gain. With reference to the detailed investigation reported in [2.5], it can be stated that for the given Nd:YVO$_4$ crystals, at a pump power of 45 W and pump spot diameter of 600 µm, the saturation power for a seed beam of 400 µm diameter would be roughly 1.5 W. Hence it is clear that the pre-amplifier system described here was operated at the saturation regime. It should be noted that the direction of the seed beam, either co-propagating or counter-propagating with the pump beam, depends on the position of the individual stage and beam steering (horizontal) in the series architecture of the system. The whole pre-amplifier system was protected by a high power Faraday isolator (HPFI) in order to avoid optical feedback or back reflections from the subsequent amplifier system (block C- not shown here). The seed power to block C could be adjusted with a polarizing attenuator made of a half-wave plate and a thin film Brewster polarizer (TFP), in order not to change the beam parameters for the main amplifier.

Roughly 18.5 W of linearly polarized output power with ~ 90.6% TEM_{00} mode content was generated from pre-amplifier block A. The mode scan is shown in Fig. 2.6.

Fig. 2.6 Transverse mode scan (~ 90.6% TEM_{00} mode content) of the 18.5 W linearly polarized output from pre-amplifier block A

After the installation of pre-amplifier block B, the optimum linearly polarized output power obtained from it was ~ 72 W with ~ 89.5% TEM_{00} mode content. The mode scan is shown in Fig. 2.7 and the beam profile observed on a CCD camera is shown in the inset. From the above mentioned values, the estimated power in TEM_{00} mode was 72 x 0.895 W ~ 64.4 W and that was slightly higher than the estimated ~ 60.8 W of power in the TEM_{00} mode, out of a total output power of 66 W (with ~ 92.2 % TEM_{00} mode content), which had been previously observed in a similar system, at the Laser Zentrum Hannover [2.13].
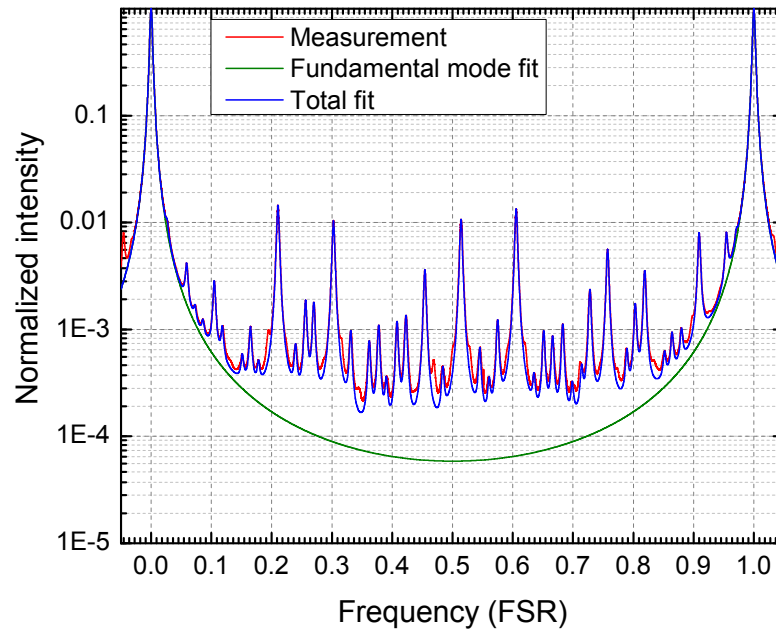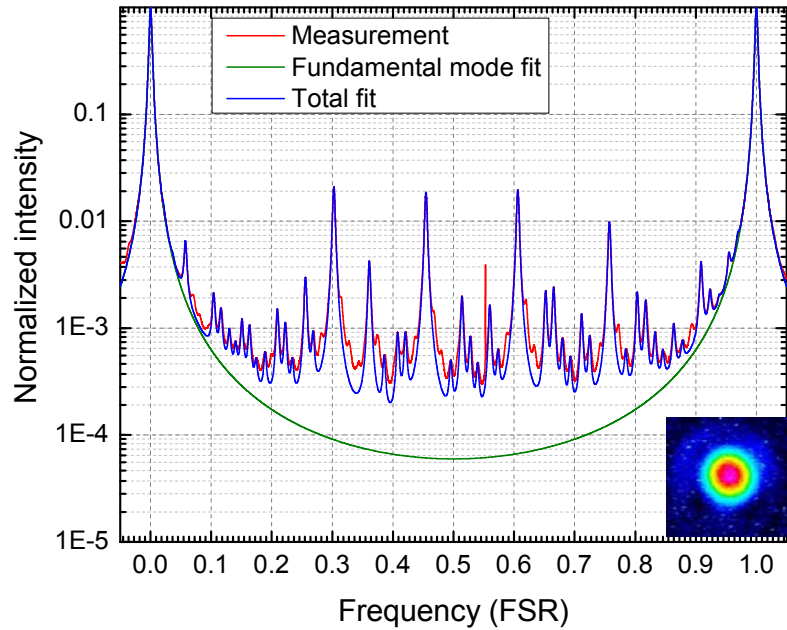
15

Fig. 2.7 Transverse mode scan (~ 89.5% TEM_{00} mode content) of the 72 W linearly polarized output from pre-amplifier block B

2.3 Conclusions

Use of an NPRO with 2W of output power at 1064 nm as the single frequency master oscillator for the MOPA system has been reported in this chapter. The necessity of a pre-amplifier stage for the MOPA system has been briefly explained. The choice of $Nd:YVO_4$ as the active media for the pre-amplifier system has been justified due to excellent optical properties. Furthermore, the design of the $Nd:YVO_4$ based multi-stage pre-amplifier system, divided into block A and block B, has been described in details. Although all the six $Nd:YVO_4$ crystals were identical, the block A with 2x stages and block B with 4x stages were distinguishable primarily due to different pump power levels. The pre-amplifier block A with 2x $Nd:YVO_4$ based stages offered 18.5 W of linearly polarized output with ~ 90.6% TEM_{00} mode content. The optimum linearly polarized output power from the overall pre-amplifier system, with 6x $Nd:YVO_4$ based stages, was 72 W with ~89.5 % TEM_{00} mode content. It was observed that the addition of block B caused roughly 1% further beam quality degradation while enhancing the output power to roughly 4 fold.

References Ch. 2

2.1) L Winkelmann, O Puncken, R Kluzik, C Veltkamp, P Kwee, J Poeld, C Bogan, B Willke, M Frede, J Neumann, P Wessels and D Kracht, "Injection-locked single-frequency laser with an output power of 220W"; Applied Physics B, Vol. **102**, 2011, p 529–538

2.2) T J Kane and R L Byer, "Monolithic, unidirectional single-mode ring laser", Optics Letters, Vol. **10**, 1985, p 65-67

2.3) Web-resource: (Datasheet-Innolight Mephisto^{TM} product line), URL: http://www.innolight.de/fileadmin/user_upload/produktblatt_pdf/Produktblatt_Mephisto.pdf

2.4) P Kwee, F Seifert, B Willke and K Danzmann, "Laser beam quality and pointing measurement with an optical resonator," Review of Scientific Instruments, Vol. **78**, 2007, p 073103-1-10

2.5) M Frede, B Schulz, R Wilhelm, F Seifert, P Kwee, B Willke and D Kracht, "Fundamental mode, single-frequency laser amplifier for gravitational wave detectors," Optics Express, Vol. **15**, 2007, p 459-465

2.6) W Koechner, "Solid-state Laser Enginnering", 6th Edition, Published by Springer, 2010, ISBN-10: 1441921176

2.7) Web resource: Encyclopedia of Laser Physics and Technology, URL: http://www.rp-photonics.com/vanadate_lasers.html

2.8) Y F Chen and Y F Lan, "Comparison between *c*-cut and *a*-cut Nd:YVO4 lasers passively Q-switched with a Cr^{4+}:YAG saturable absorber", Applied Physics B, Vol. **74**, 2002, p 415–418

2.9) Y Sato and T Taira, "Comparative Study on the Spectroscopic Properties of $Nd:GdVO_4$ and $Nd:YVO_4$ With Hybrid Process", IEEE Journal of Selected Topics in Quantum Electronics, Vol. **11**, 2005, p 613-620

2.10) G Turri, H P Jenssen, F Cornacchia, M Tonelli and M Bass, "Temperature-dependent stimulated emission cross section in Nd^{3+}:YVO_4 crystals", Journal of the Optical Society of America B, Vol. **26**, 2009, p 2084-2088

2.11) X Délen, F Balembois and Patrick Georges, "Temperature dependence of the emission cross section of Nd:YVO4 around 1064 nm and consequences on laser operation", Journal of the Optical Society of America B, Vol. **28**, 2011, p 972-976

2.12) M Tsunekane, N Taguchi, T Kasamatsu and H Inaba, "Analytical and Experimental Studies on the Characteristics of Composite Solid-State Laser Rods in Diode-End-Pumped Geometry," IEEE Journal of Selected Topics in Quantum Electronics, Vol. **3**, 1997, p 9-18

2.13) As known from Mr. B. Schulz, Laser Zentrum Hannover, through internal communication.

Ch.3 Nd:YAG based high power amplifier system

3.1 Introduction

In the solid state laser (SSL) domain, Nd:YAG is perhaps the most widely used active medium. Since the first demonstration [3.1] of tungsten lamp pumped CW operation of Nd:YAG in 1964, Nd:YAG lasers have evolved a lot for a wide range of industrial as well as medical applications. These crystals come in various form factors and can be pumped by lamps or modern diode lasers with side-pumped or end-pumped configurations. Taking advantage of a 4-level scheme, the most common lasing line is at 1064 nm, while being pumped at 808 nm. Direct upper band pumping at 885 nm for reducing quantum defect and thermal load is also well known [3.2]. Apart from the 1064 nm, Nd:YAG lasers lines at 946 nm [3.3], 1123 nm [3.4], 1319 nm [3.5], 1338 nm [3.6], 1415 nm [3.7] and 1444 nm [3.8] are also known. However, maintaining relevance to the topic of this thesis, further discussions will be limited to the application of CW Nd:YAG lasers in GWD.

In the Michelson interferometer (MI) based gravitational wave detectors, the signal to noise ratio (SNR) varies with the square root of the laser power, as discussed in sec. 1.2. Since 1064 nm was chosen as the laser wavelength for the early stage and contemporary GWDs, the demand for further power scaling, with Nd^{3+} doped crystals, became inevitable in order to enhance the SNR in the shot noise limited regime. The most obvious choice was $Nd:YVO_4$ based laser or amplifier systems. However, due to poor thermal conductivity of $Nd:YVO_4$, power scaling beyond 100 W while maintaining good beam quality was extremely challenging. Hence, with the aLIGO project aiming for a single frequency laser with > 165 W output power with >95% in

the fundamental TEM_{00} mode [3.9], Nd:YAG based laser/amplifier systems were the most promising alternatives.

Working along that direction, Frede et al. demonstrated a single frequency injection-locked 2-stage Nd:YAG laser system with 87 W of linearly polarized output power and diffraction limited beam quality [3.10] in 2003. With the addition of two more identical Nd:YAG stages, a ring laser was built and 213 W of linearly polarized output power with near diffraction limited beam quality was reported in 2005 [3.11]. This formed the basis for the high power 4-stage aLIGO laser systems [3.9] which evolved through various opto-mechanical design modifications over the years and have been recently (2011-2012) installed at the LIGO sites in the USA.

As an alternative to the injection locked aLIGO laser system, investigation on a MOPA architecture was pursued as the major part of this thesis work. This chapter will focus on the final section of the MOPA with 4x Nd:YAG based amplifier stages.

The optical and physical properties of Nd:YAG will be briefly covered first. Next, the opto-mechanical design of the amplifier stages will be described. The effective pump-spot determined by the integrated fluorescence measurement will be discussed [3.12]. Thermally induced birefringence and its compensation will be shown, both theoretically and experimentally. Most importantly, the amplifier output power and beam quality characterization for different seed sizes will be presented. A simple simulation to estimate beam quality degradation due to gain saturation will also be described. Note that beam quality degradation due to thermally induced optical aberrations will be covered in Ch.5.

3.2 Nd:YAG as an active medium

In Yttrium aluminum garnet ($Y_3Al_5O_{12}$) or YAG typically up to 1% of the Y^{3+} ions can be replaced by Nd^{3+} [3.13, 3.14]. YAG is a hard material and has an optically isotropic cubic lattice structure. The cubic lattice structure is beneficial for having a narrow fluorescent linewidth and as a result it has a high gain and low threshold for lasing [3.13]. Furthermore, high thermal conductivity (K) of YAG makes Nd:YAG one of the most suitable active media for high power CW SSL. The

energy level diagram of Nd:YAG is shown in Fig. 3.1. Apart from the relevant pumping at 808 nm ($^4I_{9/2} \rightarrow {}^4F_{5/2}, {}^2H_{9/2}$) and lasing at 1064 nm ($^4F_{3/2} \rightarrow {}^4I_{11/2}$), the other transition lines are blurred (grey).
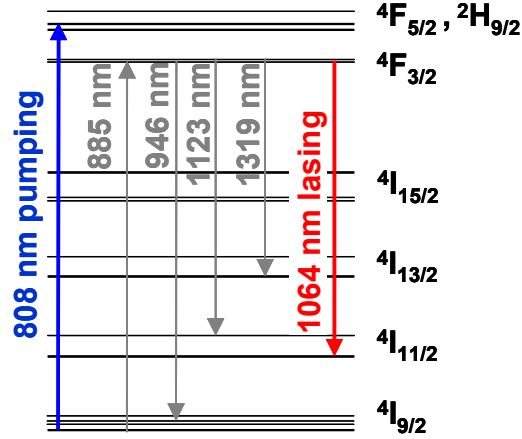
Fig. 3.1 Energy level diagram of Nd:YAG

Note that all the Nd:YAG crystals used in the MOPA system under consideration are doped at 0.1 at. %. The fluorescent spectra from one of those crystals under 808 nm pumping are shown in Fig. 3.2 (a) & 3.2 (b) for different scanning ranges on the ANDO-AQ 6317C optical spectrum analyzer. Incidentally these fluorescent spectra were measured at the throughput of a 4f imaging telescope with ARHS 1064 coated lenses, while setting up the aberration characterization experiment mentioned in Ch.5.

Fig. 3.2 Nd:YAG fluorescence spectra under 808 nm pump, range (a) 800-975 nm, (b) 1040-1090 nm

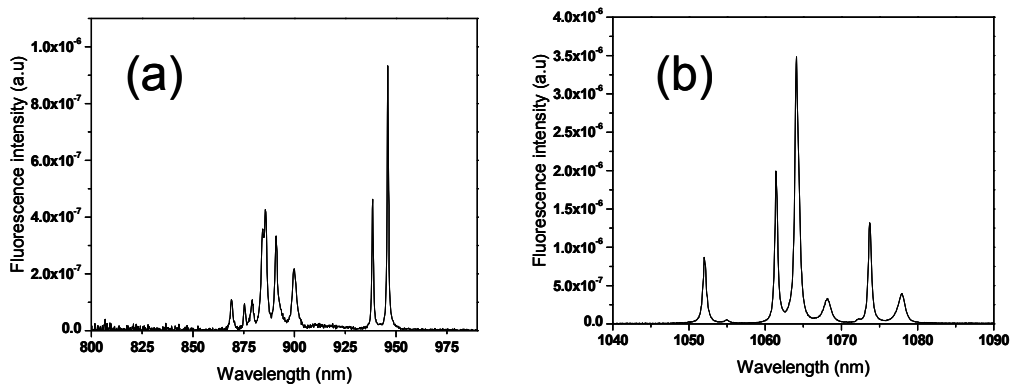The most important optical and physical properties of Nd:YAG are listed in Table 3.1 [3.13, 3.14]. Again, a range of values for the emission cross section and fluorescence lifetime are available in literature [3.15-3.18].

Properties/parameters	Values/description
Crystal structure	Cubic
Birefringence	None
Thermal conductivity (K)	~ 10-14 W/ m-K
Melting point	1970 °C
Typical pump wavelengths (λ_P / nm)	~ 808 , 885 etc.
Laser wavelength (λ_L / nm)	~ 1064, 946, 1123, 1319 etc.
gain bandwidth ($\Delta\lambda_g$)	~ 0.6 nm
Fluorescence lifetime (τ_f)	~ 230 μs
Pump absorption cross-section at 808 nm	7.7×10^{-20} cm^2
Emission cross section at 1064 nm	28×10^{-20} cm^2
Refractive index (at 1 μm)	1.82
Thermal expansion coefficient [111-orientation]	7.8×10^{-6} °C $^{-1}$ for 0–250 °C
Thermal expansion coefficient [110-orientation]	7.7×10^{-6} °C $^{-1}$ for 10–250 °C
Thermal expansion coefficient [100-orientation]	8.2×10^{-6} °C $^{-1}$ for 0–250 °C

Table. 3.1 Some important optical and physical properties/parameters of Nd:YAG

Since Nd:YAG is not naturally birefringent, thermally induced birefringence in Nd:YAG is a big challenge for laser/amplifier designers. This topic will be addressed in details in sec 3.5 of this chapter.

3.3 The opto-mechanical design of the amplifier stages

As stated before, the main high power amplifier system or block C is made of four Nd:YAG based stages. The setup of one of these stages is shown in Fig. 3.3.
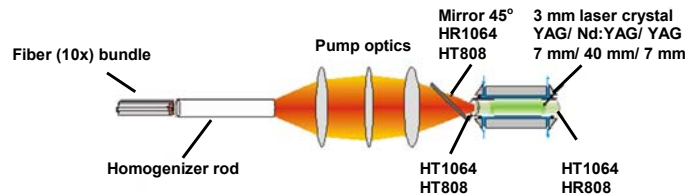

Fig. 3.3 Schematic design of one of the Nd:YAG stages

All the Nd:YAG crystals (0.1 at. %, [111]-cut) in block C are identical, having a rod geometry with 3 mm diameter and a 40 mm long doped segment between two 7 mm long undoped YAG end caps, as shown in Fig. 3.4.
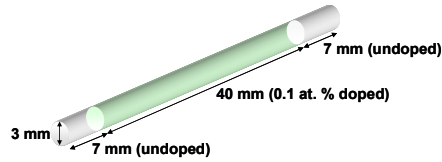

Fig. 3.4 The rod type Nd:YAG crystal

These Nd:YAG crystals are longitudinally pumped and their respective end facets (exit facets for the seed beam) are coated for high reflectivity at 808 nm and hence double pass of the 808 nm pump light. Both the entry and exit facets of the crystals are anti-reflection (AR) coated for 1064 nm. The Nd:YAG crystals are kept in custom designed water cooled chambers as shown in Fig. 3.5. The SolidWorks^{TM} 3D drawings were kindly provided by Mr. Raphael Kluzik at the LZH. The pump light is guided in the crystals due to total internal reflection at the lateral interface with water. The coolant temperature was set at $\sim$ 18 ^{o}C.
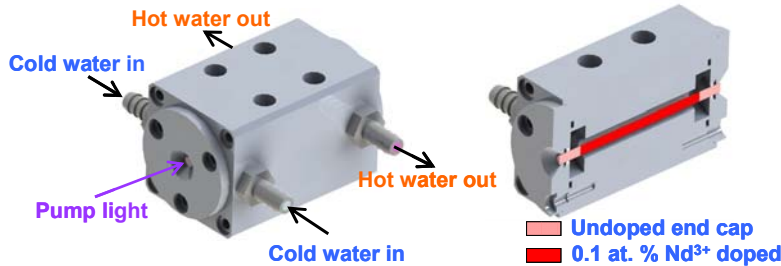
Fig. 3.5 3D design schematics of the pump chamber along with vertical cross sectional view

In every crystal, the opposite end to the pumped surface is coated for high reflectivity at 808 nm in order to enhance the pump light absorption from 159 W to 188.5 W for a pump power of 200 W and the given pump distribution, as simulated by the *LZH Rod Designer* (LRD) software. Simulation also showed that 'double pass' of the pump beam within the 0.1 at. % doped crystal would create a maximum of $\sim$ 33 ^{o}C difference in temperature across the rod axis whereas it would be $\sim$ 61 ^{o}C in case of a 'single pass' of the pump beam and with twice (0.2 at. %) the doping concentration in the crystal, for similar amount of pump light absorption ($\sim$ 188 W).

This trend was also discussed in details in [3.12]. Hence it was justified to use 0.1 at. % crystals with the end-facets being coated for the 'double pass' of the pump beam, in order to reduce thermal stress and beam quality degradation.

A fiber bundle with 10 fibers, each of 600 μm diameter and NA 0.22, is used to deliver ~ 200 W pump light to every Nd:YAG stage. Each fiber is connected to an 808 nm diode laser module (Jenoptik, JOLD-30-CPXF-1L) which can offer 30 W of power at the maximum rated current. In order to get a good spectral overlap of the ten diode lasers for each stage, a digital PID controller was used [3.10] and the FWHM of the overall output pump spectra could be limited to ~ 2.5 nm. A finer temperature-tuning of the wavelength around 808 nm was done experimentally for the maximum amplification of an input/seed beam at 1064 nm. Note that, due to some unavoidable losses of the pump power in the pump optics and the dichroic mirror (HT808/HR1064), the driving current was set in such a way that the pump power in front of the fiber bundle at every stage was around 220 W so that the estimated pump power incident on the Nd:YAG crystal could be roughly near 200 W.

A 10 mm long fused silica rod with 3 mm diameter acts as a pump homogenizer in front of the fiber bundle [3.10]. The pump homogenizer serves two important purposes. Firstly, it makes the pump profile a more uniform transverse distribution of the pump spot and hence fluorescence, instead of having a 'spotty' profile due to individual fibers in the bundle [3.10]. On top of that, since the diodes sources are operated at underrated current to enhance their operational lifetime, in case of failure of an individual diode module, the remaining diode modules can be driven with higher current in order to compensate for the power drop while also maintaining the pump distribution on the crystal [3.10]. A Zemax^{TM} simulation of pump propagation in the system is shown in Fig. 3.6.
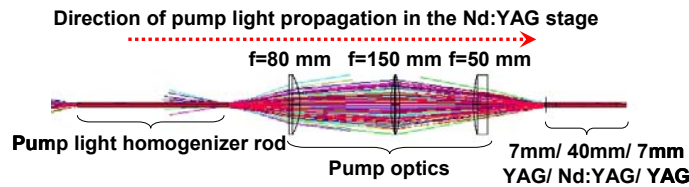

Fig. 3.6 Zemax^{TM} simulation of pump light propagation in an Nd:YAG stage

These amplifiers are pair-wise depolarization compensated using a standard scheme involving 4f imaging lenses and 90° Quartz rotators [3.10, 3.19]. This will be discussed in details in sec. 3.5 of this chapter. A high power Faraday Isolator (HPFI) is used between the pre-amplifier block B and the amplifier block C. Another Faraday Isolator (FI) is used between the NPRO and the pre-amplifier block A. These isolators are in place to protect the NPRO from any laser feedback/back reflection, which can destabilize the single frequency operation seriously.

Once the seed spot size at the 1st doped interface (YAG/Nd:YAG) of the first Nd:YAG stage was set, this would be matched for all other Nd:YAG stages due to the pair-wise 4f imaging (1st & 2nd; 3rd & 4th) and the mode-matching lenses between the 2nd and the 3rd Nd:YAG stages. The power of the seed beam to the amplifier system could be adjusted through a polarizing attenuator without affecting the beam parameters. At this point it would be worth having a look at the schematics of the overall MOPA system shown in Fig. 3.7.
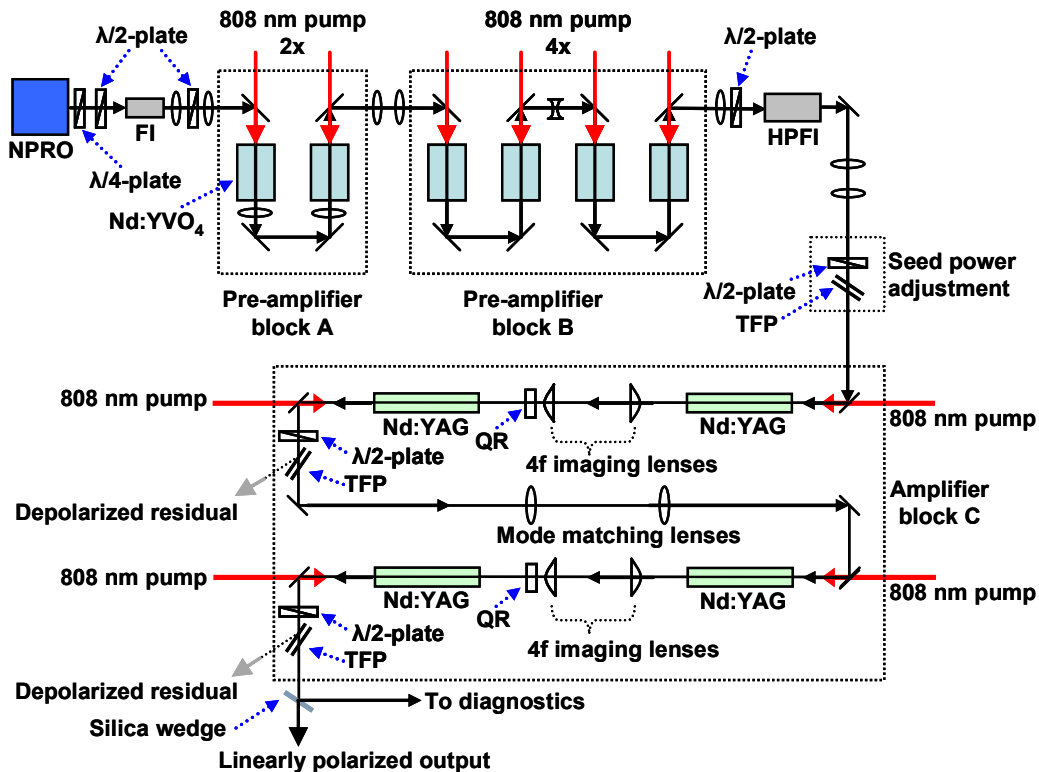

Fig. 3.7 Schematic diagram of the overall MOPA system

3.4 Pump spot measurement technique

Since the gain or amplification greatly depends on the overlap of pump and seed beam, it is more important to know the pump distribution along the length of the rod type crystals than just knowing the minimum focal spot created by the pump-optics. Hence an integrated fluorescence measurement of the rod type crystal under the given pump conditions can be very useful, as described in detail by Puncken in his PhD thesis [3.12].

Given the identical setup of the pump optics for all the four Nd:YAG amplifier stages, it was sufficient to measure the integrated fluorescence profile for just one of those, by using a 4f imaging setup as depicted in Fig. 3.8. The stray 808 nm pump light was avoided by introducing an RG850 filter in front of the CCD camera. Moreover the camera was shielded sidewise in order to avoid stray pump light and fluorescence. The iris aperture was used to chop off any non-paraxial fluorescence component and enhance the image contrast.
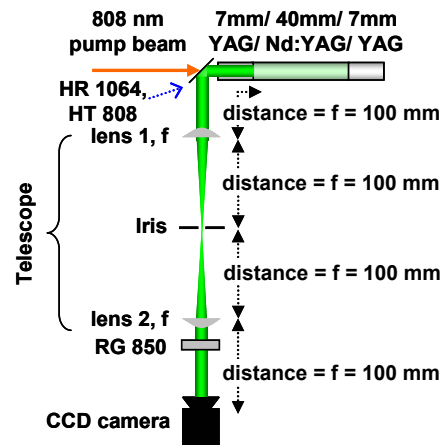
Fig. 3.8 Schematic diagram of the integrated fluorescence measurement setup (not to scale)

Note that, in the setup shown in Fig. 3.8 the 'integrated fluorescence' was imaged from the same side of pump injection, contrary to the one imaging from the throughput side shown in [3.12]. However, given the 'double pass' of the pump light as stated before, and the omni-directional fluorescence generated in the crystal, this should not have any significant impact on the measured size of the integrated fluorescence profile. The CCD image and the vertical and horizontal fluorescence

profile obtained with ~ 200 W of pump power are shown in Fig. 3.9. The horizontal and vertical FWHM were ~ 2090 μm and ~ 2280 μm. The geometric mean would give us an effective pump spot radius of ~ 1.09 mm. Note that the profile is kind of parabolic with a 25% background. Accordingly, a parabolic pump profile with spot radius 1.09 mm and a background = 0.25 were used in the LRD simulations.

Fig. 3.9 The CCD image of integrated fluorescence in (a) 2D, (b) 3D;
(c) normalized integrated fluorescence profile

3.5 Thermally induced birefringence and its compensation
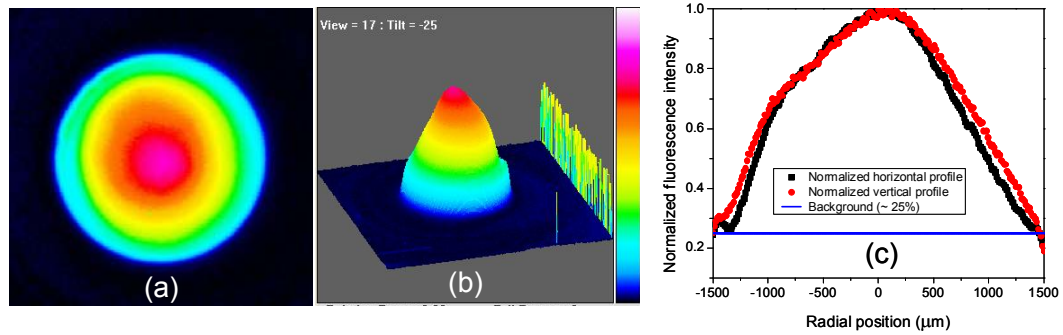
Although Nd:YAG is naturally isotropic, thermally induced stress can make it birefringent [3.19, 3.20]. Depending on the pump light distribution and the crystal cooling architecture, a transverse temperature gradient is generated in the end-pumped Nd:YAG rods. This temperature gradient results in polarization specific (radial & tangential) refractive indices through photoelastic effect [3.20]. Hence linearly polarized operation of a laser or amplifier system can be severely affected due to depolarization and bifocusing. Such thermally induced birefringence or depolarization is most efficiently compensated or reduced by using a combination of 4f-imaging optics and a 90$^{\text{o}}$ quartz rotator between a pair of crystals [3.10, 3.19]. However, there exist relatively simpler schemes for partial compensation of thermally induced birefringence [3.21, 3.22]. On the other hand intrinsic reduction of the depolarization loss in the Nd:YAG crystals cut in the [110] and [100] directions, as compared to the depolarization loss in the conventional [111] cut Nd:YAG crystals has also be demonstrated [3.20].

Before going into the details of the birefringence compensation scheme used in the MOPA system, let us visualize the origin of depolarization. Fig. 3.10 shows the transverse cross section of a rod type crystal and the thermally induced different refractive indices in the radial and tangential directions are given by n_r and n_φ respectively, for the point (r,φ) in the cylindrical co-ordinate system of the rod. Now, let us imagine a linearly polarized seed beam (either parallel to X (horizontal) or Y (vertical) direction). Clearly, the seed beam inside the crystal will experience birefringence at all points excluding the points lying along the X & Y axes.
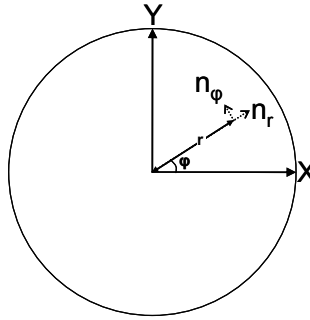
Fig. 3.10 Birefringence in a rod type crystal

Note that depolarization can be stated mathematically as the ratio of depolarized power and the initial total power in linear polarization for a non-resonant probe beam. A detailed derivation of depolarization in rod type crystals can be found in [3.23]. In case of a seed beam in an amplifier, since gain is involved, depolarization can be redefined as the ratio of output power in the depolarized component and the total output power. Now, it will be worth estimating the depolarization loss in a single Nd:YAG stage. Fig. 3.11 shows the pair-wise depolarization compensation scheme used in the MOPA system. In this system, the image of the 'phase slip' due to depolarization in one crystal is projected with equal magnitude but opposite sign onto the next crystal which is in co-axial symmetry with the first one. Hence, ideally the depolarization in the first one should cancel out or compensate for the same in the next one. Practically, 100% compensation is not possible since the depolarization in a crystal is not limited to a single plane and also the 4f- imaging optics may not be perfect. Nevertheless, this technique is quite simple

and highly effective in paired rod type crystal based laser or amplifier systems [3.10, 3.12].
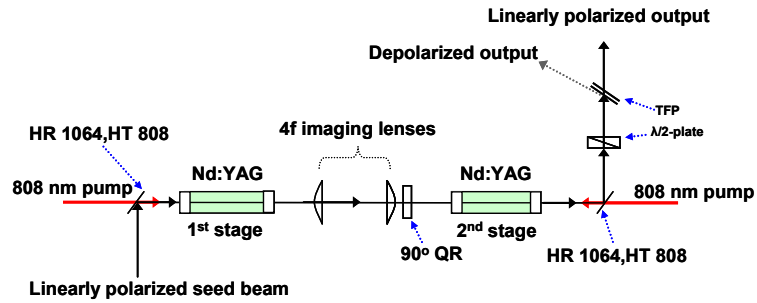
Fig. 3.11 Pair-wise depolarization compensation

Note that by rotating the $\lambda/2$-plate shown in Fig. 3.11, the depolarized power (P_d) and the linearly polarized output power (P_{lp}) were measured as the minimum and maximum transmitted/throughput power respectively, measured after the TFP. Hence the depolarization could be expressed or calculated as $P_d/(P_d+P_{lp})$.

Since depolarization depends on the probe or seed beam size [3.23, 3.24], a simulation with LRD was performed initially to see the trend for an uncompensated single Nd:YAG stage as shown in Fig. 3.12. The pump power was set at 200 W.
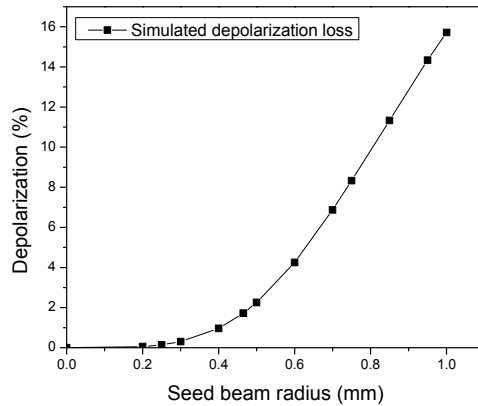
Fig. 3.12 Simulation of the variation depolarization with seed beam size

Experimentally, using a seed beam of $\sim$ 1500 μm diameter and without the 90° quartz rotator, the depolarization measured individually in the 1st and 2nd Nd:YAG stage, i.e. with the pump being ON in one stage while OFF in the other, were $\sim$ 6.3% and $\sim$ 7.5% respectively and this was in good agreement with the LRD simulation

showing an expected ~ 8.3% depolarization. The slight difference with simulation might have been due to variable seed size along propagation. After introducing the QR as shown in Fig. 3.11, the depolarization dropped down to 1.7% and that was consistent with the report on a 2-stage laser system using similar Nd:YAG stages [3.10].

It is worth mentioning that for depolarization measurements, the TFP or the polarizing beam splitter cube must have an inherently good polarization extinction ratio (PER). In the measurements reported here, the TFP or the polarizing beam splitter cube (PBS) had a PER >500:1 or >1000:1 respectively.

3.6 Amplifier output power and beam quality characterization

Once depolarization was compensated efficiently, the main objective was power scaling while maintaining good beam quality.

The total small signal gain (G_0) for a single stage was measured to be ~ 2.3 for ~ 200 W of pump power. From the expression for the maximum available intensity ($I_{available} = \ln(G_0) \cdot I_{sat}$) given by Siegman [3.25] and using the widely used saturation intensity for Nd:YAG, I_{sat}= 2.9 kW/cm^2, it was calculated that roughly a maximum of ~ 42.7 W of power could be extracted from each Nd:YAG stage for a top-hat circular seed beam with 1500 μm diamater. This was also in good agreement with the output power of ~ 150-160 W produced by a ring laser with four such Nd:YAG stages at 800 W of total pump power [3.11]. It was also calculated that for a 25 W Gaussian beam with 1500 μm diameter, the peak intensity would be slightly lower than I_{sat}. That means, as long as the overall output power is less than 25 W for the Gaussian seed beam with 1500 μm diameter in the chain of 4 amplifier stages, the differential gain coefficient, $g(r,z) \in (g_0/2, g_0]$, where g_0 is the small signal gain coefficient. Note that the above mentioned calculations assumed a uniform transverse gain profile too, which is not exactly true for a parabolic pump profile. However, as compared to a normalized parabolic gain profile of the same total width-span, a normalized uniform (flat-top) gain profile would have worse effect of gain saturation on a Gaussian seed beam. Nevertheless, the experimental results with Gaussian seed beam

and parabolic gain profile together match well with the simple calculations based on top-hat seed and gain profile.

In absence of pre-amplifier block B, ~ 18.5 W of output power was generated from the pre-amplifier block A and after passing through some optics and a low power FI, the seed power available just before the amplifier block C was 14.5 W. With that 14.5 W of seed power the linearly polarized output power produced by a single Nd:YAG stage was ~ 26 W and the output vs seed power plot is shown in Fig. 3.13.
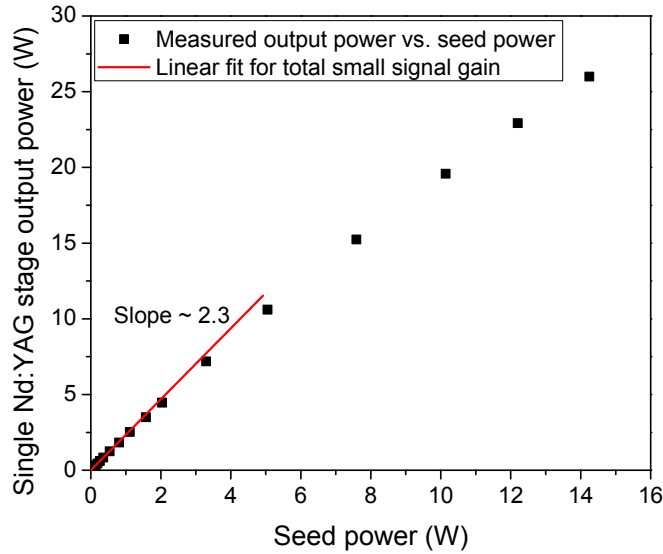
Fig. 3.13 Single Nd:YAG stage output power vs. seed power

Then a 2-stage Nd:YAG amplifier system with depolarization compensation was set up and it generated a linearly polarized output power of ~ 45 W and TEM_{00} mode content was ~ 88.7% for a seed power of ~14.5 W with 90.6% TEM_{00} mode content. The mode scan of that 45 W output beam is shown in Fig. 3.14. For better clarity, the normalized intensity along the vertical axis is shown in logarithmic scale in all the mode scan plots. The beam profile is shown in inset. It should be noted that the TEM_{00} mode content of the single stage amplifier output was not measured keeping in mind the adverse effect of uncompensated depolarization on the beam profile. The DBBL can analyze single polarization component only. However,

depolarization can not be compensated in a single Nd:YAG amplifier stage and hence its output beam quality can not be measured accurately on the DBBL.
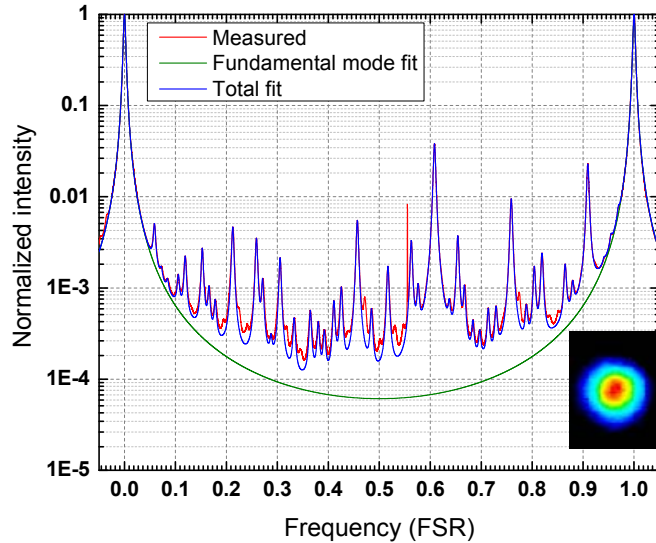
Fig. 3.14 Mode scan of the 45 W linearly polarized output from a 2-stage Nd:YAG amplifier

In the next step, the complete 4-stage Nd:YAG amplifier system was set up for characterization. With a seed power of ~ 15 W the amplifier system produced a linearly polarized output power of ~ 89 W with a good Gaussian beam profile as shown in Fig. 3.15 (CCD image). The TEM$_{00}$ mode content was better than 85% and the mode scan is shown in Fig. 3.16.
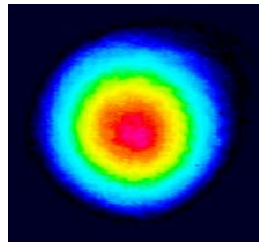
Fig. 3.15 Beam profile of the 89 W linearly polarized output from the 4-stage Nd:YAG amplifier
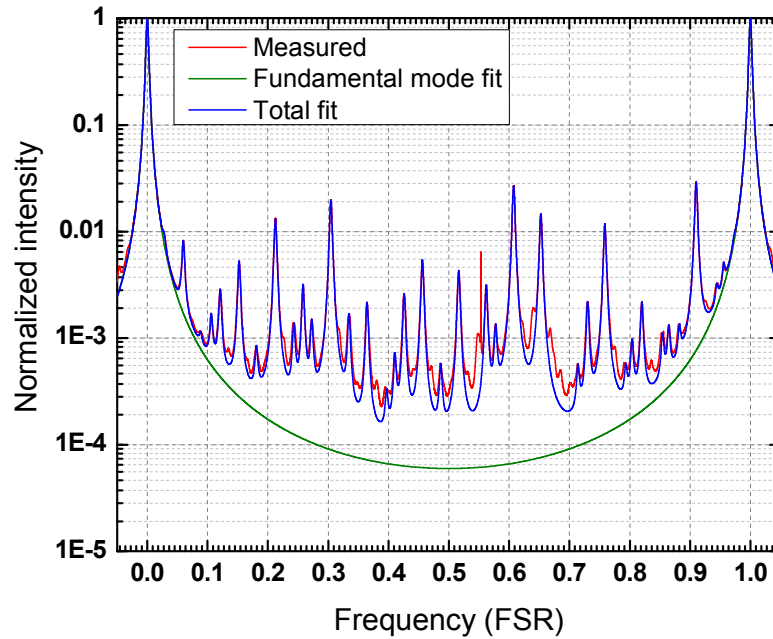
Fig. 3.16 Mode scan of the 89 W linearly polarized output beam with > 85.6 % TEM_{00} mode content

After installing the pre-amplifier block B, roughly 60 W of linearly polarized seed power was available to the 4-stage Nd:YAG amplifier system. The amplifier system was then characterized at 3 different seed sizes (diameter ~ 930 μm, ~ 1500 μm and ~ 1900 μm) and the results are shown in Fig. 3.17. The TEM_{00} mode contents measured at the maximum output power are shown with arrows and the estimated powers in the fundamental TEM_{00} are shown within parentheses. Note that for the seed beam with 1500 μm diameter, the mode scan was performed after measuring the maximum linearly polarized output power of ~ 177 W and 83.5% TEM_{00} mode content was measured. However, on another day when the output vs. seed power was characterized, the maximum linearly polarized output power was ~ 183 W with 80.9% TEM_{00} mode content, at a seed power of ~ 56.1 W as shown in Fig. 3.17. But for ~ 5W of seed power the output power was ~ 60.2 W with 86.3% TEM_{00} mode content. This change in the fundamental mode content of the output with seed power could be explained later with further experiments as described in pages 18-20 of this chapter.

Note that both the 177 W output beam and the 183 W output beam with 83.5% and 80.9% TEM_{00} mode contents respectively would give almost equal to

~ 148 W power in the fundamental TEM_{00} mode. The day-to-day variation in the maximum available seed power and hence the linearly polarized output power could be attributed to a degrading pump diode module in the pre-amplifier system.
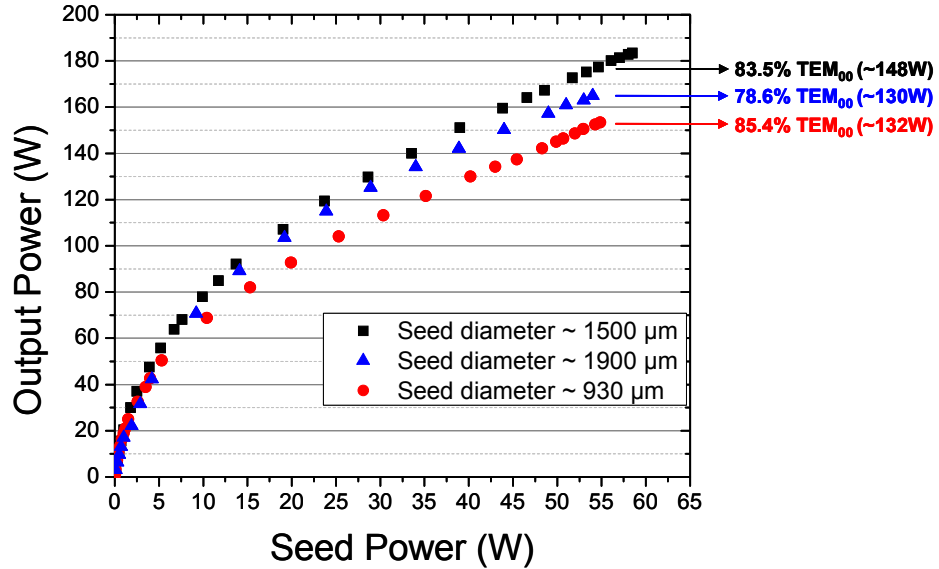
Fig. 3.17 Gain characterization of the 4-stage amplifier system at different seed sizes

For the optimum output power as well as beam quality, the seed diameter of ~ 1500 μm was clearly the best option. It can be said that, for a given pump light distribution, one has to fix the seed beam size in such a way that the output power is maximum whereas beam degradation due to both gain saturation and wavefront aberration are minimum. Although a small seed beam is better in order to minimize spherical aberration, its amplification is limited due to poor overlapping with the pump light profile and it may also suffer beam quality degradation due to spatially varying gain saturation. On the other hand, a large seed beam may have a better gain in the amplifier at the cost of greater spherical aberration and diffraction losses [3.26, 3.27]. The choice of the optimal seed diameter is also substantiated in chapter 5 in terms of the impact of spherical aberration on beam quality.

The mode scan of the 177 W linearly polarized output for the ~ 1500 μm seed beam is shown in Fig. 3.18 and the beam profile is shown in inset.
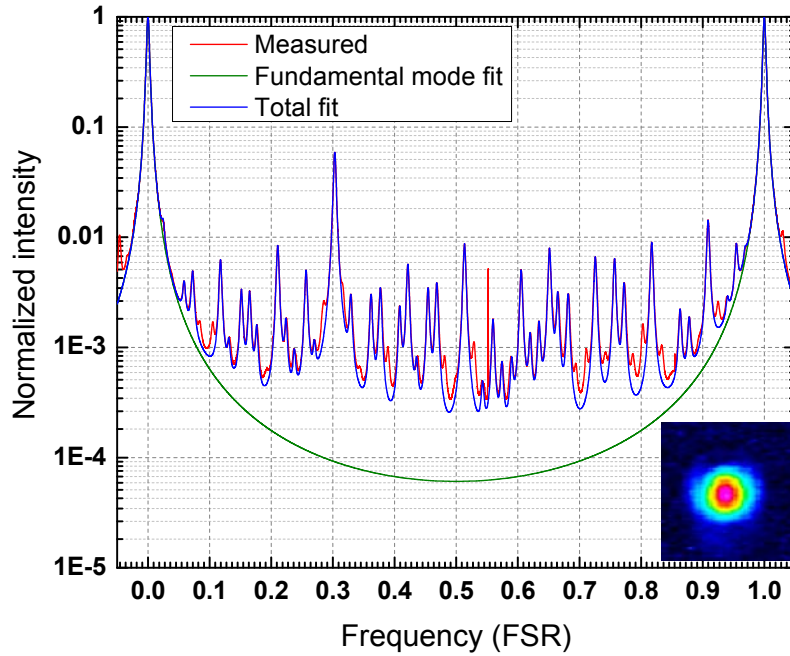
Fig. 3.18 Mode scan of the ~ 177 W linearly polarized amplifier output with 83.5 % TEM_{00} mode content at a ~ 1500 μm seed (diameter)

With a smaller seed beam of diameter ~ 930 μm, the maximum output power was ~ 154 W with ~ 85.4% TEM_{00} mode content and the corresponding mode scan is shown in Fig. 3.19.
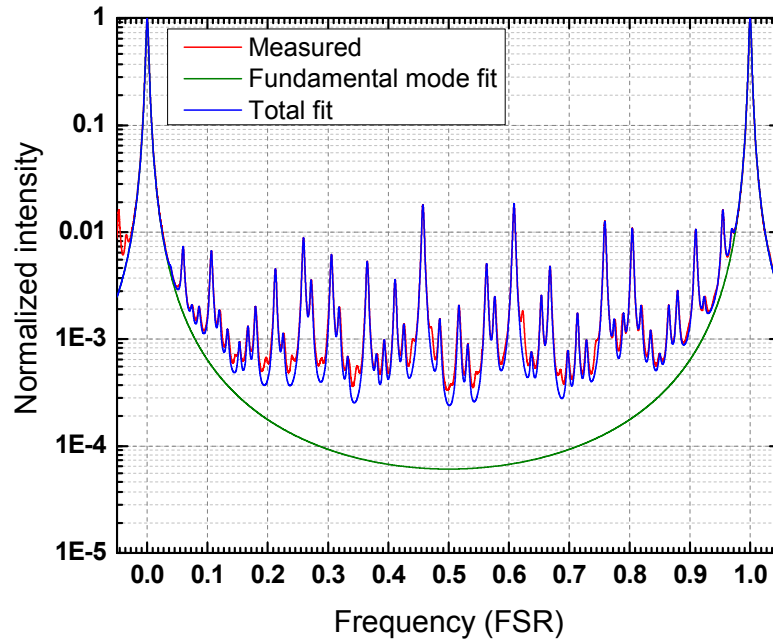
Fig. 3.19 Mode scan of the ~154 W linearly polarized output beam with 85.4% TEM_{00} mode content for a seed beam of ~ 930 μm diameter

In the experiments with the seed beam of diameter ~ 930 μm, it was observed that the output beam profiles looked very different for low (~ 1 W) and high (~ 57.7 W) seed power levels as shown in Fig. 3.20 (a) and (b).
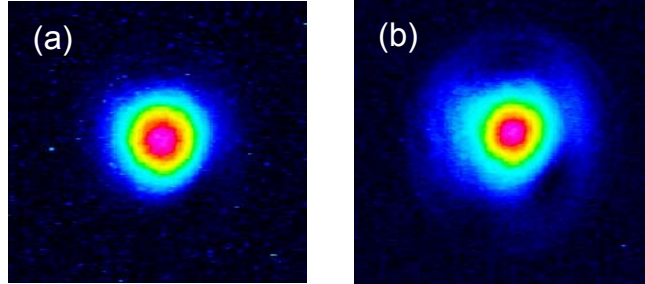
Fig. 3.20 (a) The ~ 19 W linearly polarized output beam profile at ~ 1 W of seed power and (b) the ~ 154 W linearly polarized output beam profile at ~ 57.7 W of seed power

Also, the TEM_{00} mode content measured for ~ 1W and ~ 57.7 W of seed power were ~ 91.8% and ~ 86.4% respectively. However, according to simulations, this could not be explained in terms of beam quality degradation due to gain saturation, described in sec. 3.7, for the Nd:YAG crystals concerned. Nevertheless, the output beam profile as shown in Fig. 3.20 (b) seemed to be more aberrated and stretched out near the periphery as compared to that in Fig. 3.20 (a).

Hence the amplifier system was characterized again with the seed beam of diameter ~ 1500 μm. However, it was noticed that the seed power available to the amplifier system had dropped from ~ 60 W to ~ 50 W due to a degrading diode laser in the pre-amplifier system. Under that seed condition, the linearly polarized output beam profile out of the 2nd stage looked a bit more aberrated with a smeared round pattern around the normal Gaussian profile as shown in Fig. 3.21 (a). This could be improved by reducing the pump driving current in the 1st stage and then accordingly in the 2nd stage by 1.5 A and 1.2 A respectively and a better linearly polarized output beam profile (after the 2nd stage) was observed, as shown in Fig. 3.21 (b).
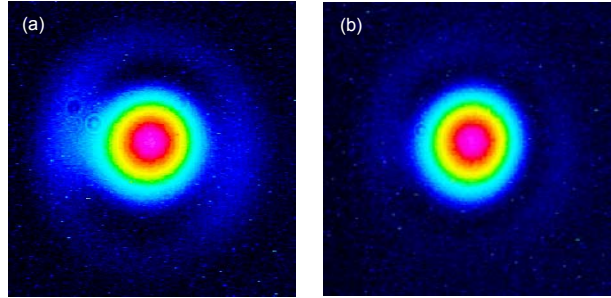
Fig. 3.21 Output beam profile from the 2-stage system (a) before and (b) after pump current reduction

These reductions in driving current would correspond to a pump power drop of ~ 12 W and ~ 8.4 W respectively. The higher than required current setting was due to a manual error in estimation of pump power based on the power-current calibration measurements with two different detectors as well as the arrangement and naming of the diode boxes in the rack system. Apparently, the excess pump powers in the first two heads were causing excessive aberrations leading to a worse beam profile. However, given the relatively little amount of excess power mentioned above, such a significant change in the beam profile and beam quality could not be explained clearly. With the slightly reduced pump powers as stated above, the overall linearly polarized output power out of the 4-stage system was ~ 160 W. Hence the reduction in pump power in the first two stages caused just ~ 2 W drop in the overall linearly polarized output power of the system, while improving the beam profile as shown in comparing Fig. 3.22 (a) and (b).
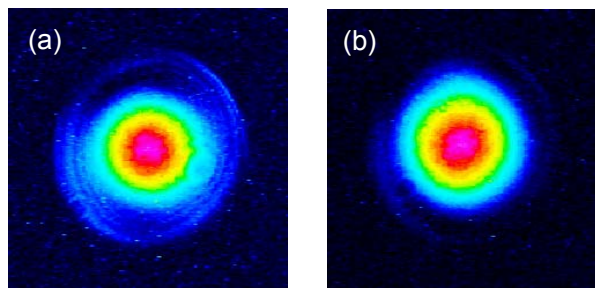
Fig. 3.22 4-stage output beam profile with (a) 162 W, 82.6% TEM_{00} before and (b) 160 W, 85.9% TEM_{00}, after pump power reduction in the 1st & 2nd stage

As a concrete evidence for the aforesaid argument, mode content measurements before reduction of the pump powers in the first two stages, the 162 W

linearly polarized output had ~ 82.6% TEM_{00} mode content whereas with the new pump power settings, the 160 W linearly polarized output had ~ 85.9 % TEM_{00} mode content. At this point, with ~ 1W of seed power, ~ 20.1 W of linearly polarized output was obtained with ~ 86.3% TEM_{00} mode content. Hence it could be said that for the given system, gain saturation related degradation in beam quality was negligible, at least for the seed beam with ~ 1500 µm diameter.

The comparison of the output beam quality at low and high seed power levels for the seed beam with ~ 1500 µm diameter is given in Table 3.2 for easy reference.

Seed power (W)	Overall lin. polarized output power (W)	TEM_{00} (%)
~ 1	~ 20.1	~ 86.3
~ 50	~ 160	~ 85.9
~ 60 (Old settings*)	~ 177	~ 83.5

Table. 3.2 Comparison of TEM_{00} mode content at extreme seed power levels.(*Old setting corresponds to the result before reducing the excess pump powers in the first two stages. This result is also shown in Fig. 3.18).

From the results and discussions above it can be expected that once the pre-amplifier system is repaired to offer ~ 60 W of power level to the Nd:YAG amplifier system, the linearly polarized output beam (at ~ 1500 µm seed) will possibly show a better TEM_{00} mode content (between 83.5% and 89.5%) than in Fig. 3.18, without much deviation from the ~ 180 W power level.

With a larger seed beam with a diameter ~ 1900 µm and a maximum seed beam power of ~ 54 W, a linearly polarized output of ~ 165 W with ~ 78.6% TEM_{00} mode content was generated. With the same size of the seed but ~ 1 W of power, ~ 17.5 W of linearly polarized output with ~ 82% TEM_{00} mode content was obtained. However, this difference in TEM_{00} mode content (~ 3.4%) at extreme seed power levels was too small to be accounted for in relation to gain saturation, especially when the ~ 1500 µm showed even a smaller difference (~ 0.4%). Note that the TEM_{00} mode content fitting errors stated by the software concerned were always below ±1% of the total mode power. Also note that the software actually returns the percentage of higher order mode contents (say, $x\%$) from which the TEM_{00} mode content is calculated as $(100\text{-}x)\%$. The output beam profiles for the 1 W and 54 W seed were

quite similar as shown in Fig. 3.23 (a) and (b) respectively. The mode scan of the 165 W linearly polarized output is shown in Fig. 3.24.
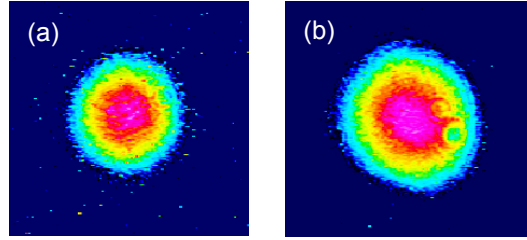
Fig. 3.23 Beam profile of (a) ~ 17.5 W output at ~ 1W seed power (b) ~ 165 W output at ~ 54 W seed power, both with a seed diameter of ~ 1900 μm
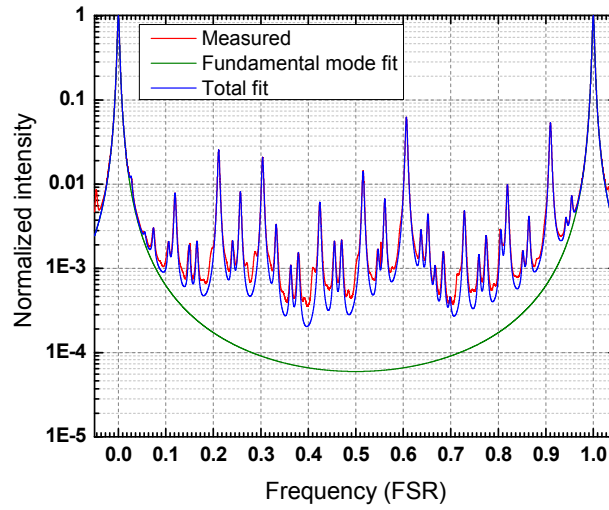
Fig. 3.24 Mode scan of the 165 W linearly polarized output beam corresponding to a seed diameter of ~ 1900 μm

3.7 Simulation of gain saturation

With reference to [3.25], one can represent the differential equation of signal intensity gain along z- direction in a single pass amplifier system as follows:

$$\frac{1}{I(r,z)} \cdot \frac{dI(r,z)}{dz} = \frac{g_0}{1+(I(r,z)/I_{sat})} = g(r,z) \quad \text{Eqn. 3.1}$$

Where, g_0 is the small signal gain coefficient, I is the intensity of the laser beam concerned and I_{sat} is the saturation intensity of the active medium concerned.

The total unsaturated or small signal gain G_0 is given by

$$G_0 = \exp(g_0 \cdot L) \qquad \text{Eqn. 3.2}$$

Here L is the length of the active medium.

Now, as we already know the total small signal gain for a single Nd:YAG stage, we can calculate g_0 for the L=40 mm doped section of the crystal. Now, even if we assume a flat-top or radially uniform gain profile in the crystal (i.e. a constant g_0 over the rod cross section), we must also consider that the seed beam has a Gaussian profile and hence it will experience a spatially varying saturated gain [3.28]. The central portion will reach the saturation early while propagating in the z-direction, whereas due to the decaying intensity away from the centre of the distant parts of the Gaussian beam can still experience higher gain. Eventually, this can result in a non-Gaussian output beam profile and hence a degraded beam quality. In order to simulate such spatially varying gain saturation and resultant degradation in beam quality, let us first visualize the situation as in Fig. 3.25 (a) and see the saturated gain profile for Gaussian seed beams of different sizes and power levels in Fig. 3.25 (b).
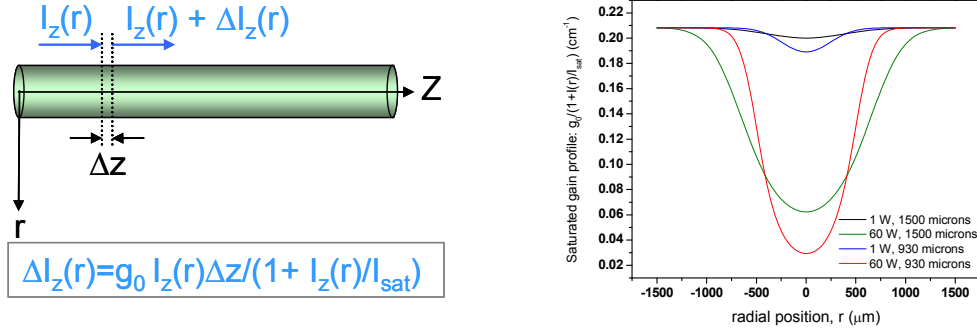
Fig. 3.25 (a) The gain saturation simulation scheme and (b) the gain saturation profile

If we assume n number of thin slices perpendicular to the Z-axis of the crystal such that $n\Delta z=L$ and apply the Eqn. 3.1 for discrete n-steps, as shown in Fig. 3.25 (a), we can generate the output intensity profile $I_L(r)$ and hence the electric field as $\sqrt{I_L(r)}$. Now we can try to find out the optimal overlap integral, with a pure Gaussian field as follows.

$$\alpha = \frac{\int_0^R \sqrt{I_L(r)} \cdot \exp(-r^2/\omega_{opt}^2) \cdot r dr}{\sqrt{\int_0^R I_L(r) \cdot r dr} \cdot \sqrt{\int_0^R \exp(-2r^2/\omega_{opt}^2) \cdot r dr}}$$

The expression for α given above can be re-written in a discrete form as follows:

$$\alpha = \frac{\sum_{j=0}^m \sqrt{I_L(jR/m)} \cdot \exp(-(jR/m)^2/\omega_{opt}^2) \cdot (jR/m)}{\sqrt{\sum_{j=0}^m I_L(jR/m) \cdot (jR/m)} \cdot \sqrt{\sum_{j=0}^m \exp(-2 \cdot (jR/m)^2/\omega_{opt}^2) \cdot (jR/m)}}$$

Here, R is the radius of the rod type crystal and $(m+1)$ is the number of discrete steps for calculation. ω_{opt} is the Gaussian beam radius to be optimized for the maximum value of $\eta = \alpha^2$ and then that maximum value of η would be the estimated TEM$_{00}$ mode content.

Using the above mentioned method a simulation was performed for the whole 4-stage amplifier system assuming an active medium of 4x40 mm length and for all the experimental values of seed sizes, i.e. 930 μm, 1500 μm and 1900 μm in diameter, the calculated TEM$_{00}$ mode content was always > 99%. Hence the simulation of gain saturation, assuming a flat-top gain profile throughout the cross-sectional area, could not explain any degradation in beam quality. For these calculations, I_{sat}=2.9 kW/cm^2 and experimental G_0=2.3^4 were used. The seed power was set as 60 W for which the peak input intensity (I_0) was calculated. Note that the simplified simulation technique described here assumed a uniform seed size throughout the length of propagation. Still, it was understood that due to a modest value of G_0, the effect of spatially differential gain saturation on the degradation of beam quality was negligible. This was in good agreement with the experimental results shown in Table 3.2 where the output TEM$_{00}$ mode content did not change significantly while the seed power changed massively from ~ 1 W to ~ 60 W. In this context it can be mentioned that a

Gaussian seed beam with ∼ 26 W of power and a diameter of ∼ 1500 μm would give a peak intensity (2.94 kW/cm^2), slightly higher than the saturation intensity (I_{sat}) mentioned above.

3.8 Conclusions

In this chapter, the optical and physical properties of Nd:YAG as an active medium have been discussed briefly. The opto-mechanical design of the the 4-stage Nd:YAG amplifier system has been described in detail. Measurement of an effective pump spot size inside the rod type Nd:YAG crystals by imaging the integrated fluorescence has been demonstrated.

The origin of thermally induced birefringence or depolarization has been mentioned and a technique adapted to minimize such depolarization loss has been shown in details along with experimental validation.

Most importantly, power scaling in the amplifier system has been discussed with experimental details. Out of three different seed sizes used, a Gaussian seed beam with 1500 μm diameter was shown to be the best choice for optimal linearly polarized output power of ∼ 177 W with ∼ 83.5% TEM$_{00}$ mode content for the given pump power and profile.

No significant effect of spatially differential gain saturation on the beam quality was observed experimentally as well as through a simulation. Hence it was evident that the major source beam quality degradation in the amplifier system was thermally induced wavefront aberrations which will be discussed in Ch.5.

References Ch. 3

3.1) J E Geusic, H M Marcos and L G Van Uitert, "LASER OSCILLATIONS IN Nd-DOPED YTTRIUM ALUMINUM, YTTRIUM GALLIUM AND GADOLINIUM GARNETS"; Applied Physics Letters, Vol. **4**, 1964, p 182-184

3.2) M Frede, R Wilhelm and D Kracht, "250 W end-pumped Nd:YAG laser with direct pumping into the upper laser level"; Optics Letters, Vol. **31**, 2006, p 3618-3619

3.3) X Délen, I Martial, J Didierjean, N Aubry, D Sangla, F Balembois and P Georges, "34W continuous wave Nd:YAG single crystal fiber laser emitting at 946 nm"; Applied Physics B, Vol. **104**, 2011, p 1-4

3.4) C Y Li, Y Boa, Y T Xu, F Yang, Z C Wang, B S Wang, J L Xu, H W Gao, Q J Peng, D F Cui, Z Y Xu, "219.3W CW diode-side-pumped 1123 nm Nd:YAG laser"; Optics Communications, Vol. **283**, 2010, p 2885–2887

3.5) N Simakov, D J Hosken, M W Hamilton and J Munch, "Injection Mode-Locked, Q-Switched Nd:YAG Laser at 1319 nm"; IEEE Journal of Quantum Electronics, Vol. **46**, 2010, p 1086-1090

3.6) Y Yang, J L Xu, J L He, X Q Yang, B Y Zhang, H Yang, S D Liu and B T Zhang, "Diode-pumped passively mode-locked Nd:YAG laser at 1338 nm with a semiconductor saturable absorber mirror"; Applied Optics, Vol. **50**, 2011, p 6713-6716

3.7) H C Lee, S U Byeon and A Lukashev, "Diode-pumped continuous-wave eye-safe Nd:YAG laser at 1415 nm"; Optics Letters, Vol. **37**, 2012, p 1160-1162

3.8) K C Tark, J E Jung and S Y Song, "Superior Lipolytic Effect of the 1,444nm Nd:YAG Laser: Comparison With the 1,064nm Nd:YAG Laser"; Lasers in Surgery and Medicine, Vol. **41**, 2009, p 721–727

3.9) L Winkelmann, O Puncken, R Kluzik, C Veltkamp, P Kwee, J Poeld, C Bogan, B Willke, M Frede, J Neumann, P Wessels and D Kracht, "Injection-locked single-frequency laser with an output power of 220W"; Applied Physics B, Vol. **102**, 2011, p 529–538

3.10) M Frede, R Wilhelm, R Gau, M Brendel, I Zawischa, C Fallnich, F Seifert and B Willke, "High-power single-frequency Nd:YAG laser for gravitational wave detection"; Classical and Quantum Gravity, Vol. **21,** 2004, p 895–901

3.11) M Frede, R Wilhelm, D Kracht and C Fallinch, "Nd:YAG ring laser with 213 W linearly polarized fundamental mode output power"; Optics Express, Vol. 13, 2005, p 7516-7519

3.12) O Puncken, "Pumpkopfdesign für den Advanced LIGO Laser"; PhD Thesis 2011, Leibniz Universität Hannover; Cuvillier Verlag Göttingen 2011, ISBN 978-3-86955-967-4

3.13) W Koechner, "Solid-state Laser Enginnering", 6th Edition, Published by Springer, 2010, ISBN-10: 1441921176

3.14) Web source: Encyclopedia of Laser Physics and Technology, URL: http://www.rp-photonics.com/yag_lasers.html

3.15) M C Nostrand and R H Page, "Nd:YAG effective emission cross section using novel method based on laser performance data"; Advanced Solid-State Lasers Conference, 2001 Technical Digest, 2001, p 438-440

3.16) M Birnbaum, A W Tucker and C L Fincher, "Laser emission cross section of Nd:YAG at 1064 nm"; Journal of Applied Physics, Vol. 52, 1981, p 1212-1215

3.17) B F Aull and H P Jenssen, "Vibronic Interactions in Nd:YAG Resulting in Nonreciprocity of Absorption and Stimulated Emission Cross Sections"; IEEE Journal of Quantum Electronics, Vol. **18**, 1982, p 925-930

3.18) D C Brown, "Heat, Fluorescence, and Stimulated-Emission Power Densities and Fractions in Nd:YAG"; IEEE Journal of Quantum Electronics, Vol. **34**, 1998, p 560-572

3.19) Q Lü, N Kugler, H Weber, S Dong, N Müller and U Wittrock, "A novel approach for compensation of birefringence in cylindrical Nd:YAG rods," Optical & Quantum Electronics, Vol. **28**, 1996, p 57-69

3.20) O Puncken, H Tünnermann, J J Morehead, P Weßels, M Frede, J Neumann and D Kracht, "Intrinsic reduction of the depolarization in Nd:YAG crystals," Optics Express, Vol. **18**, 2010, p 20461-20474

3.21) W A Clarkson, N S Felgate and D C Hanna, "Simple method for reducing the depolarization loss resulting from thermally induced birefringence in solid-state lasers"; Optics Letters, Vol. **24**, 1999, p 820-822

3.22) J J Morehead, "Compensation of laser thermal depolarization using free space", IEEE Journal of Selected Topics in Quantum Electronics, Vol. **13**, 2007, p 498-501

3.23) I Shoji and T Taira, "Intrinsic reduction of the depolarization loss in solid-state lasers by use of a .110.-cut $Y_3Al_5O_{12}$ crystal"; Applied Physics Letters, Vol. **80**, 2002, p 3048-3050

3.24) Y Wang, K Inoue, H Kan, T Ogawa and Satoshi Wada, "Birefringence compensation of two tandem-set Nd:YAG rods with different thermally induced features"; Journal of Optics A: Pure and Applied physics, Vol. **11**, 2009, p 1-9

3.25) A E Siegman, Book- "Lasers"; 1st edition, Published by University Science Books, ISBN: 978-0935702118

3.26) J Alda, J Alonso and E Bernabeu, "Characterization of aberrated laser beams"; Journal of Optical Society of America A, Vol. **14**, 1997, p 2737-2747

3.27) A E Siegman, "Analysis of laser beam quality degradation caused by quartic phase aberrations"; Applied Optics Vol. **32**, 1993, p 5893-5901

3.28) W B Bridges, "J-3-Gaussian Beam Distortion Caused by Saturable Gain or Loss"; IEEE Journal of Quantum Electronics, Vol. **4**, 1968, p 820-827.

Ch.4 Relative intensity noise measurements

4.1 Introduction

In every physical system noise is inevitable and laser sources are no exceptions. For gravitational wave detectors, noise suppression in laser sources is a key issue and this is addressed with very complex electronic control systems [4.1-4.4]. Nevertheless, one would definitely prefer to start with a low noise free running laser source or amplifier system. Noise in laser systems can be broadly classified into i) intensity noise and ii) frequency noise and each of these demand an elaborate treatment. However, this chapter will focus only on the intensity noise measurements in the MOPA system concerned. Relative intensity noise measurements of the 808 nm pump diodes, NPRO, pre-amplifier block B and amplifier block C will be compared. A simulation will be presented in order to understand the pump-to-signal noise transfer and excess output noise at very low seed power.

4.2 Sources of intensity noise

The typical sources of intensity noise in a laser amplifier system are shown in Fig. 4.1.
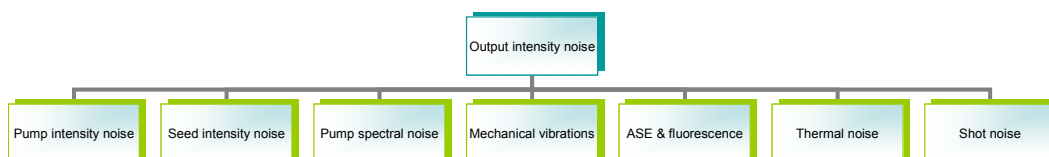
Fig.4.1 Major sources of amplifier output noise

The pump intensity noise affects the population inversion and directly affects the output intensity. On the other hand, any fluctuation in the spectra of the pump source can also alter the population inversion and result in additional noise. Mechanical vibrations can affect the overlapping of seed and pump beams at every stage of the amplifier and vary the output intensity. Not all the absorbed pump photons contribute to amplifier gain. Some parts of it generate both ASE and fluorescence, which depend on the input seed intensity. The effect of this kind of interplay between the seed intensity, ASE and fluorescence, on the output noise is not easy to analyze experimentally. Thermally induced fluctuations in refractive index and polarization can also affect the linearly polarized output of the amplifier system.

Shot noise can be visualized as the inherent randomness of the number of photons arriving at a detector surface in a given time interval. Shot noise follows a Poisson distribution and is proportional to the square root of power of the laser beam concerned. Hence the signal-to-noise ratio (SNR) of a detector read-out in the shot noise limited regime will be proportional to the square root of power ($P/\sqrt{P} = \sqrt{P}$). For the GWD community, studies on shot noise are of immense importance and squeezed light sources have emerged as the way to beat the limitation imposed by shot noise level [4.5-4.6].

4.3 Relative intensity noise (RIN) in an amplifier

In general, the absolute amount of noise is not a useful quantity to compare between two systems. What matters is the relative value of the noise with respect to the average signal intensity (DC value) concerned. As a function of frequency (f) the RIN can be expressed mathematically as $RIN(f) = \dfrac{\sqrt{\langle \Delta P^2(f) \rangle}}{P}$, where P is the average power level and the numerator is the root-mean-square (rms) noise. Actually, it would be more appropriate to use the term 'relative power noise' for the measurements and simulations discussed in this chapter. However, 'relative intensity noise' is a more common term in the GWD community.

Now let us first consider a saturable amplifier where noise contributions from the pump source and all other noise sources are negligible.

Keeping in mind the long upper state fluorescence life time ($\sim 220\,\mu s$ in Nd:YAG), the low frequency noise components in the seed power will modulate the population inversion. In case of an unsaturated amplifier, such slow noise components will experience the same overall gain factor as experienced by the average (DC) level of the seed power. Hence the output RIN of the amplifier will match that of the seed. On the other hand, in case of a saturated amplifier, the absolute output noise power will be same as the absolute noise power in the seed beam. Hence the RIN of the output will be suppressed by the overall gain factor, as compared to the seed RIN. This means that in a hypothetical chain of amplifiers where pump noise and other noise sources are neglected, the output RIN will be lower than the seed RIN in the low frequency range. So, in principle, a MOPA approach for power scaling is advantageous in order to suppress the output RIN.

Now, if we consider the high frequency noise components in the seed power level, the population inversion will fail to respond fast enough to such modulations and hence the noise components will see the same gain as seen by the average seed level, for both saturated and unsaturated amplifier systems. Hence, irrespective of the small signal or saturated gain regime, the amplifier output RIN will match with the seed RIN.

Now if we consider pump noise, only the low frequency noise components can have influence on the population inversion and hence on the output RIN. The population inversion will fail to respond to the high frequency pump noise components. In other words, the active medium will behave like a low pass filter to the pump noise. Hence, the amplifier output RIN will be dominated by the seed RIN in the high frequency regime. It is only in the low frequency regime that the combined effect of seed and pump RINs will influence the amplifier output RIN. This issue is clarified further through a simulation in sec. 4.8.

4.4 Noise detection technique

Photo-diodes in reverse-bias or trans-impedance-amplifier configuration are most suitable for measuring very low power of a light source. The incident photons generate a current of photo-electrons which result in a voltage read-out from the 'load' resistor of the photo-diode. Naturally, the photon to photo-electron conversion has certain efficiency depending on the detector material and the frequency (ν) of the incident photon radiation. Biased InGaAs PIN photo-diode (Thorlabs[TM] DET10C) as well as switchable gain Silicon photo-diode (Thorlabs[TM] PDA36A-EC) were used for the experiments mentioned in this chapter. An electric spectrum analyzer (Stanford Research[TM], SR785) was used to analyze the noise spectra in the frequency domain. The block-diagram in Fig. 4.2 will further explain the setup.
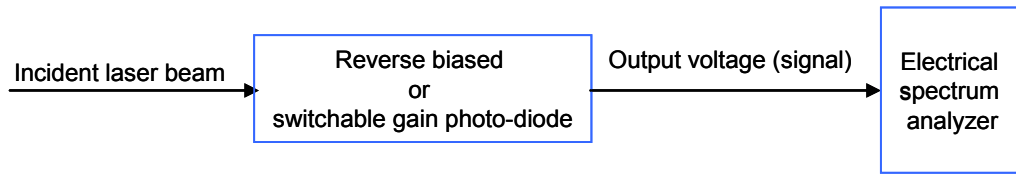
Fig. 4.2 Block diagram of RIN measurement setup

As the intensity noise of the incident laser beam would transform into noise in the output voltage of the photo-diode, one has to ensure that the photo-diode operates in a linear response regime and is not saturated. Apart from that, one has to consider the bandwidth limitation of the photo detector. For a typical biased photo-diode (e.g. DET10C) the bandwidth can be altered to a certain extent by changing the load resistance (R_{load}) as bandwidth, $f_{BW} = 1/(2\pi.R_{load}.C_j)$ where C_j is the junction capacitance. In other words, for a given photo-diode, one can use a suitable shunt resistor at the BNC output in order to change the bandwidth as required. In case of a switchable gain photo-diode (e.g. PDA36A-EC) one has to refer to the datasheet for the bandwidth limitations at different gain levels. Most importantly, the incident laser beam must have a power lower than the specified damage threshold of the photo-diode. It is often complained that photo-diodes suffer from surface non-uniformity [4.7]. To minimize errors due to positional issues, one must try to centre the incident

beam on the active area of the detector and follow that for all the experiments. A lens is often used to focus the incident beam onto the detector. To avoid stray light of any kind, suitable filters and an iris-aperture can be very useful.

4.5 Shot noise and detector noise

The relative shot noise level can be calculated as $\sqrt{2e/I}$ where e is the charge of an electron (in Coulomb) and I is the detector current (in Ampere). Since we measure the output voltage (V) of a detector across a shunt resistor ($\sim$kΩ), whereas the instrumental load resistance is a few MΩ, it is easier to express the current as $I \approx V/R_s$. For a given shunt and at a fixed sensitivity level (dBV$_{pk}$) of the analyzer, if RIN of any system is being measured by a photo-diode at an output voltage of V$_{dc}$, one has to make sure that the RIN of the dark noise (calculated as, $RIN_{dark} = absolute\ dark\ noise/V_{dc}$) is significantly lower than the measured RIN of the system (i.e. $RIN_{dark} < RIN_{syst.\ measured}$). Otherwise, the measurement will be erroneous. Although, in some cases where the values of RIN_{dark} and RIN_{syst} are very close, the actual RIN of the system can be mathematically corrected as $RIN_{syst.\ corrected} = \sqrt{(RIN_{syst.\ measured})^2 - (RIN_{dark})^2}$. This is explained in Fig. 4.3 where the measured RIN of the NPRO, RIN of the dark noise of the photo-diode and the corrected RIN of the NPRO are compared. The measured NPRO noise is much higher than the corresponding dark RIN in the 1 Hz-10 kHz range and hence the corrected RIN does not show any significant difference from the measured one in that frequency range. But, in the 10 kHz-100 kHz range, the measured RIN of the NPRO and the corresponding dark RIN (blue) of the photo-diode are somewhat close and hence the corrected RIN (red) of the NPRO is slightly different from the measured RIN (black).

In this context, it is worth mentioning that independent (i.e. incoherent) RINs add up as the square root of the summation of the squares of individual RINs.

To have a rough estimate of how much accuracy can be expected in measured RINs without any corrections for the dark RIN, the following simple calculation can be useful.

If we expect an uncorrected measured RIN to have 90% or more accuracy as compared to the corrected RIN (i.e. $\frac{RIN_{syst.\,corrected}}{RIN_{syst.\,measured}} \in [0.9,1)$), the uncorrected measured RIN level should be $1/\sqrt{1^2 - (0.9)^2} \approx 2.3$ times (or higher) than the dark RIN level concerned (i.e. $\frac{RIN_{syst.\,measured}}{RIN_{dark}} \geq 2.3$), throughout the measured frequency range.
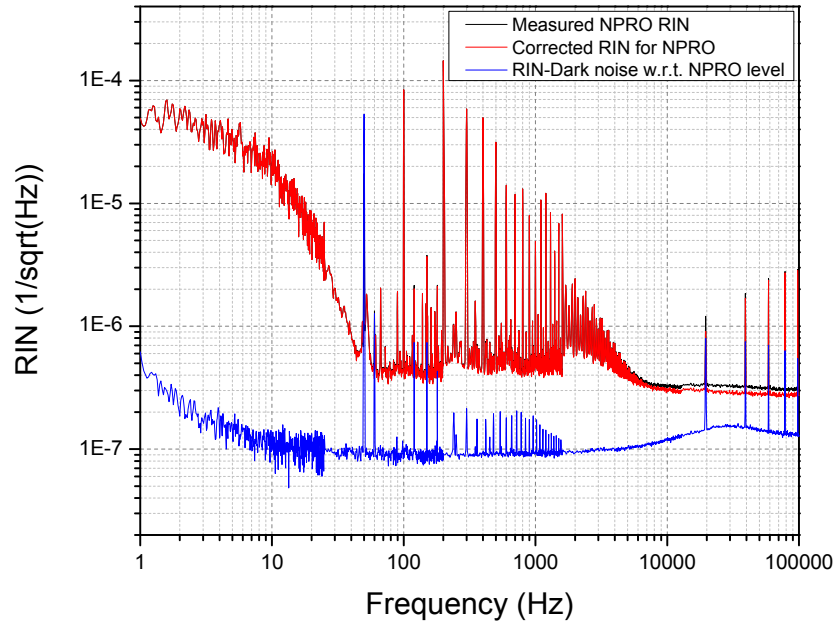
Fig. 4.3 Measured and corrected RIN of the NPRO

Please note that the so-called pink noise was unavoidable in all the experiments. Pink noise or 1/f noise is more prominent in the low frequency regime (1-50 Hz) and can be ignored while analyzing the rest of the noise spectra up to 100 kHz. The analyzer, SR785 is itself limited to the maximum frequency of 102.4 kHz. Note that the spike at 50 Hz and related higher harmonics, in all the RIN plots, could be attributed to the frequency of the standard power supply in the lab. The spike at 60 Hz and its higher harmonics could be attributed to the refresh rate or

flicker rate of the CRT display of the electrical spectrum analyzer. The spike at 20 kHz could be attributed to the line frequency of the CRT display.

4.6 RIN of the 808 nm pump diodes

The RIN of the 808 nm pump light was characterized in two ways. First, only the scattered part (from the pump optics) of the pump light was collected by a lens to focus on the photo-diode. Fig. 4.4 shows the pump RIN results obtained from the four Nd:YAG stages, using the above mentioned technique. The pump power was ~ 200 W in every Nd:YAG stage. This approach was based on an assumption that the RIN of the scattered part should not be much different from that of the whole beam itself, as the pump light from each diode travels through couple of metres of fibers and also mix up spatially inside the homogenizer.
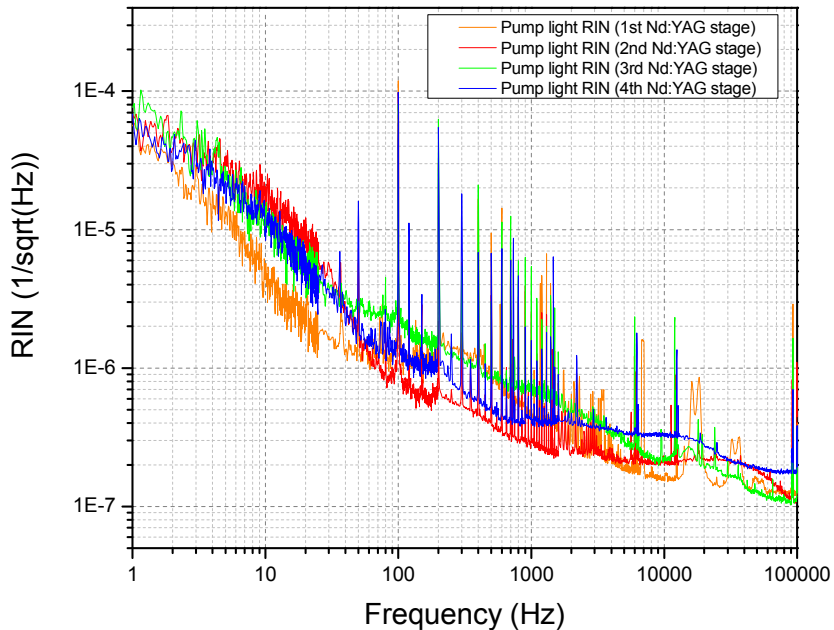
Fig. 4.4 Pump light noise in four Nd:YAG stages (measured by sampling scattered light)

The second technique was to sample out the whole pump beam after the homogenizer, attenuate it, and then focus on the photo-diode. Fig. 4.5 shows a photograph of that experimental setup. This experiment was performed only with one of the Nd:YAG stages, namely the '3rd-stage' in block C. Due to space constraints,

the experiment could not be repeated with the other 3 stages. Fig. 4.8 shows the pump light RIN measured using this technique.
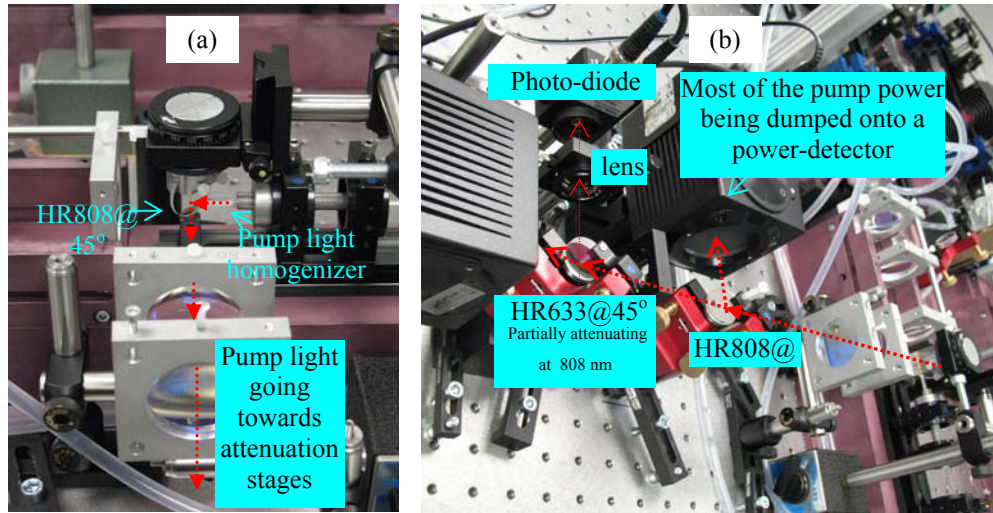
Fig. 4.5 (a) Full pump beam being sampled out; (b) pump light attenuation & noise measurement setup
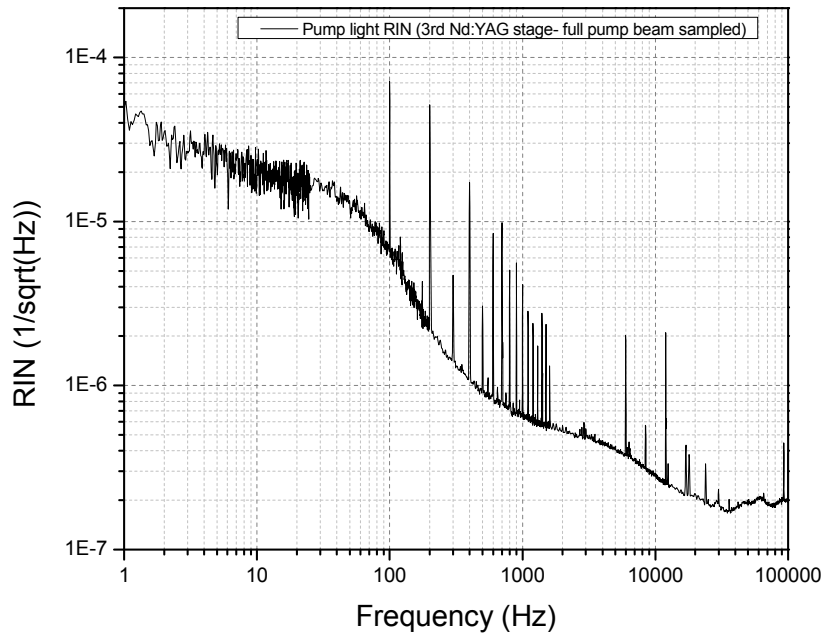
Fig. 4.6 Pump light RIN as measured by sampling out the whole beam.

Given the fact that all the 40 diode modules, equally distributed in 4 boxes, were of identical model, it would not be grossly wrong to assume almost similar kind

of pump light RIN spectra for the other 3 stages, once it was known for one of the Nd:YAG stages.

The RIN results obtained from the 3rd Nd:YAG stage, using these two techniques are compared in Fig. 4.7. It can be clearly observed that the RIN sampled from the whole pump beam was higher than that measured using scattered pump light (especially prominent in the 5 Hz-500 Hz range, but quite similar in the 1 kHz- 100 kHz range). This implies that it would be always better to sample out the whole pump beam for RIN characterization, instead of sampling the scattered parts only. Nevertheless, these experimental results are still very useful in order to have a good estimate of the pump noise levels at different Fourier frequencies.
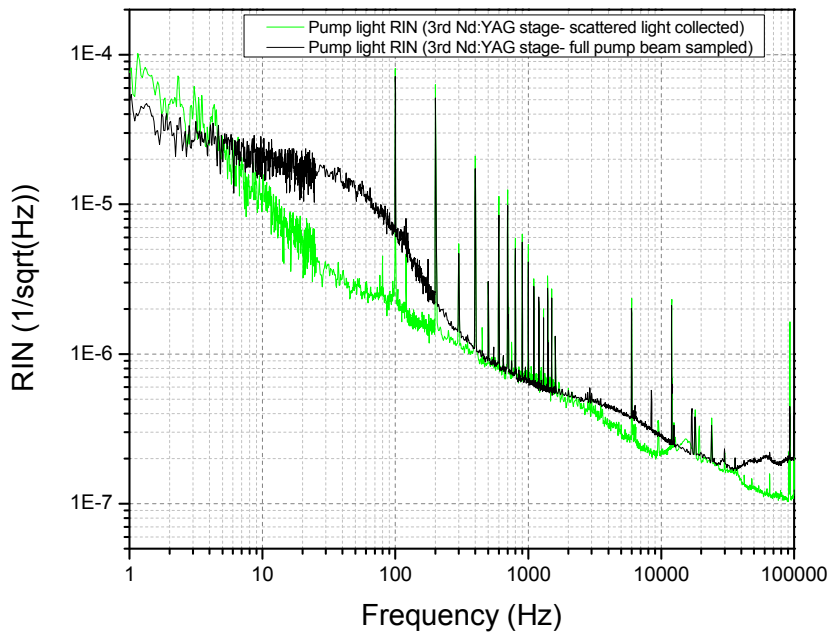
Fig. 4.7 Comparison of the pump light RIN measured by using two different techniques

4.7 RIN of the NPRO, pre-amplifier & amplifier

Fig. 4.8 compares the RINs of the NPRO, output from the pre-amplifier block B and linearly polarized output from the amplifier block B. Please note that the maximum linearly polarized amplifier output power was ∼ 160 W during these experiments. It was found later on that this drop in power, from the optimum 177 W, was due to a degrading pump diode module in the pre-amplifier block A (See

sec. 3.6). However, that should not have had a huge impact in the measurement and comparative study of the RIN in the system.
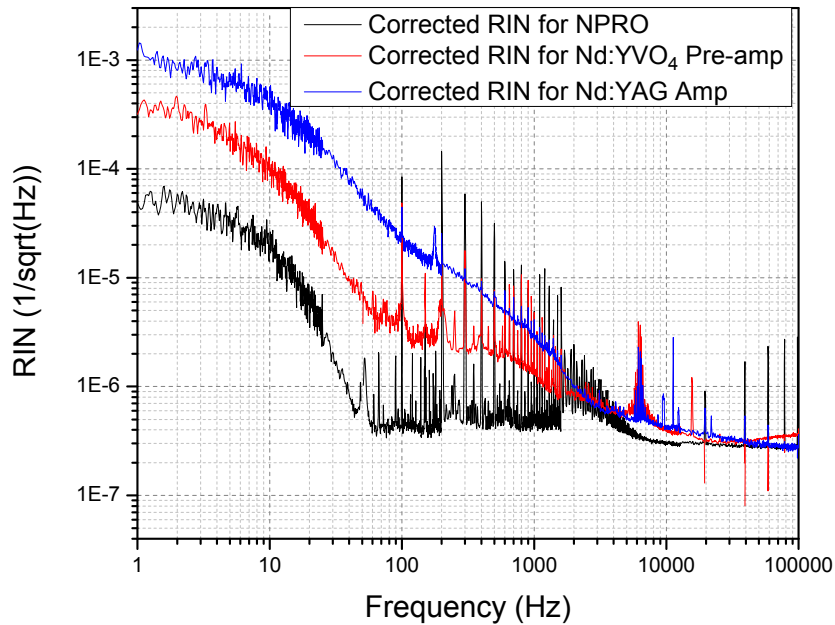
Fig. 4.8 RIN comparison: NPRO seed source, pre-amplifier and amplifier system

From Fig. 4.8, the increase in RIN from the NPRO to the final Nd:YAG amplifier output is clearly visible. It should be noted that the amplifier output RIN and the seed RIN are almost equal in the higher frequency region (2 kHz-100 kHz). This is expected and can be easily explained. The population inversion in the Nd:YAG is easily affected due to the low frequency fluctuations in seed beam. Whereas, given the long upper state life time (~220 µs), the population inversion can not respond to the high frequency fluctuations in the seed beam. Hence the amplifier output RIN almost follows the RIN of the NPRO in the high frequency region.

It was found that the non-stabilized (free running) aLIGO laser output had similar kind of RIN [4.4] as in the case of the solid state MOPA, as shown in Fig. 4.9. Although the MOPA system and the injection locked aLIGO laser system are quite different in principle, the RIN characterization of the MOPA system, performed at 160 W linearly polarized output power level, showed a similar noise spectrum to that of the free running (non-stabilized) aLIGO laser system. Note that, in principle, the MOPA system can also be stabilized by the same acousto-optic modulator (AOM)

based beam stabilization scheme as applied to the aLIGO laser system [4.8]. The archived RIN data from the aLIGO system was kindly provided by Dr. Oliver Puncken, Laser Zentrum Hannover.
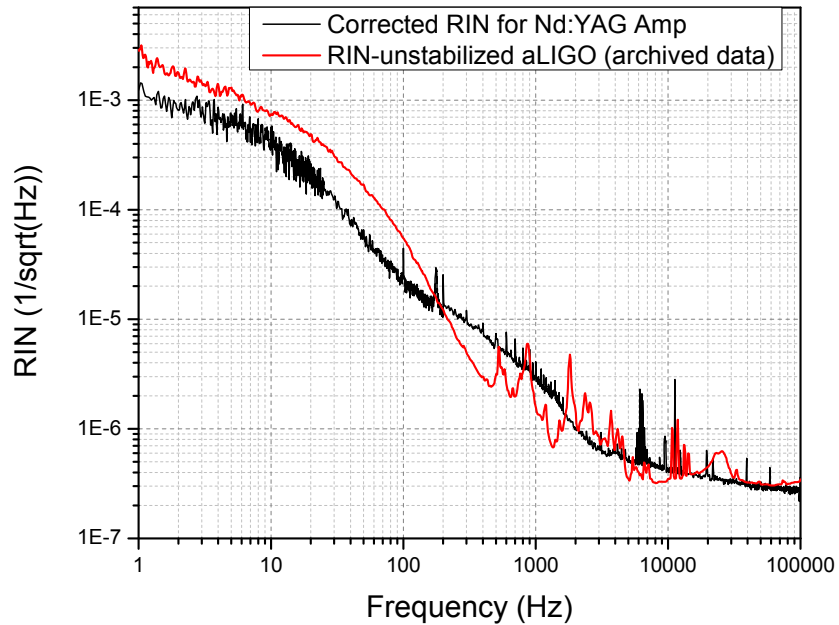
Fig. 4.9 Comparison of RIN: MOPA vs aLIGO free running laser

One interesting finding was that the MOPA output RIN was higher, especially in the 20 Hz-10 kHz range, in case of very low seed power as compared that at higher seed power. This is shown in Fig. 4.10.
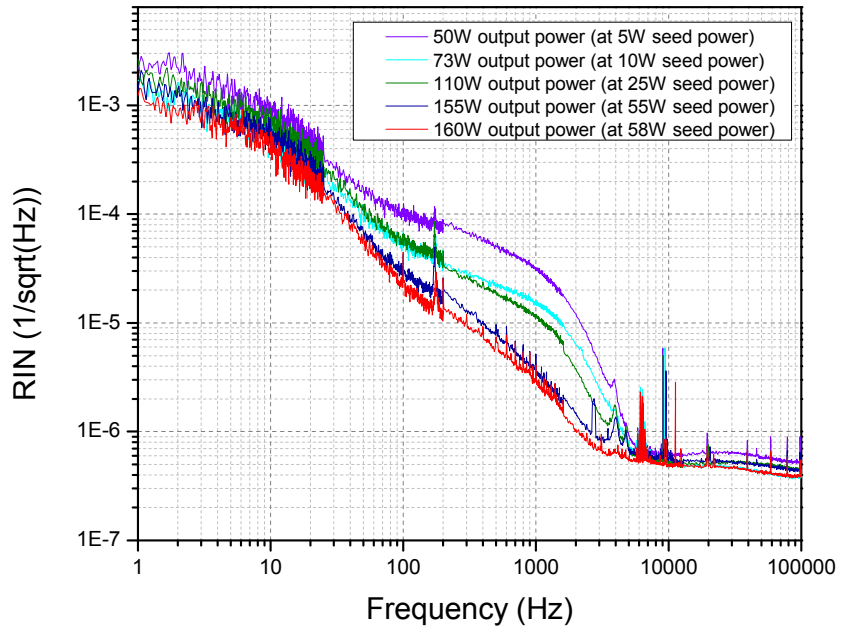
Fig. 4.10 Variation of amplifier output RIN with seed power

The RIN of the output from the pre-amplifier block B was also monitored at low and high seed powers, as shown in Fig. 4.11.
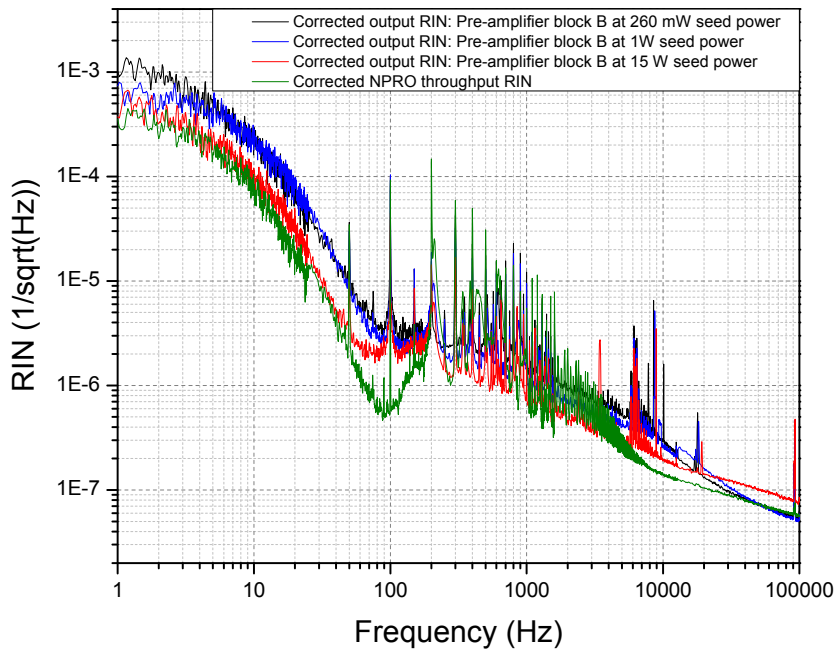
Fig. 4.11 Variation of Pre-amplifier output RIN with seed power

Although the RIN was higher for lower seed power, except in the 20 kHz-100 kHz range, the change in noise spectra did not look similar to the ones seen in Fig. 4.10. Keeping the pump sources of block A switched off, the RIN of the throughput NPRO beam was also measured (just before block B) as shown in Fig. 4.11. Note that the saturated output RIN of block B, at 15 W of seed power, is very close to that of the NPRO throughput in the ~ 1-40 Hz range and, interestingly, a similar trend can be found in Fig. 5 of [4.9] where the RINs of a 4 stage Nd:YVO$_4$ based amplifier output and NPRO were compared. It can be mentioned here that in [4.9] the pump diodes had a maximum rated power of 45 W unlike 75 W in block B described in this thesis.

Also note that the RIN of the NPRO shown in Fig. 4.11 is different than that in Fig. 4.8. The corresponding experiments were performed on different dates and this difference in the RINs could be due to the internal pump source dependent changes in the NPRO noise itself.

For further verification of the seed power dependent change in the output noise spectra in Nd:YVO$_4$, measurement of the RIN of the pre-amplifier block A would have been interesting too. But unfortunately, a pump light delivery fiber in block A burnt out before that measurement could be completed.

Note that the seed spot sizes in the pre-amplifier block A and block B were experimentally optimized but given the pump spot sizes of 500 μm and 600 μm, it can be said that the seed diameters should have been in the range of ~ 400 − 500 μm. In this context, it is worth mentioning that for the Nd:YVO$_4$ crystals concerned, the estimated saturation power for a seed beam with 400 μm diameter would be ~ 1.5 W [9]. Hence, for a seed beam with 500 μm diameter the calculated saturation power should be ~ 2.34 W. From these values, it is obvious that at the standard (full power) operating conditions, all the Nd:YVO$_4$ stages in block A and block B were saturated. On the other hand, the saturation power for a seed beam with a diameter of ~ 1500 μm in the Nd:YAG crystals were ~ 25 W.

In order to segregate any thermal noise due to the 808 nm pump light in the Nd:YAG amplifier system a PM fiber coupled 976 nm diode laser source was tried as a probe source. No resonant absorption related effects are involved when 976 nm light passes through an Nd:YAG crystal and only thermally induced excess RIN, if any, could have been observed while pumping the Nd:YAG crystal at 808 nm, as compared to the RIN without the 808 nm pump light. However, due to the random fluctuation of RIN spectrum of the said probe diode laser (976 nm) itself, the experimental results were inconclusive.

Unfortunately, no current modulator was available to modulate the driving currents of the pump diodes and directly measure the impact on the amplifier output RIN, in terms of a so called 'transfer function' of noise from the pump to the amplifier system. Nevertheless, a simulation was carried out, in order to interpret the experimental results, especially the excess noise characteristics in the amplifier output.

4.8 Simulation of pump and seed noise coupling

The dynamics of noise and gain modulation have been theoretically modeled in [10], for Erbium doped fiber amplifiers (EDFAs). This model analytically calculates the pump-to-signal transfer function as well as the impact of input 'signal modulation' on the output power. Henrik Tünnermann, at the Laser Zentrum Hannover, provided a Python code to simulate this for his experimental EDFA results. That code was modified for calculations in accordance with the 4-level Nd:YAG system and the crystal geometry. Then the output RIN of the 4-stage Nd:YAG amplifier system was simulated. Fig. 4.12 is a simplified schematic description of the noise model.
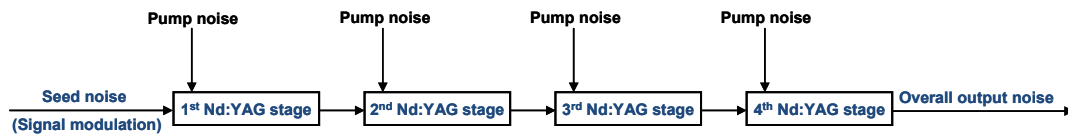
Fig. 4.12 Schematics of pump & seed noise coupling in 4x Nd:YAG amplifier system

The noise (RIN) in the output of the 1st Nd:YAG stage would have contributions from both the input seed noise and the pump noise. This output noise from the 1st stage would act as the seed noise (or signal modulation) for the 2nd stage where, once again, pump noise would couple up, according to the pump-to-signal transfer function. Similar iterations would follow in the 3rd and 4th stage as well. To understand the scheme clearly, let us first have a look at the transfer functions from [10].

Pump noise transfer: $\quad m_p' = \dfrac{m_p B_s [P_p(0) - P_p(L)]}{\sqrt{\omega^2 + \omega_{eff}^2}} \qquad$ Eqn. 4.1

Seed noise transfer: $\quad m_s' = \dfrac{m_s B_s \sqrt{\omega^2 + (\omega_{eff} + K)^2}}{\sqrt{\omega^2 + \omega_{eff}^2}} \qquad$ Eqn. 4.2

Here m_p and m_s are the small fractional modulation amplitudes (i.e. for the linear range) in the pump and seed power levels respectively, ω is the circular frequency of modulation and ω_{eff} is kind of a 'corner frequency' that depends on both material parameters as well as system parameters like seed and pump power levels. $[P_p(0) - P_p(L)]$ is the number of absorbed pump photons along the length L of the active medium concerned. Constant $B_s = (\sigma_{em}/A_{seed})$ where σ_{em} is the emission cross section and A_{seed} is the circular area covered by the seed beam with diameter 1500 μm. Constant $K = B_s[P_s(0) - P_s(L)]$, where $[P_s(L) - P_s(0)]$ is the number of extracted signal photons along the length L of the active medium concerned.

Note that the pump noise modulation and seed noise modulation were incoherent. Hence, to extend the model in [4.10] to a 4 stage Nd:YAG amplifier, the overall output noise of the 1st amplifier stage (i.e. $\sqrt{(m_p')^2 + (m_s')^2}$) was taken as the seed modulation for the 2nd stage and so on.

In the simulation, the input/ seed power and the final output power were set to be 60 W and 180 W respectively. Experimental seed RIN (output from block B), as shown in Fig. 4.13, was used for the simulations. The pump light RIN spectrum measured by fully sampling out the pump beam in the 3rd stage was repeatedly used for all the Nd:YAG stages in the simulations.

Fig. 4.13 shows the simulated output RINs for 1 W & 60 W seed power. Also the pump light RIN and the seed RIN are shown. Since the pump-light RIN is lower than that of the seed, the simulated trend almost follows what has been shown mathematically in sec. 4.3. The amplifier output RIN is at maximum in the small signal gain region (at 1W of seed power in this case) but gets suppressed when the amplifier approaches saturation (at 60 W of seed power in this case).
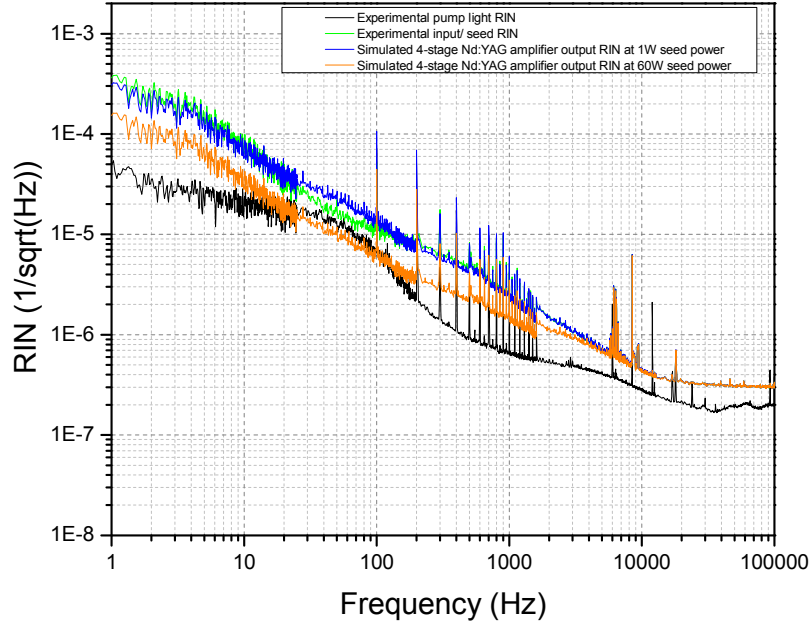
Fig. 4.13 Simulated amplifier output RIN at low and high seed power levels.

It can be clearly seen that at 1W of seed power, the simulated amplifier output RIN matches well with the seed RIN level. Also, the amplifier output RIN at a much higher seed power (60 W) is lower than the seed RIN for a wide frequency range of ~ 1 Hz- 3 kHz. Whereas, the amplifier output RIN, at both low and high seed power levels, match with the seed RIN in the high frequency region (3 kHz-100 kHz), as expected from theory described in sec. 4.3.

The RIN of the output of the pre-amplifier block B was slightly higher while measured just before the Nd:YAG amplifier system (Fig. 4.13, green plot), as compared that measured by direct sampling of the output (Fig. 4.8 and 4.11, red plot). Since the output from pre-amplifier block B passes through various optics and

especially a high power Faraday Isolator with Terbium Gallium Garnet (TGG) crystal, before reaching to the amplifier block C, this slight excess noise could possibly be attributed to the absorption process (at 1064 nm) in the TGG crystal mainly. TGG crystals are reported to show some thermal issues due to such absorption [4.11].

In Fig. 4.13, in the frequency range of ~ 20 Hz-100 Hz, the simulated output RIN for 60 W seed is below the pump RIN and apparently this may be hard to accept.

However, keeping in mind the slope (output power vs pump power) characteristics of a 4-level amplifier system at high seed power [4.12], this is definitely feasible. To clarify this point, a hypothetical linear plot is sketched and shown in Fig. 4.14 followed by some simple mathematical steps.
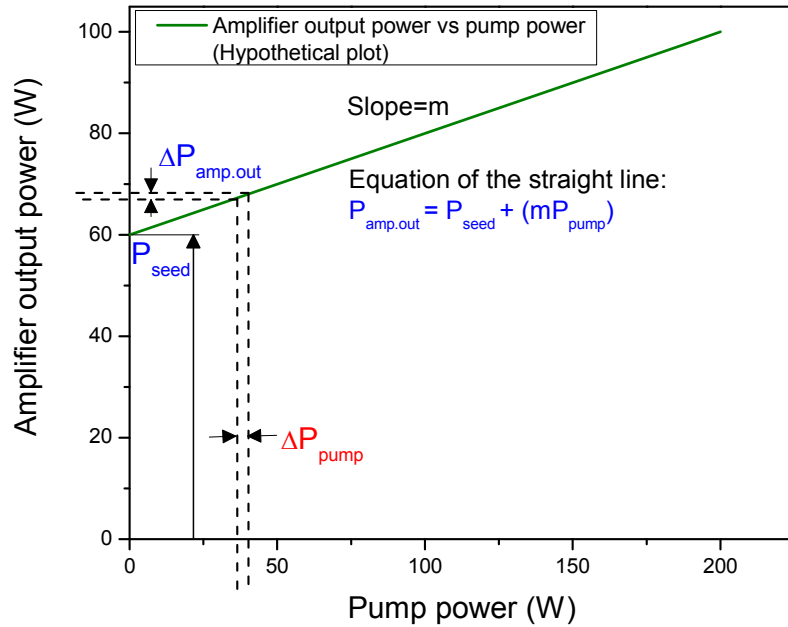
Fig. 4.14 A hypothetical plot of amplifier output power vs pump power in a 4-level system

For the low frequency regime, keeping the picture in mind from Fig. 4.14, if we further assume the seed to be noise free then, the amplifier output power ($P_{amp.out}$) experiences an absolute noise of $\Delta P_{amp.out} = m \cdot \Delta P_{pump}$ corresponding to a small modulation of ΔP_{pump} in the pump power. As $P_{amp.out} = P_{seed} + (m \cdot P_{pump})$, we can write down the following equation:

$$\frac{\Delta P_{amp.out}}{P_{amp.out}} = \frac{m \cdot \Delta P_{pump}}{P_{seed} + (m \cdot P_{pump})}$$

or,

Amplifier output RIN, $\dfrac{\Delta P_{amp.out}}{P_{amp.out}} = \dfrac{(\Delta P_{pump} / P_{pump})}{1 + (P_{seed} /(m \cdot P_{pump}))}$ Eqn. 4.3

As $\dfrac{\Delta P_{pump}}{P_{pump}}$ = Pump RIN, we can certainly infer from Eqn. 4.3 that the amplifier output RIN can be lower than the pump RIN (i.e. $\dfrac{\Delta P_{amp.out}}{P_{amp.out}} < \dfrac{\Delta P_{pump}}{P_{pump}}$) under the aforementioned conditions/assumptions.

Now, let us compare the simulated RINs with the experimental RINs in Fig. 4.15. Note that for this experiment, the minimum seed power level of ~ 5 W was chosen in order to avoid different attenuation optics that would be required in front of the photo-diode for a 1 W of seed beam. In other words, using the same attenuation optics, the measurements could be performed at the minimum of ~ 5 W and maximum of ~ 58 W seed power levels.

In Fig. 4.15, one can clearly observe that both for low (~5W, measured) and high seed power (~58 W, measured) levels corresponding to ~50 W & ~160 W output power levels respectively, the experimentally obtained RINs were significantly higher than that of the simulated ones. This kind of excess noise in the Nd:YAG amplifier system is not well explained so far but might be due to spectral instability/ noise of the pump light sources. Given the narrow absorption bandwidth of Nd:YAG centred at 808 nm, any spectral fluctuation in the pump light can have serious impact on the population inversion and hence on the amplification dynamics, resulting in some excess output RIN which can not be directly estimated from the pump light RIN and seed RIN. However, a high resolution (say, 0.1 nm) diffraction grating can be used to resolve the spectra of the pump light and compare the real-time relative power fluctuations between two diffraction maximas. The amount of such relative power

fluctuations will possibly indicate whether spectral fluctuation in the pump light could have a significant impact on the RIN of the Nd:YAG amplifier system.
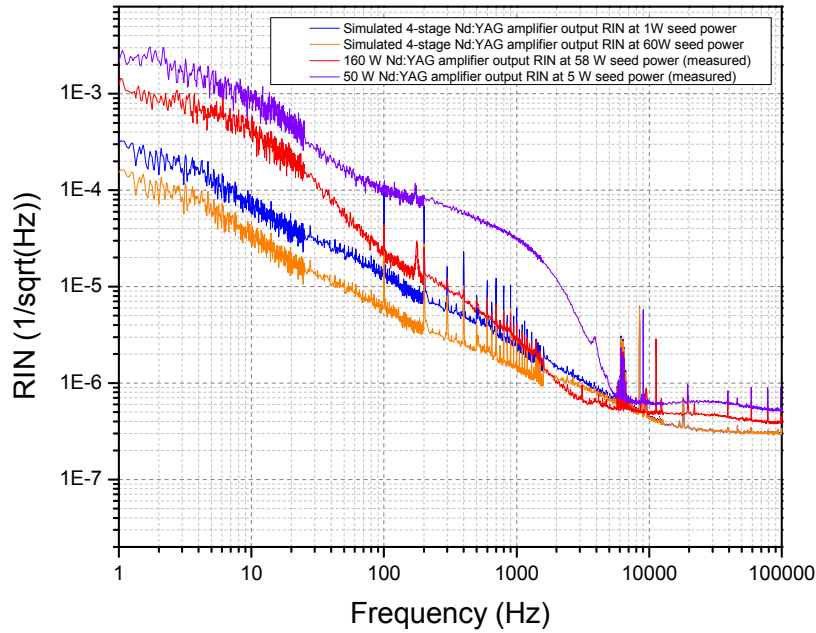
Fig. 4.15 Comparison of simulated and experimental RIN of the Nd:YAG amplifier system

4.9 Conclusion

The intensity noise transfer characteristics of a saturable gain amplifier have been discussed in brief. The Relative Intensity Noise (RIN) of the 808 nm pump light sources, the NPRO seed, the Nd:YVO$_4$ based pre-amplifier system and the 4 stage Nd:YAG amplifier system have been measured and compared. Low-pass-filter like behaviour of an amplifier gain medium in response to seed/signal modulation has been explained.

Variation of the output RIN with seed power has been experimentally observed in both the pre-amplifier block B and amplifier block C. It was found that the output RIN was highest at the lowest seed power. In the Nd:YAG based amplifier system, the RIN at low seed power looked a bit peculiar, with a 'bumpy' rise in the 100 Hz- 5 kHz range (log-log scale). This could be a vague indication to some kind of corner frequency around ~ 2 kHz but could not be explained so far and hence demands for further investigation.

A simulation on the pump and seed noise coupling and its effect on the RIN of the Nd:YAG amplifier system has been presented and tallied with the experimental results. The experimental output RIN was considerably higher than the simulated one.

It must be noted that the experimental output RIN of the Nd:YAG amplifier system was higher than both the pump light RIN and seed RIN. Similarly, the output RIN of the pre-amplifier block B was higher than that of the NPRO. Such excess output RIN could possibly be a result of spectral fluctuations in the pump light.

In short, overall RIN characterization of the MOPA system was conducted experimentally. The output RIN of the MOPA system was found to be very similar to that of the free-running aLIGO laser system.

References Ch.4

4.1) F Seifert, P Kwee, M Heurs, B Willke and K Danzmann: Laser power stabilization for second generation gravitational wave detectors; Optics Letters, Vol. **31**, No. 13, 2006

4.2) P Kwee, B Willke and K Danzmann: Shot-noise-limited laser power stabilization with a high-power photo-diode array; Optics Letters, Vol. **34**, No. 19, 2009

4.3) P Kwee, B Willke and K Danzmann: Laser power noise detection at the quantum-noise limit of 32 A photocurrent; Optics Letters, Vol. **36**, No. 18, 2011

4.4) L Winkelmann, O Puncken, R Kluzik, C Veltkamp, P Kwee, J Poeld, C Bogan, B Willke, M Frede, J Neumann, P Weßels and D Kracht: Injection-locked single-frequency laser with an output power of 220 W; Applied Physics B, Vol. **102**: p 529-538, 2011

4.5) H Vahlbruch, A Khalaidovski, N Lastzka, C Graf, K Danzmann and R Schnabel: The GEO 600 squeezed light source; Classical and Quantum Gravity, Vol. **27**, 084027 (8pp), 2010

4.6) The LIGO Scientific Collaboration, "A gravitational wave observatory operating beyond the quantum shot-noise limit," Nature Physics (Letter), Vol. **7**, p 962–965, 2011

4.7) T C Larason and S S Bruce, "Spatial uniformity of responsivity for silicon, gallium nitride, germanium, and indium gallium arsenide photodiodes," Metrologia, Vol. **35**, p 491-496, 1998

4.8) P Kwee, C Bogan, K Danzmann, M Frede, H Kim, P King, J Pöld, O Puncken, R L Savage, F Seifert, P Wessels, L Winkelmann and B Willke, "Stabilized high-power laser system for the gravitational wave detector advanced LIGO," Optics Express **20**, p 10617-10634 (2012)

4.9) M Frede, B Schulz, R Wilhelm, F Seifert, P Kwee, B Willke and D Kracht, "Fundamental mode, single-frequency laser amplifier for gravitational wave detectors," Optics Express, Vol. **15**, 2007, p 459-465

4.10) S Novak and A Moesle: Analytic model for gain modulation in EDFAs; Journal of Lightwave Technology, Vol. **20**, No. 6, 2002

4.11) E A Khazanov, O V Kulagin, S Yoshida, D B Tanner and D H Reitze: Investigation of Self-Induced Depolarization of Laser Radiation in Terbium Gallium Garnet; IEEE Journal of Quantum Electronics, Vol. **35**, No. 8, 1999

4.12) A K Sridharan, S Saraf, S Sinha and R L Byer, "Zigzag slabs for solid-state laser amplifiers: batch fabrication and parasitic oscillation suppression," Applied Optics **45**, p 3340-3351 (2006).

Ch.5 Aberrations and wavefront sensing

5.1 Introduction

It is well known that the beam quality of high power end-pumped solid state lasers degrades due to thermally induced aberrations [5.1-5.4]. Since it was clearly evident from the simulations (see sec. 3.7) and experiments (see Table 3.2) that the degradation of TEM$_{00}$ mode content in the Nd:YAG amplifier output could not be attributed to gain saturation only, it was obvious to assume a significant role of thermal aberrations behind the beam quality degradation. This demanded for the characterization of aberrations in the amplifier system.

In this chapter, firstly the basics of Zernike aberration polynomials and Shack-Hartman wavefront sensor will be covered. Then the results from experimental measurements of thermal lens power and primary spherical aberration in an Nd:YAG amplifier stage, using a probe 976 nm diode laser, will be reported. Also, simulations of the thermal lens power and an estimation of beam quality degradation due to spherical aberration will be described. Scaling of Zernike coefficients with different pupil radii will be discussed.

5.2 Thermal aberrations and degradation in beam quality

Thermally induced variation of refractive index *n=n(r)* in end-pumped rod lasers or amplifiers depends on the combined effect of the pump light distribution and the crystal cooling architecture, which create a temperature gradient inside the active media. An ideal thermal lens must have a parabolic shape which does not have any

impact on the output beam quality (excluding birefringence in Nd:YAG). In reality, non-uniform heat load profile, the temperature dependent heat conductivity and stress dependent variations of the refractive index result in an aberrated thermal lens. Under the assumptions of temperature independent thermal conductivity (K) and homogenous pumping, for a segmented YAG/ Nd:YAG/ YAG (undoped 7mm/40mm doped/ undoped 7mm) rod, the bulging effect induced by thermal stress at the end facets can be neglected and the focal length of the thermal lens ($f_{r,\varphi}$) can be approximated as the follows [5.4]:

$$f_{r,\varphi}^{-1} \approx \frac{P_h}{KA}(\frac{1}{2}\frac{dn}{dT} + \alpha C_{r,\varphi} n_0^3) \qquad \text{Eqn. 5.1}$$

Symbol	Term	Numerical values
P_h	Absorbed heat power	variable
K	Thermal conductivity	$\sim$ 10-14 W m^{-1} K^{-1}
A	Area of the rod	7.0685 mm^2
$\frac{dn}{dT}$	Temperature dependence of refractive index	$\sim$10x10^{-6}
α	Thermal expansion coefficient	7-8x10^{-6}
$C_{r,\varphi}$	Photo-elastic coefficients (radial and tangential)	See [5.5]
n_0	Unperturbed refractive index (at the centre of the YAG rod)	1.82

Table 5.1: Description of the terms in Eqn. 5.1

It is very difficult to pick up the right values for *K* and the refractive index gradient (*dn/dT*) as a range of values can be found in scientific literature [5.6-5.9]. Moreover, *K* and (*dn/dT*) both can vary with temperature [5.10, 5.11]. Still, some widely circulated values [5.9] have been assigned here in Table 5.1 for the estimation of thermal lens. Note that in the LZH Rod Designer (LRD) software the value used is *K*=11.94 W m^{-1} K^{-1}. The second term ($\alpha C_{r,\varphi} n_0^3$) in eqn. 5.1 indicates stress induced birefringence (i.e. different refractive indices for the radially and tangentially polarized components of the seed beam). However, pair-wise depolarization compensation (See *Ch.3*) is already in place and this chapter will focus only on the polarization-independent effects of thermal lensing.

As mentioned before, an ideal thermal lens does not affect beam quality. Beam quality degrades due to the higher order aberrations like spherical aberration, coma etc. The reader can find a detailed description on various kinds of aberrations in any standard text book like [5.12]. Such aberrations distort the phase profile of the amplified seed beam in such a manner that the far field irradiance shows deviation from pure Gaussian profile. In other words, when a purely fundamental TEM_{00} laser beam is propagated through an aberrating optical system, the output is no longer purely TEM_{00}.

Aberration to planar wavefronts is shown below with simplified schematics in Fig. 5.1.
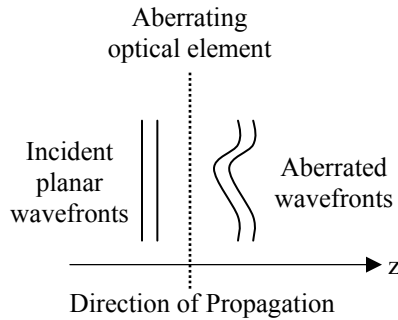
Fig. 5.1: Schematic description of aberration to normal wavefronts

Any non-quadratic function of r that modifies the incident phase-front causes beam degradation. Hodgson and Weber showed [5.13] that spherical aberration, a quartic function of r, can be present in thermal lenses in rod type active media, due to the variation of thermal conductivity with temperature and inhomogeneous pump distribution. In their calculation, the phase shift depends on both the spatial heat intensity profile and the thermal conductivity expressed in the form of $K(T)=a/T$, where a is a material constant (W/cm) and T is the temperature in absolute scale. Finally the phase shift function takes the following form: $\Phi(r)=\varepsilon[1-\zeta r^2]r^2$, where ε and ζ are constants. Here the spherical aberration term is $\varepsilon\zeta r^4$. As compared to tip, tilt or astigmatism, spherical aberration is very hard to correct and a significant amount of beam degradation could be inevitable. This chapter will emphasize on the ideal thermal lensing term (defocus: phase shift proportional to r^2) and the spherical aberration (phase shift proportional to r^4). Naturally the overall aberration can be

resolved into several characteristic components or basis functions of *r,φ (φ-azimuthal angle*) and there are various standard methods available for wavefront analysis. Optical designers quite often use Seidel polynomials (developed in the mid-19th centrury) whereas interferometrists prefer Zernike polynomials (developed in the early 20th century) [5.14].

It should be noted that astigmatism, although a higher order aberration, does not affect the beam quality but makes the beam waist (x-waist, y-waist) focused at different planes perpendicular to the z-direction. In other words, astigmatism makes the 2-D beam profile elliptical. Although the beam quality is not affected, given the mode matching technique (with two spherical lenses) used in the DBBL, astigmatism can potentially affect the calculation of the TEM_{00} mode content by comparing the elliptical profile with a single circular Gaussian profile.

Since good optical alignment was ensured and no significant asymmetric off-the –axis patterns were seen besides the round Gaussian beam profile, effects of coma could also be neglected safely in this context.

5.3 Zernike polynomials

Zernike polynomials are named after Nobel laureate Fritz Zernike. These polynomials are extensively used for aberration characterization in optical imaging instruments, adaptive optics and various other areas. The most interesting features of these polynomials are that i) the radial and azimuthal parts are separable and ii) each radial polynomial is orthogonal to other radial polynomials and each azimuthal polynomial is orthogonal to other azimuthal polynomials, all defined within a unit circle. The Zernike polynomials in the polar coordinates can be written as [5.15]:

$$Z_n^m(\rho,\varphi) = \begin{cases} N_n^m R_n^{|m|}(\rho)\cos(m\varphi); & m \geq 0, 0 \leq \rho \leq 1, 0 \leq \varphi \leq 2\pi \\ N_n^m R_n^{|m|}(\rho)\sin(m\varphi); & m < 0, 0 \leq \rho \leq 1, 0 \leq \varphi \leq 2\pi \end{cases}$$

$$\forall n, m \in \mathbb{Z}$$

For a given *n, m* can only take these values: *-n, -n+2, -n+4, ..., n;*

The normalizing factor, $N_n^m = \sqrt{\dfrac{2n+1}{1+\delta_{0m}}}$ where $\delta_{0m} = \begin{cases} 1; m = 0 \\ 0; m \neq 0 \end{cases}$

The radial function, $R_n^{|m|}(\rho) = \displaystyle\sum_{k=0}^{(n-|m|)/2} \dfrac{(-1)^k (n-k)!}{k!(((n+|m|)/2)-k)!(((n-|m|)/2)-k)!}$

These polynomials can be easily represented in Cartesian coordinates as well [5.16] and that is generally the case while handling experimental data from most of the standard wavefront sensors. Some of the important Zernike polynomials in polar co-ordinates are listed in Table 5.2. Some 2D profiles of Zernike terms are shown in Fig. 5.2.

Order	Frequency		
n	m	$Z_n^m(\rho,\theta)$	Physical description
0	0	1	Constant: Piston
1	-1	$2\rho\sin(\theta)$	y-Tilt
1	1	$2\rho\cos(\theta)$	x-Tilt
2	-2	$\sqrt{6}\rho^2\sin(2\theta)$	Astigmatism with axis at $\pm 45°$
2	0	$\sqrt{3}(2\rho^2-1)$	Field curvature/ defocus
2	2	$\sqrt{6}\rho^2\cos(2\theta)$	Astigmatism with axis at $0°$ or $90°$
3	-3	$\sqrt{8}\rho^3\sin(3\theta)$	
3	-1	$\sqrt{8}(3\rho^3-2\rho)\sin(\theta)$	y-Coma
3	1	$\sqrt{8}(3\rho^3-2\rho)\cos(\theta)$	x-Coma
3	3	$\sqrt{8}\rho^3\cos(3\theta)$	
4	-4	$\sqrt{10}\rho^4\sin(4\theta)$	
4	-2	$\sqrt{10}(4\rho^4-3\rho^2)\sin(2\theta)$	Secondary astigmatism
4	0	$\sqrt{5}(6\rho^4-6\rho^2+1)$	Spherical aberration with defocus

Table 5.2 A few important Zernike polynomials
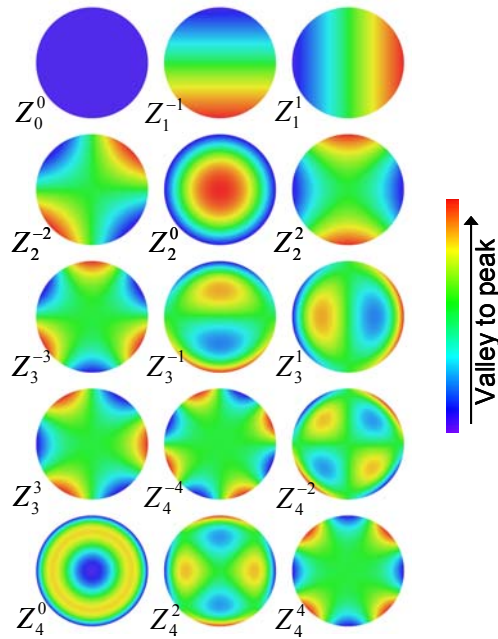
Fig. 5.2 The Zernike aberration profiles. This retouched picture was generated from a modified C code originally written by Rocchini and available on Wikipedia under the GNU Free Documentation License version 1.2 (Attribution: Zom-B at en.wikipedia)

5.4 Principle of wavefront analysis with Shack-Hartmann wavefront sensor

There are various wavefront sensing tools and the Shack-Hartmann wavefront sensors (SHWS) are perhaps the most common ones. The key components of a SHWS are a microlens array and a CCD or CMOS chip (along with necessary electronics). The overall laser beam incident on the SHWS is spatially sampled by tiny lenslets on a microlens array. Each lenslet focuses the incident part of the beam on the CCD chip. An important point to note here is that these individual focal points are spatially distributed in accordance with the direction of the surface normals of the sample parts of the incident wavefront. This is described schematically in Fig. 5.3-5.4. In Fig. 5.3 planar wavefronts are incident on the SHWS and certain focal points are created on the CCD chip. Fig. 5.4 is an exaggerated pictorial description of a situation where an aberrated wavefront is incident on the microlens array and some deviated focal points corresponding to each lenslet are created. Please note that only 1 dimensional (keeping $x=x_0$ fixed) aberration is shown here for simplicity. In reality, the shifts in focal spots will take place in 2 dimensions (x,y). The displacements in

the focal points with respect to that of the original ones (x_i,y_j) for a planar wavefront are stored in a 2-D array δ[x][y]. It is worth mentioning that one does not necessarily need a purely planar wavefront for reference. Any arbitrary wavefront data or in other words, 'spot-field' distribution, can be stored as reference and further variation or aberration to that original wavefront can be monitored with respect to the stored reference points. Now, in order to understand the overall wavefront structure, some mathematical steps involving these discrete displacement values are necessary.
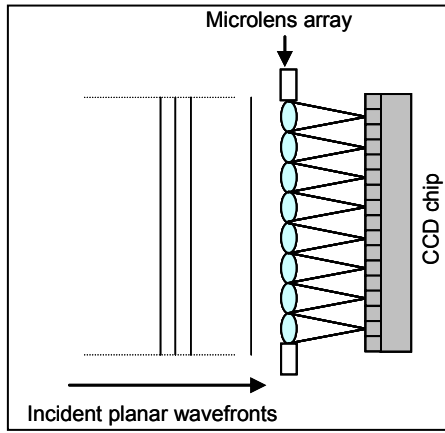
Fig. 5.3 Planar wavefronts on microlens array   Fig. 5.4 Aberrated wavefront and deviated foci
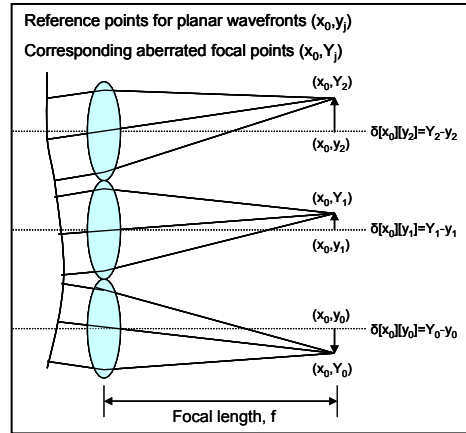
For each lenslet (generally circular) in the microlens array, we can assume a square surrounding it uniformly and the projection of this square on the CCD chip can be considered as one 'Area of Interest' (AOI). The red coloured square in Fig. 5.5 depicts such an AOI in an exaggerated view. Sometimes this AOI is also termed as a 'sub-aperture' for the corresponding lenslet. We need to know the intensity centroid for each AOI and that can be determined as follows [5.17]. Say, we are going to measure the position of the focal spot or the intensity centroid ($x_{c,k}$,$y_{c,k}$) of the kth AOI. Then,

$$x_{c,k} = \frac{\sum\limits_{i,j \in AOI_k} x_{i,j} I_{i,j}}{\sum\limits_{i,j \in AOI_k} I_{i,j}} \quad ; \quad y_{c,k} = \frac{\sum\limits_{i,j \in AOI_k} y_{i,j} I_{i,j}}{\sum\limits_{i,j \in AOI_k} I_{i,j}} \qquad \text{Eqn. 5.2}$$

The aforementioned definition of the centroid is nothing but the intensity weighted mean location of the centre of the spot. In some cases (e.g. in Mr.Beam^{TM} software used with the SHWS), the intensity centroid is determined by replacing $I_{i,j}$ with $I_{i,j}^{2}$ in eqn. 5.2, in order to avoid cross-talk between neighbouring focal spots.
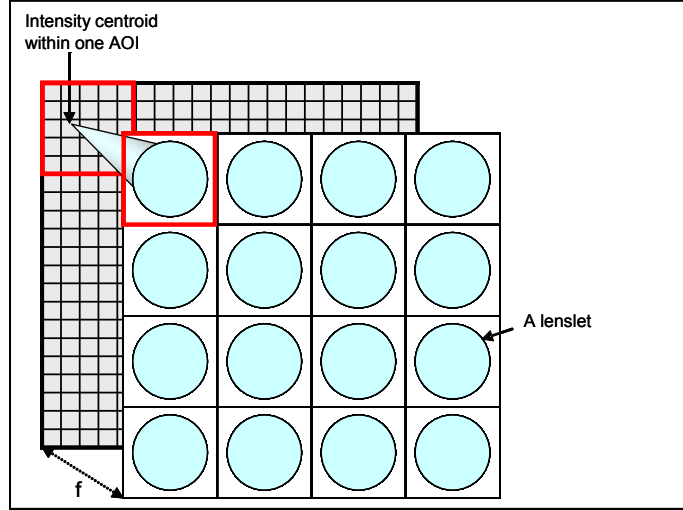
Fig. 5.5 Magnified schematics of the Microlens array AOI

Now, let us define a general aberrated phase function, $\Phi(x,y)$, in the Cartesian co-ordinates as follows:

$$\Phi(x, y) = \frac{2\pi}{\lambda} W(x, y)$$

Where λ is the wavelength concerned and $W(x,y)$ is the path difference between the aberrated test beam and the corresponding reference beam, measured at (x,y).

At this point, we are ready to measure the slope of $W(x,y)$ at the kth AOI as follows:

$$\begin{bmatrix} (\partial W / \partial x) \\ (\partial W / \partial y) \end{bmatrix}_k = \begin{bmatrix} \beta_{x,k} \\ \beta_{y,k} \end{bmatrix} \approx \frac{1}{f} \begin{bmatrix} (x_{c,k} - x_{ref,k}) \\ (y_{c,k} - y_{ref,k}) \end{bmatrix} \quad \text{Eqn. 5.3}$$

$(x_{ref,k}, y_{ref,k})$ is the intensity centroid of the reference beam at the kth AOI and f is the focal length of a lenslet. In general the gradient can be represented as:

$$\vec{\nabla}W = \frac{\partial W}{\partial x}\hat{i} + \frac{\partial W}{\partial y}\hat{j}$$

Here, $\hat{i}$ and $\hat{j}$ are the unit vectors in the x and y directions respectively.

In the modal reconstruction method [5.17], $W(x,y)$ can be represented as a linear and weighted combination of various polynomials (e.g. Zernike polynomials) as follows:

$$W(x, y) = \sum_{l=1}^{M} c_l P_l(x, y) \quad \text{Eqn. 5.4}$$

Where the coefficient c_l is the weight of the polynomial $P_l(x, y)$ and the expansion has been carried upto the Mth term of the polynomial. It is worth mentioning that the transformation of the coefficients from a 2-index system (n,m) to a single index system (l) does not affect the reconstruction method and is done just for simplicity. Unfortunately the choice of such single indices varies in literature. One author may represent the Zernike defocus coefficient as C_3 whereas another may represent the same as C_4 or so. According to the ANSI Standard:

$$\text{Mode number}, l = \frac{n(n+2)+m}{2}$$

Now from eqn. 5.3, the slope functions for the kth AOI can also be written in terms of the analytical derivates as given below:

$$\begin{bmatrix}(\partial W/\partial x)\\(\partial W/\partial y)\end{bmatrix}_k = \begin{bmatrix}\sum_{l=2}^{M} c_l \dfrac{\partial P_l(x,y)}{\partial x}\\\sum_{l=2}^{M} c_l \dfrac{\partial P_l(x,y)}{\partial y}\end{bmatrix}$$

A mathematically significant point to note here is that such polynomials have analytical derivates which will be very helpful in fitting the experimental discrete datasets. For the purpose of fitting, we can define χ^2 as follows:

$$\chi^2 = \sum_k \left(\beta_{x,k} - \sum_{l=2}^M c_l \frac{\partial P_l(x,y)}{\partial x} \right)^2 + \sum_k \left(\beta_{y,k} - \sum_{l=2}^M c_l \frac{\partial P_l(x,y)}{\partial y} \right)^2$$

The next task is to minimize χ^2 by finding the solutions of the system of equations from $\frac{\partial \chi^2}{\partial c_l} = 0$.

It should be noted that Zernike mode normalizing factors (like $\sqrt{3}$ for defocus, $\sqrt{5}$ for 3rd order spherical aberration) are already embedded in the Zernike coefficients provided by the *LZH Rod designer* (LRD) software and the SHWS software (Mr.Beam[TM]).

5.5 The experimental setup

The wavefront sensing experiments reported in this chapter were carried out using a SHWS designed by Laser Laboratorium Göttingen e.V. and manufactured by LOT-Oriel GmbH & Co. KG, Germany. The technical details are given below in Table 5.3. The SHWS comes with proprietary software, Mr. Beam[TM] for automatic data acquisition and analysis.

SHWS (Model: LLG-WFS 02): CCD camera with an integrated microlens array and software for the beam analysis. 12bit camera with USB 2.0 interface.	2/3" CCD chip (Sony) - Active area approximately 10.2 mm x 8.3 mm - Resolution 1392 x 1040 pixels - Pixel size of 6.45 μm - Spectral sensitivity of 350 nm to 1100 nm - Refresh rate up to 8 Hz, externally triggered	Microlens array - Dimensions 12 mm x 12 mm - Focal length 3.5 mm - Lens size 150 μm x 150 μm - Fill factor:> 95% - Subapertures: max. 50 x 40 - Wavefront-resolution $\sim \lambda/10$ per subaperture (633 nm) -Wavefront dynamics $\sim 5\lambda$ per sub-aperture, $\sim 150\,\lambda$ total

Table 5.3 Technical details of the SWHS

The experimental setup is schematically shown in Fig. 5.6. A 200 mW diode laser source, operating at 976 nm, was used as a probe for these experiments. Nd:YAG does not have any absorption or emission at 976 nm and hence the choice of the probe wavelength was justified. This diode laser comes with a fiber pigtail and offers single mode output. The output from the fiber pigtail was collimated to achieve the right spot sizes, keeping in mind the dimension of the Nd:YAG rod (3 mm in diameter). It should be noted that the precision of any SHWS, for a given incident beam size, is highly dependent on the number of lenslets sampling the wavefront, the fill factor, pixel size on the CCD and the focal length of the lenslets. Since these parameters are constant for a given SHWS, one has to increase the incident beam size subjected to the limited active area on the microlens array or the CCD. A small spot size of the incident beam means lesser number of sampling AOIs and hence the results would be more prone to numerical fitting errors. The probe beam diameter inside the Nd:YAG rod should not be more than ~ 1500 μm in order to avoid clipping and losses. In fact, the best operating seed spot diameter of the actual seed (1064 nm) in the amplifier system was ~1500 μm (See sec. 3.6).
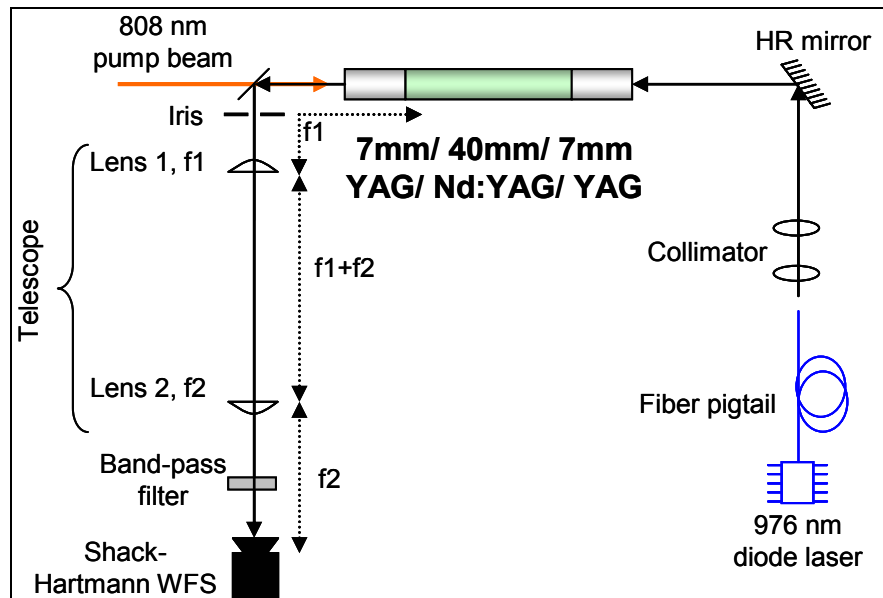
Fig. 5.6 Schematic description of the experimental setup for aberration characterization

For the purpose of imaging the thermal lens created inside the Nd:YAG rod due to the 808 nm pump, a telescope with two lenses had to be built. Changing the lenses and hence focal lengths (f1 & f2) one can set the magnification factor $|m|=f2/f1$ of the telescope. This magnification is very helpful in order to have a larger beam spot on the SHWS.

In order to see what happens to the complex q parameter of a Gaussian beam when it goes through a telescope, the ABCD matrices were constructed as given below.

$$A_{telescope} = \begin{bmatrix} 1 & f2 \\ 0 & 1 \end{bmatrix} \cdot \begin{bmatrix} 1 & 0 \\ -\dfrac{1}{f2} & 1 \end{bmatrix} \cdot \begin{bmatrix} 1 & f1+f2 \\ 0 & 1 \end{bmatrix} \cdot \begin{bmatrix} 1 & 0 \\ -\dfrac{1}{f1} & 1 \end{bmatrix} \cdot \begin{bmatrix} 1 & f1 \\ 0 & 1 \end{bmatrix}$$

$$= \begin{bmatrix} m & 0 \\ 0 & \dfrac{1}{m} \end{bmatrix} \quad \text{where, } m = -\dfrac{f2}{f1}$$

$$\Rightarrow q_{output} = m^2 q_{input}$$

The calculation above indicates that the radius of curvature and the beam waist of the input Gaussian beam will scale up m^2 times and $|m|$ times respectively, at the output image plane of the telescope. Hence the normalizing radius or evaluation radius, r_{eval} would scale up $|m|$ times while characterizing the output beam from the telescope, as compared to that without a telescope. If we neglect any intrinsic aberration in the telescope, the magnification itself should not ideally have any impact on the Zernike polynomial fitting on the SHWS, apart from changing signs of the coefficients of the radially asymmetric Zernike terms (e.g. tilt or coma) due to a negative m [5.18].

It should be noted that for these experiments one of the four Nd:YAG stages of the amplifier block C was used and the pump optics, water cooling chamber are not shown in Fig. 5.6 above for simplicity. Also note that the probe beam went through an iris before hitting 'Lens 1' of the telescope. This was done in order to minimize the amount of stray 808 nm light and fluorescence entering the telescope. A Thorlabs FB980-10 band-pass filter was used before the SHWS in order to eliminate all unwanted wavelengths. Otherwise, stray lights could have disastrous impact on the

measurements. Special care was taken to shield the camera from stray lights using mechanical barriers and the ceiling lights in the lab were switched off.

One important parameter to set on the software was the exposure time. Shorter exposure time means faster calculation of the data acquired and it can also help get rid of some stray light which could be inevitably integrated over a long exposure time. The exposure time and the optical power of the probe beam was chosen in such a way that the CCD camera was below saturation and also no light spots, other than the ones from the probe itself, were seen by the camera.

Given the round spot size of the probe beam on the camera, a circular portion of the grid covering all the active AOIs was selected for the calculations and rest of the sensor points outside the circle were deactivated. This approach helps in speeding up the analysis time for the software. Also, the radius of the circular grid is actually the normalizing 'evaluation radius' or r_{eval}.

5.6 Experimental results

The primary method of experiment was to measure a wavefront of the probe beam without switching on the 808 nm pump (i.e. without any thermal lens) and save the spot-field on the SHWS as a reference. Then the 808 nm pump would be switched on and the current increased in steps up to the normal operating point (~200 W). At each step, aberrations were measured with respect to the reference file. For each step, aberration measurements were averaged over 20-30 snapshots for better accuracy.

For every Nd:YAG head, the pump power was always measured in front of the fiber bundle concerned and a linear calibration curve (pump power vs driving current) was already prepared. Ideally, one should monitor aberrations with the variation of heat power or absorbed pump power. However, knowing the exact amount of absorbed pump power is extremely difficult in the given setup due to the design of the crystal chamber and the pump-double-pass scheme mentioned in sec. 3.3. Hence aberration vs. emitted diode pump power was noted down.

For the ease of understanding, the following experiments can be grouped into two categories: Category I- the experiments with a fixed beam diameter (~ 1040 μm) inside the crystal and varied telescope magnifications (as shown in Fig. 5.7-5.12) ; category II- the experiments where the beam diameter was increased to ~ 1400 μm but a fixed 1:3 telescope was used (Fig. 5.13-5.14). So, the impact of magnification on the accuracy of wavefront analysis could be verified from the category-I experiments. Whereas, after the completion of the category-II experiments, thermal lens power and spherical aberration, as 'seen' by two different probe beam diameters (1040 μm & 1400 μm) but imaged with the same 1:3 telescope, could also be compared.

In the first set of experiments, a 1:1 telescope was used. A planar Gaussian beam was used as reference (in-built reference file with focal spots at the geometric centres of each AOI) and with the increasing pump power the software calculated the focal length of the thermal lens. Note that the focal length of a convex lens and its power are considered to be positive according to the Cartesian sign convention.

The probe beam diameter incident on the crystal was ~1050 μm and so was the size on the SHWS. Note that the FB980-10 band-pass filter was not available for this experiment and an RG850 filter along with an HR1064 / HT976 mirror was used before the SHWS. As described in previously [5.3], the thermal lens power increased linearly with the pump power (i.e. with absorbed pump power). This is shown in Fig. 5.7. The slope was ~ 0.0173 D/W.
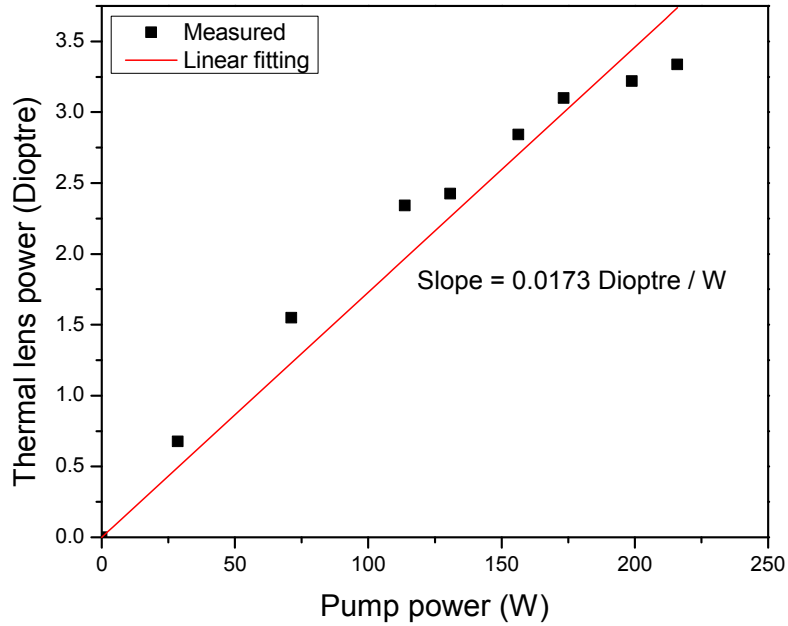
Fig. 5.7 Thermal lens power vs pump power (Probe spot diameter ~ 1050 μm; 1:1 telescope; r_{eval} ~ 1.14237 mm, on the SHWS)

The 1:1 telescope led to an inadequately small beam spot size on the SHWS and as a result, very few lenslets (see Table 5.3) were being used to sample the incident wavefront. This is evident from the slightly scattered points in Fig. 5.7 and also from the better results in the next sets of experiments where the telescope magnification factor ($|m|$) was increased. The probe spot diameter, mentioned in the figure captions, corresponds to the actual size of the 976 nm probe beam inside the crystal. Note that the r_{eval} values on the SHWS, as returned by the software, are presented here in this thesis up to 5 decimal places (in mm). However, given the pixel size of 6.45 μm in the CCD chip concerned, sub-micron level of accuracy of the r_{eval} values is not feasible.

Next, the telescope was re-built with f1=140 mm and f2=200 mm ($|m|$~1.429). Once again the in-built reference file was used. The results are shown in Fig. 5.8. Clearly the increase in beam spot size on the SHWS improved the accuracy of the measurements. The slope was ~ 0.01872 D/W. The linear trend is in excellent agreement with theory, as evident from eqn. 5.1.
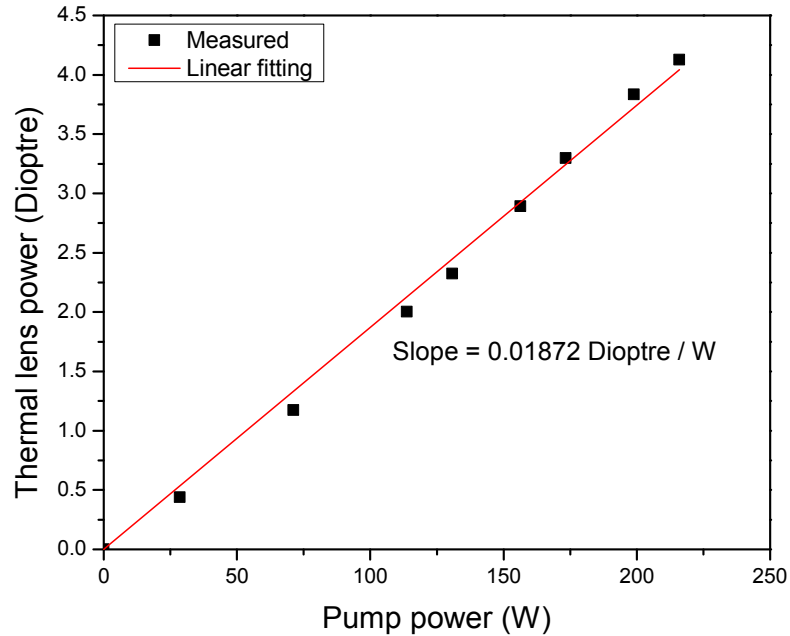
Fig. 5.8 Thermal lens power vs. pump power (Probe spot diameter ~ 1050 μm; 1:1.429 telescope; r_{eval} ~ 2.34787 mm, on the SHWS)

At this point, it was important to verify that the experimental results were sensible enough. Hence the thermal lens power (max ~ 4.1 D) shown in Fig. 5.8 was compared to the simulated results in the ***LZH Rod Designer*** (LRD) program written by Ralph Wilhelm [5.19]. The corresponding simulation showed thermal lens power of 4.42 D at 200 W of pump power. Also, the above mentioned experimental result was compared to the thermal lens power (~ 5 D at 200 W) reported in [5.3] for a similar crystal. Note that the little deviation found in this comparison could be attributed to the slightly different pump optics and a completely different SHWS used in [5.3].

Following the improvement of the previous experiment, a new telescope was built with 1:3 magnification (f1=100 mm, f2=300 mm). The FB980-10 band-pass filter was installed at this stage as shown in Fig. 5.5 (replacing the HR1064/HT976 dichroic mirror). The measured thermal lens power with varying pump power is shown in Fig. 5.9. The slope was ~ 0.02144 D/W and the peak thermal lens power was ~ 4.5 D.
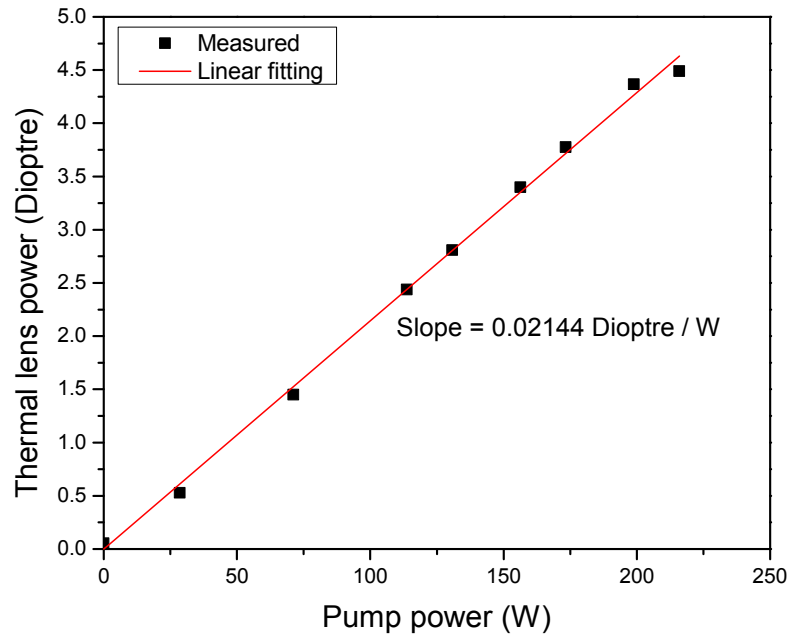
Fig. 5.9 Thermal lens power vs. pump power (Probe spot diameter ~ 1050 μm; 1:3 telescope; r_{eval} ~ 2.65377 mm, on the SHWS)

Note that the slight differences between the slopes shown in Figs. 5.7, 5.8 and 5.9 could be due to several reasons like alignment and change in the number of lenslets used in the SHWS. However, the later measurement with a larger beam and hence with more lenslets could be reasoned to be more accurate.

At this stage, the change in the Zernike spherical aberration coefficient with pump power was also monitored and a linear trend with slope $0.00103\lambda/W$ was measured as shown in Fig. 5.10.
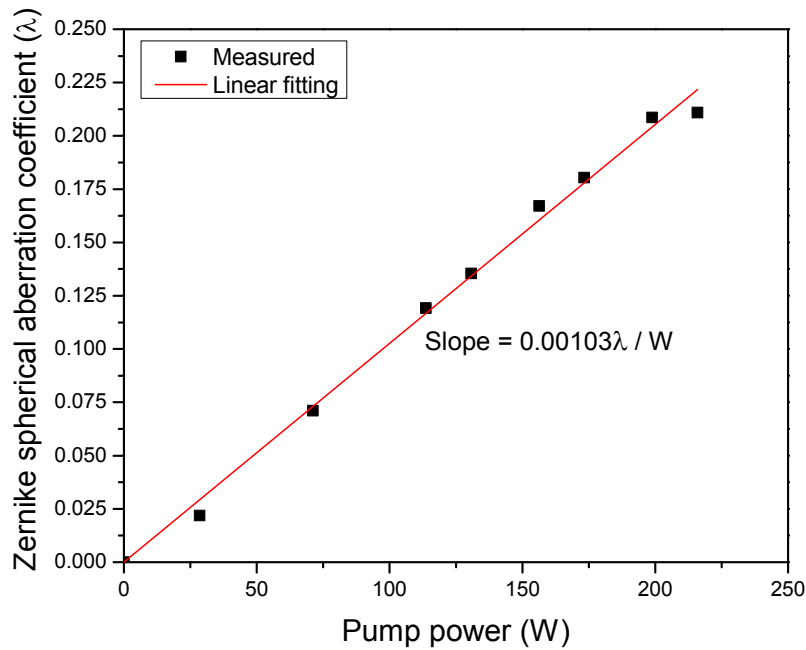
Fig. 5.10 Zernike spherical aberration coefficient vs. pump power
(Probe spot diameter ~ 1050 μm; 1:3 telescope; r_{eval} ~ 2.65377 mm, on the SHWS)

After this experiment, the RG850 filter was removed. It was found that the RG850 filter was causing little bit of distortion in the probe 976 nm beam profile, as the filter was not coated for 976 nm. The FB980-10 band-pass filter was good enough to chop off the unwanted wavelengths and hence the removal of RG850 filter had no impact on the purity of the spectrum on the SHWS.

Note that from this point onwards, instead of using a built-in reference file, the probe profile at zero pump power was always stored and used as the reference and all other profiles (and hence aberrations) were compared to such reference files. This enabled even more precise measurements of various Zernike aberration terms as any aberration due to the telescope would also get cancelled out. With this kind of reference setting, the previous experiments were then repeated (with 1:3 telescope and ~1050 μm (diameter) probe beam inside the crystal). Again the thermal lens power was measured at different pump power levels (see Fig.5.11) and similar results were obtained.
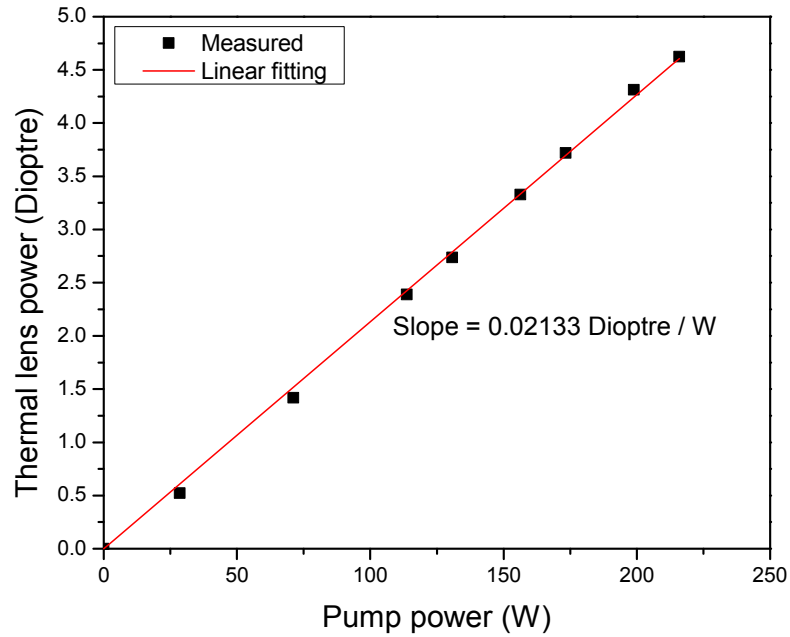
Fig. 5.11 Thermal lens power vs. pump power (RG850 removed; probe spot diameter ~ 1050 µm; 1:3 telescope; r_{eval} ~ 2.65377 mm, on the SHWS)

The plot above confirmed that the RG850 filter did not have a significant impact on the measurement of thermal lens power.

Keeping in mind the actual 1064 nm seed spot size (~ 1500 µm in diameter) inside the crystal under optimum operating condition of the Nd:YAG amplifier system, the 976 nm probe beam spot size inside the crystal had to be increased from 1050 µm as mentioned in the previous experiments. Hence, by changing the collimator in front of the pigtail fiber attached to the 976 nm source, a 1400 µm spot size (diameter) was set for further measurements. Given the lenses available at that moment, 1400 µm spot diameter was the closest possible size to mimic the actual 1500 µm seed diameter. Fig. 5.12 shows the thermal lens power measurement with that 1400 µm probe beam.
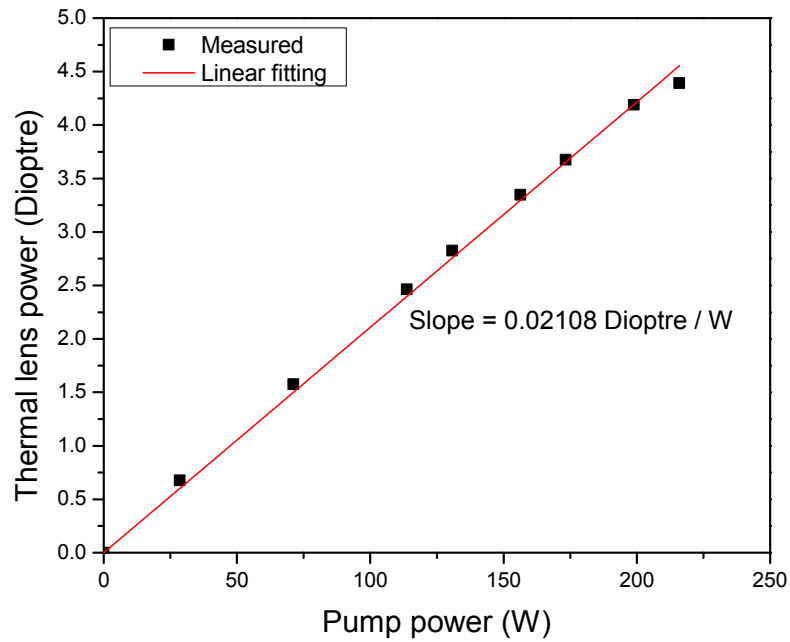
Fig. 5.12 Thermal lens power vs. pump power (Probe spot diameter ~ 1400 μm; 1:3 telescope; r_{eval} ~ 3.24499 mm, on the SHWS)

Notice that with an increased probe beam size, the thermal lens power decreased slightly. It was ~ 4.62 D for a probe beam diameter of ~ 1050 μm but has slightly come down to ~ 4.39 D for the probe beam with ~ 1400 μm diameter. For an ideal spherical lens, one would expect same dioptric power for both the probe beam sizes. Whereas, due to the presence of spherical aberration, the probe beams with different sizes would see different amounts of peak-to-valley (P-V) deviation from the ideal parabolic curvature. The above mentioned experimental results were compared with LRD simulation shown in Fig. 5.13.
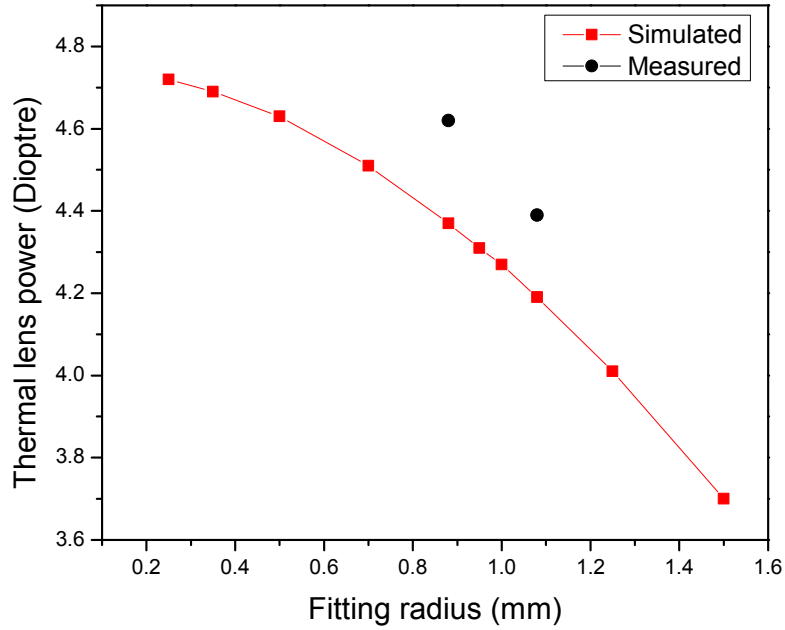
Fig. 5.13 Thermal lens power vs fitting range (pupil radius)

The simulation shows how the dioptric power would change with the fitting range. This 'fitting range' is actually the normalizing pupil radius or evaluation radius (r_{eval}) for Zernike polynomials defined over a unit circle. The simulated trend shown in Fig. 5.13 above could be easily explained by the scaling of Zernike coefficients with r_{eval}, discussed in sec. 5.8.

Fig. 5.13 shows that the simulated dioptric power varies from 4.72 D to 3.7 D for the fitting ranges 0.25 mm and 1.5 mm respectively. The experimentally obtained values of thermal lens power, measured with two different probe beam sizes, could be compared directly to the simulated values as shown in Table 5.4. Since the telescope had a magnification of |m|=3, the actual evaluation radius used in the SHWS was scaled down 1/3 times and used as the evaluation radius in LRD simulation.

Zernike fitting range in Rod designer (mm)	Simulated lens power (D)	r_{eval} on the SHWS (mm)	Measured lens power (D)
1.08	4.19	3.24499	4.39
0.88	4.37	2.65377	4.62

Table 5.4 Comparison of the measured and simulated thermal lens powers for different probe beam sizes

From the Table 5.4, it can be seen that the measured values of the thermal lens power and the corresponding simulated ones are just slightly different. Moreover, 4.37/4.19 ~ 1.043 and 4.62/4.39 ~ 1.052 and the closeness of these two ratios clearly show that the trend followed by the experimental results for two different beam sizes were in excellent agreement with the simulated trend.

Next, the variation of spherical aberration coefficient (C_{40}) was plotted against the pump power and is shown in Fig. 5.14 and a linear trend was observed. This is consistent with the observation made by Martinez in a diode-pumped Nd:YAG laser system [5.4] as well as the observation made by Buske et al. in a CW arc-lamp pumped Nd:YAG MOPA system [5.20]. Contrary to that, a nonlinear variation of C_{40} with heat power (i.e. a fraction of pump power) is also reported in [5.21] for a multi-kW rod type Nd:YAG system with a star shaped pump configuration.

Fig. 5.14 Zernike spherical aberration coefficient vs. pump power
(Probe spot diameter ~ 1400 μm; 1:3 telescope; r_{eval} ~ 3.24499 mm, on the SHWS)

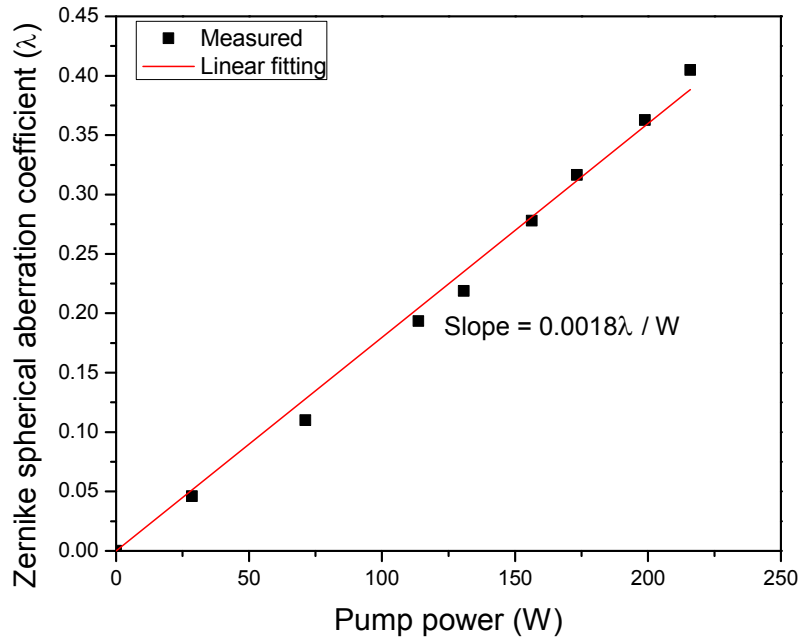Comparing Fig. 5.10 and 5.14, it is clear that the spherical aberration increased with the increased probe beam spot size, as one would expect mathematically by the scaling of Zernike coefficients with r_{eval}, discussed in sec. 5.8.

5.7 Simulations of beam quality degradation due to primary spherical aberration

In order to simulate the TEM_{00} mode content of an aberrated (spherical aberration only) Gaussian beam, first a Gaussian field was defined as:

$$\widetilde{E}_{Gauss}\left(\omega_{Gauss}, A, r\right) = e^{-(r/\omega_{Gauss})^2} \cdot e^{-i \cdot A \cdot \frac{2\pi}{\lambda} \cdot (r/r_{eval})^2}$$

Here ω_{Gauss} is the beam radius (where the peak intensity drops to $1/e^2$), A is an arbitrary constant related to the radius of curvature of the Gaussian wavefront and weighted for the normalizing or evaluation radius, r_{eval}. This r_{eval} is also known as the pupil radius for the Zernike polynomials. Here r is the radial distance from origin and i is the complex square root of -1, as defined by $i^2 = -1$.

Then an aberrated field was defined as follows:

$$\widetilde{E}_{test}\left(\omega_{test}, C_{40,} r\right) = e^{-(r/\omega_{test})^2} \cdot e^{-\frac{2\pi}{\lambda} \cdot i \cdot 6 \cdot C_{40} \cdot (r/r_{eval})^4}$$

Here ω_{test} is the beam waist radius of the test beam, C_{40} is the 3rd order Zernike spherical aberration coefficient (n=4, m=0). Now the fractional TEM_{00} content of the test beam can be obtained by maximizing the value of the following overlap integral with optimum values of the parameters, ω_{Gauss} and A. The parameter A takes care of the best fitting wavefront curvature for the overlap.

$$Overlap, \alpha = \frac{\left| \int_0^{r_{eval}} \widetilde{E}_{Gauss} \cdot \widetilde{E}_{test}^* \cdot rdr \right|}{\sqrt{\int_0^{r_{eval}} \left|\widetilde{E}_{Gauss}\right|^2 \cdot rdr} \sqrt{\int_0^{r_{eval}} \left|\widetilde{E}_{test}\right|^2 \cdot rdr}}$$

The fractional TEM_{00} mode content in the test beam is given by, $\eta_{TEM_{00}} = \alpha^2$

The simulation results obtained using the two sets of experimental values of C_{40} (at maximum pump power levels) are given in Table 5.5.

Probe beam diameter inside the crystal (µm)	Probe beam diameter on the SHWS (µm)	r_{eval} on the SHWS (mm)	C_{40} (µm)	Optimum A	Optimum ω_{Gauss} (µm)	Single stage output $\eta_{\text{TEM}_{00}}$
1050	3200	2.65377	0.1738	0.00065	1530	0.93
1400	4350	3.24499	0.39495	0.0011	1720	0.79

Table 5.5 Simulated degradation of TEM$_{00}$ mode content in a single amplifier stage, due to spherical aberration on Gaussian beams of different waist sizes (experimental data used).

Note that the simulated results in Table 5.5 are valid for the aberration in a single Nd:YAG amplifier stage only. In order to compare the experimental TEM$_{00}$ mode contents of the overall 4-stage Nd:YAG amplifier system, it was required to extend the simulation for the aberration contribution from all the four stages. Assuming an additive effect of aberration from the amplifier stages in series, the same simulation was repeated with 4x times C_{40} values. The simulated results are summarized in Table 5.6. This assumption was based on the fact the seed beam was imaged in between for all the four Nd:YAG amplifier stages.

Probe beam diameter inside the crystal (µm)	Probe beam diameter on the SHWS (µm)	r_{eval} on the SHWS (mm)	C_{40} (µm)	Optimum A	Optimum ω_{Gauss} (µm)	4-stage output $\eta_{\text{TEM}_{00}}$
1050	3200	2.65377	4x 0.1738	0.0013	1130	0.76
1400	4350	3.24499	4x 0.39495	0.0025	1195	0.55

Table 5.6 Simulated overall degradation of TEM$_{00}$ mode content in the 4-stage amplifier, due to spherical aberration on Gaussian beams of different waist sizes (experimental data used).

The TEM$_{00}$ mode contents shown in Table 5.5 are much lower than the experimentally obtained values like 85.4% for a seed beam with 930 µm diameter; and 83.5% for a seed beam with 1500 µm diameter.

Since the use of experimentally obtained Zernike coefficients resulted in impractically small TEM$_{00}$ mode contents in the overlap simulation, the overlap simulations were repeated with the Zernike coefficients simulated in the Rod designer software. Table 5.7 shows both the Zernike defocus coefficient (C_{20}) and spherical

aberration coefficient (C_{40}) simulated for both the 1050 µm and 1400 µm probe beams along with the TEM$_{00}$ mode contents calculated for a single Nd:YAG stage output. The C_{20} values (isotropic, i.e. non-polarization specific) calculated by LRD are also shown in Table 5.7. Note that the r_{eval} values shown in the table are directly scaled down (1/3rd) from the experimentally used evaluation radii or pupil radii on the SHWS. The new overlap calculations with the simulated C_{40} values showed no significant change in the fundamental TEM$_{00}$ mode content at the output of a single Nd:YAG amplifier stage. Whereas, the overlap calculations for the 4-stage amplifier output, showed 98% and 88% TEM$_{00}$ mode contents for the small and large probe beams respectively, as shown in Table 5.8.

Probe beam diameter inside the crystal (µm)	Pupil radius (fitting range) r_{eval} (mm)	Simulated C_{20} (µm)	Simulated C_{40} (µm)	Optimum A	Optimum ω_{Gauss} (µm)	Single stage output $\eta_{\text{TEM}_{00}}$
1050	0.88	-0.84667	0.02398	0.000125	521	1.0
1400	1.08	-1.22140	0.05341	0.002	680	0.99

Table 5.7 Rod designer simulated Zernike coefficients and overlap calculations for a single stage amplifier output

Probe beam diameter inside the crystal (µm)	Pupil radius (fitting range) r_{eval} (mm)	C_{40} (µm)	Optimum A	Optimum ω_{Gauss} (µm)	4-stage output $\eta_{\text{TEM}_{00}}$
1050	0.88	4x 0.02398	0.00035	500	0.98
1400	1.08	4x 0.05341	0.00056	585	0.88

Table 5.8 Rod designer simulated Zernike coefficients and overlap calculations for the 4-stage amplifier output

In case of the overall 4-stage amplifier output, we can argue that the simulated 88% TEM$_{00}$ mode content of the 1400 µm probe beam is comparable with the experimentally obtained 83.5% TEM$_{00}$ mode content for the 1500 µm seed beam. However, it should be kept in mind that in the real experiment the TEM$_{00}$ mode content of the seed beam was ~ 89.5% and not 100%, unlike in the simulation which

assumed an aberration-free 'clean' beam at the beginning. It is also essential to note that the simulations do not take into account the gain saturated amplification, actual beam propagation and interference of the higher order modes.

Nevertheless, one thing is clear from Table 5.5-5.8 that larger beams (seed or probe) would suffer more degradation in beam quality, due to spherical aberration in the end-pumped rod-crystals concerned. This is in agreement with literature [5.4, 5.22, 5.23] where the $\left(M^2\right)^2$ parameter is shown to grow with the 8th power of beam diameter for a constant spherical aberration coefficient. It was already verified experimentally that, with the increase in seed beam radius, the output TEM_{00} mode content degraded, as shown in Fig. 5.15.
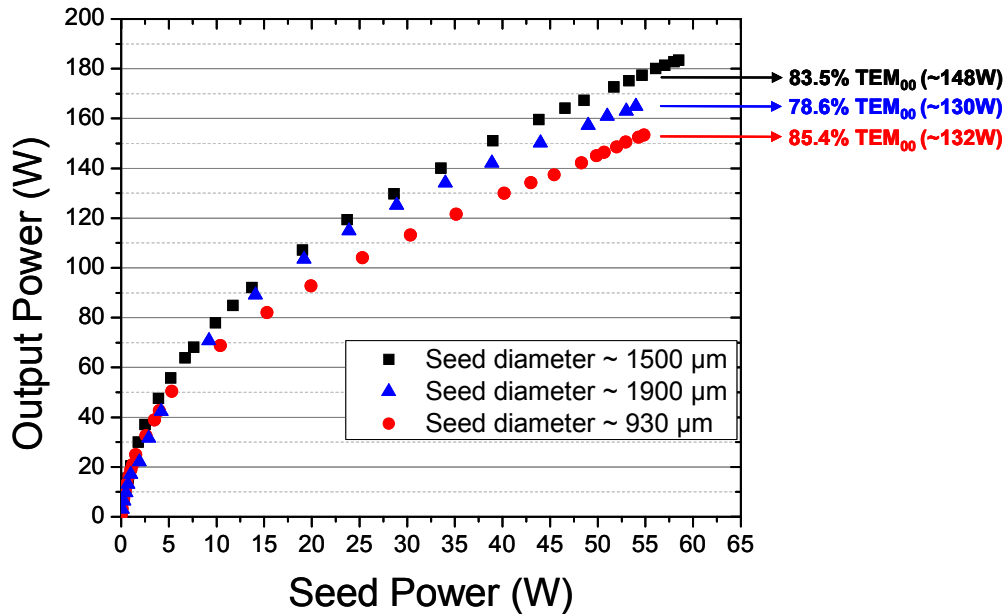
Fig. 5.15 Nd:YAG amplifier system- output beam quality at different seed sizes

As an alternative method of calculation, in case of the ~1400 μm (diameter) probe beam, if we follow Table 5.7 and consider the simulated TEM_{00} mode content out of a single stage and assume identical amount of fractional loss (1% at each stage) to the remaining TEM_{00} mode content in the following 3 stages, the final output would have $\sim (0.99)^4 \approx 96.06\%$ TEM_{00} mode content. Now, keeping in mind the 89.5% TEM_{00} mode content of the actual seed beam, if we multiply 0.895 with

$(0.99)^4$, we get $0.895 \times (0.99)^4 \approx 85.97\%$ TEM$_{00}$ mode content. This is close to the 83.5% TEM$_{00}$ mode content in the 4-stage amplifier output, using 1500 µm seed diameter, as shown in Fig. 5.15. Note that, in this method of calculation, it is assumed that the beam propagation is identical in all the four amplifier stages and the higher order modes do not interact or interfere in a constructive way to enhance the TEM$_{00}$ mode content at any stage. Also it is assumed that the exclusion of higher order modes while calculating the effect of aberration in the following stages does not change the uniformly propagating fundamental mode size chosen initially.

Now, let us consider the $\eta_{\text{TEM}_{00}}$ values for the 4-stage Nd:YAG amplifier system from Table 5.8. We can see that if we multiply the $\eta_{\text{TEM}_{00}}$ values with 0.895, we shall have an estimated $0.98 \times 0.895 \approx 87.71\%$ TEM$_{00}$ mode content for the 1050 µm seed beam; and $0.88 \times 0.895 \approx 78.76\%$ TEM$_{00}$ mode content for the 1400 µm seed beam. Based on these calculations, it can be roughly estimated that the TEM$_{00}$ mode content of the 4-stage amplifier system would be close to or better than 87.71% while using a seed beam of 930 µm diameter (<1050 µm) . On the other hand, the TEM$_{00}$ mode content can not be better than 78.76% while using a seed with 1500 µm diameter (>1400 µm). These calculations can not explain the experimental results shown in Fig. 5.15, especially for the 1500 µm beam and the 1900 µm beam. However, for the seed beam with 1900 µm diameter, one has to keep in mind the almost marginal overlapping with a parabolic pump profile with ~25% background and an effective spot diameter of ~2180 µm (FWHM) as mentioned in sec. 3.4. The overlap of seed and pump modes not only determines the power extraction but also can impact the output beam quality due to radially varying gain distribution.

From the aforementioned findings, it is evident that the approach to calculate TEM$_{00}$ mode content of the 4-stage amplifier output, assuming additive contribution of the C_{40} coefficient (i.e. 4xC_{40} for the whole system) may not be very accurate. Nevertheless, this serves the purpose of a basic qualitative analysis. To achieve better accuracy, the following factors should be taken into account in a rigorous simulation:

a) true beam propagation, b) different gain saturation regimes in the amplifier stages, c) interaction of the higher order modes in the active media.

5.8 Scaling of Zernike coefficients with different pupil radii

It must be noted carefully that even if aberration of the same optical element (e.g. lens) is being characterized by fitting Zernike polynomials, the sets of coefficients obtained by using different normalizing evaluation radii (r_{eval}) are not directly comparable [5.24]. Ophthalmologists often encounter this issue while comparing monochromatic ocular aberrations between two groups of people with different pupil sizes. However, it is shown [5.24] that a set of Zernike coefficients (say, a_{nm}) obtained with a normalizing evaluation radius or pupil radius r_1, can be mathematically scaled and expressed in terms of another set of Zernike coefficients (say, b_{nm}) obtained with pupil radius r_2. In the given context, the following modified equations (Eqn. 5.6, 5.7) are of particular interest. With the fifth order Zernike spherical aberration coefficients (a_{60} and b_{60}) being neglected, these equations are modified versions of the originals in [5.24]. Also, given that the Zernike mode normalizing factors (like $\sqrt{3}$ for defocus, $\sqrt{5}$ for 3rd order spherical aberration) are already embedded in the coefficients provided by the LRD software and the SHWS software (Mr.Beam^{TM}), the constants in the original equations are modified accordingly. So, the following equations hold good for the sets of Zernike coefficients as provided by the LRD and Mr.Beam software.

$$b_{20} = \left(\frac{r_2}{r_1}\right)^2 \cdot \left[a_{20} - a_{40} \cdot 3 \cdot (1 - \left(\frac{r_2}{r_1}\right)^2) \right] \quad \text{Eqn. 5.6}$$

$$b_{40} = \left(\frac{r_2}{r_1}\right)^4 \cdot a_{40} \quad \text{Eqn. 5.7}$$

Now, taking the values of r_1=1.08 mm, a_{20}= -1.22140 μm, a_{40}= 0.05341 μm and r_2= 0.88 mm from Table 5.7 and using the equations above, the estimated $b_{20} \approx 0.846667$ μm and $b_{40} \approx 0.0235428$ μm are in excellent agreement with the already simulated values of 0.84667 and 0.02398 respectively, as shown in Table 5.6.

Although the spherical aberration coefficients experimentally obtained from the SHWS seemed to be quite large, if we apply Eqn. 5.7 with r_1= 3.24499 mm, a_{40}= 0.39495 μm and r_2= 2.653770 mm, the estimated $b_{40} \approx 0.17666$ μm and is surprisingly close to the value 0.1738 obtained experimentally (as shown in Table 5.5). This indicates that these Zernike spherical aberration coefficients given by the SHWS are somehow scaled up by a certain constant multiplier. It was interesting to observe that $\dfrac{0.39495}{3^2} \approx 0.043883$ μm is very close to the corresponding simulated C_{40}=0.05341 μm (for the 1400 μm probe); and $\dfrac{0.1738}{3^2} \approx 0.01931$ μm is very close to the corresponding simulated C_{40}= 0.02398 μm (for the 1050 μm probe). Incidentally, $|m| = 3$ is the magnification of the relay telescope concerned. Neither this kind of scaling of Zernike coefficients with the telescope magnification, nor the very high amount of spherical coefficients given by the SHWS could be readily explained.

5.9 Conclusions

In this chapter, the origin of thermally induced wavefront aberrations in rod type active media has been explained briefly. Analysis of aberrated wavefronts with the help of Zernike polynomials has been explained in detail. The principle of SHWS has been discussed and the modal method of analyzing the discrete data from SHWS has been shown.

It should be noted that the accuracy of the wavefront measurements with the SHWS largely depends on the optical alignment of the probe beam and other optical elements as well as the settings of the measurement tools / parameters (e.g. grid) in the software concerned.

Some experimental results on the thermal lens aberrations of a single stage Nd:YAG amplifier, using a 976 nm probe laser, have been reported. 4f imaging telescopes with different amounts of magnification were tested. Two different probe beam sizes (1050 μm and 1400 μm in diameter) were used for aberration characterization. The measured thermal lens power was found to be closely

comparable with simulated result in every case. Both the Zernike defocus coefficient (C_{20}) and 3rd order or primary spherical aberration coefficient (C_{40}) were found to vary linearly with pump power.

The simulations to estimate the degradation of TEM$_{00}$ mode content due to spherical aberration, both for a single stage and the whole 4-stage amplifier system, were pursued using overlap calculation of an aberrated Gaussian field with a pure Gaussian field distribution with some phase curvature. The C_{40} coefficients obtained experimentally seemed to be much higher in magnitude than expected. Using those experimental values, the overlap calculation showed excessive loss in the TEM$_{00}$ mode contents, which did not match with the experimentally observed TEM$_{00}$ mode contents. Hence the LRD simulated C_{40} coefficients were also tested in the overlap calculations and much more realistic TEM$_{00}$ mode contents were obtained. Given the mode-matching of the seed beam in the 4-stage amplifier system, it was assumed that if the probe/seed beam suffers a certain amount of spherical aberration (given by C_{40}) in one of the amplifier stages, it would suffer 4-times the aberration (given by 4xC_{40}) for the whole system with 4-stages. Although the results obtained from this simple approach were not so accurate in comparison to the experimental results, this approach could still be used qualitatively. Also, the simulation showed a trend that beam quality degradation would scale up with seed spot size, which had been previously reported by several authors [5.4, 5.22, 5.23]. For a better estimation of beam quality degradation in the amplifier system, rigorous simulation considering the true beam propagation throughout the system and spatial gain distribution in the Nd:YAG crystals will be necessary.

The scalability of Zernike coefficients obtained from different pupil sizes is discussed in this chapter. The Zernike coefficients obtained from the LRD simulations as well from the experiments, for two different probe beam sizes (and hence different pupil sizes), were found to be very accurately scalable in accordance with the mathematical treatment given in [5.24].

References Ch.5

5.1) C Pfistner, R Weber, H P Weber, S Merazzi, and R Gruber, "Thermal Beam Distortions in End-Pumped Nd:YAG, Nd:GSGG, and Nd:YLF Rods"; IEEE Journal of Quantum Electronics, Vol. **30**, No. 7, 1994, p 1605-1615

5.2) W A Clarkson, "Thermal effects and their mitigation in end-pumped solid-state lasers"; J. Phys. D: Appl. Phys. **34** (2001), p 2381–2395

5.3) O Puncken, "Pumpkopfdesign für den Advanced LIGO Laser"; PhD Thesis 2011, Leibniz Universität Hannover; Cuvillier Verlag Göttingen 2011, ISBN 978-3-86955-967-4

5.4) A V Martínez, "Measurement and analysis of aberrations in high power Nd:YAG lasers", PhD thesis 2001, Technische Universität Berlin; dissertation.de-Verlag im Internet GmbH, ISBN 3-89825-340-6

5.5) W Koechner, "Solid-State Laser Engineering (Springer Series in Optical Sciences)"

5.6) W Koechner, "Thermal Lensing in a Nd:YAG Laser Rod"; Applied Optics, Vol. **9**,1970, p 2548-2553

5.7) C Pfistner, R Weber, H P Weber, S Merazzi, and R Gruber, "Thermal Beam Distortions in End-Pumped Nd: YAG**,** Nd: GSGG, and Nd : YLF Rods"; IEEE Journal of Quantum Electronics, Vol. **30**,1994, p 1605-1615

5.8) H J Eichler, A Haase, R Menzel and A Siemoneit, "Thermal lensing and depolarization in a 1 highly pumped Nd:YAG laser amplifier"; Journal of Physics. D Appl. Phys. **26** ,1993, p 1884-1891

5.9) Web resource: Encyclopedia of Laser Physics and Technology, URL: http://www.rp-photonics.com/yag_lasers.html

5.10) P H Klein and W J Croft, "Thermal Conductivity, Diffusivity, and Expansion of Y2O3, Y3 Al5O12, and LaF3 in the Range 77°–300°K"; Journal of Applied Physics Vol. **38**, 1967, p 1603-1607

5.11) T Y Fan and J L Daneu, "Thermal coefficients of the optical path length and refractive index in YAG"; Applied Optics, Vol. **37**, 1998, p 1635-1637

5.12) V N Mahajan, "Optical Imaging and Aberrations, Part II. Wave Diffraction Optics", (SPIE Press Monograph Vol. PM209), ISBN-10: 081948699X

5.13) N Hodgson and H Weber, "Influence of Spherical Aberration of the Active Medium on the Performance of Nd: YAG Lasers", IEEE Journal of Quantum Electronics, Vol. **29**, NO. 9, September1993, p 2497-2507

5.14) L D Bores, "Refractive eye surgery", Wiley-Blackwell 2001

5.15) S K Saha, "Diffraction-limited imaging with large telescopes and moderate",World Scientific Publishing Co Pte Ltd. 2007

5.16) R J Mathar, "Zernike basis to Cartesian transformations"; Serb. Astron. J. **179** (2009), 107 - 120, p 107-120

5.17) D R Neal, J Copland, D Neal, "Shack-Hartmann wavefront sensor precision and accuracy"; Advanced Characterization Techniques for Optical, Semiconductor, and Data Storage Components, Proceedings of SPIE Vol. **4779** (2002), p 149-160

5.18) I Buske, "Aberrationen in Nd:YAGHochleistungslasern und -verstärkern:

Ihr Einfluss und ihre Korrektur mit adaptiver Optik," PhD Thesis,2005, Technischen Universität Berlin,

URL: opus.kobv.de/tuberlin/volltexte/2005/1062/pdf/**buske**_ivo.pdf

5.19) R Wilhelm, D Freiburg, M Frede, D Kracht and C Fallnich, "Design and comparison of composite rod crystals for power scaling of diode end-pumped Nd:YAG lasers," Optics Express, Vol. 17, 2009, p 8229-8236

5.20) I Buske, H M Heuck, P Welp and U Wittrock, "Aberrations of a Master-Oscillator-Power-Amplifier Laser with Adaptive Optics Correction", Adaptive Optics For Industry and Medicine, Springer Proceedings in Physics, 2005, Vol. **102**, Part III, 250-259, DOI: 10.1007/3-540-28867-8_26

5.21) E Leibush, S Jackel, S Goldring, I Moshe, Y Tzuk, and A Meir, "Elimination of spherical aberration in multi-kW, Nd:YAG, rod pump-chambers by pump-distribution control", Advanced Solid-State Photonics, Technical Digest (Optical Society of America, 2005), paper MB45

5.22) J Alda, J Alonso and E Bernabeu, "Characterization of aberrated laser beams"; Journal of Optical Society of America A, Vol. **14**, 1997, p 2737-2747

5.23) A E Siegman, "Analysis of laser beam quality degradation caused by quartic phase aberrations"; Applied Optics Vol. **32**, p 5893-5901, 1993

5.24) J Schwiegerling, "Scaling Zernike expansion coefficients to different pupil sizes"; Journal of Optical Society of America A, Vol. **19**, 2002, p 1937-1945

Ch.6 Conclusions and Outlook

6.1 Conclusions

The Michelson interferometer (MI) based gravitational wave detectors (GWD) demand highly stable single frequency linearly polarized laser sources with very high TEM_{00} mode contents. As a scalable alternative to the state-of-the art injection locked aLIGO laser systems commissioned at the LIGO observatories, a high power solid state single frequency master oscillator power amplifier (MOPA) system was built and characterized within the scope of this PhD thesis. The MOPA system comprises a commercial non planar ring oscillator (NPRO) with 2 W of output power, a pre-amplifier system with six $Nd:YVO_4$ based stages and 72 W of output power with $\sim 89.5\%$ TEM_{00} mode content, and the main amplifier system with four identical Nd:YAG based stages. The $Nd:YVO_4$ and Nd:YAG crystals are end-pumped by 808 nm diode modules. All the rod type (diameter 3 mm) Nd:YAG crystals were pumped at ~ 200 W of power level. Depolarization was efficiently minimized in the Nd:YAG amplifier system by using a pair-wise (1st & 2nd stage; 3rd & 4th stage) depolarization compensation scheme with 4f imaging lenses and 90° quartz rotators. The whole MOPA system was designed for a single pass of the seed beam. At a seed power of ~ 60 W and seed diameter of ~ 1500 μm, a linearly polarized output power of ~ 177 W at 1064 nm, with $\sim 83.5\%$ TEM_{00} mode content was achieved from the main amplifier system. Since the contemporary MI based GWDs can utilize TEM_{00} mode only, and a typical M^2 measurement does not convey any information on the exact TEM_{00} mode content, the mode content measurements were carried out with the

help of a very specialized instrument based on a non-confocal triangular ring resonator.

The amplifier system was characterized at three different Gaussian seed sizes (diameters $\sim$ 930, 1500 and 1900 μm). The gain saturation characteristics of the system were observed experimentally at all the seed sizes. In order to investigate the impact of gain saturation related spatially varying gain profile on the beam quality of a Gaussian seed beam, a simulation was performed. It was found that gain saturation was not responsible for the degradation of TEM_{00} mode content in the amplifier output ($\sim$ 83.5% for ~1500 μm seed diameter) while compared to that of the seed ($\sim$ 89.5%). Hence, it clearly reinforced the intuitive explanation of beam quality degradation due to thermally induced aberrations that would be investigated later.

Noise is a critical issue for the GWD. Without proper noise suppression of the laser sources down to certain levels, no detector can possibly detect the faint gravitational waves reaching earth. Hence relative intensity noise (RIN) measurements were performed at the NPRO output, at the pre-amplifier output and at the amplifier output and compared, over a range 1 Hz-100 kHz. The pump light RIN in the Nd:YAG amplifier system was also characterized. The influence of pump light RIN in the low frequency regime (1 Hz to a few hundred Hz) was clearly observed. In the higher frequency regime, the amplifier output RIN was dominated by the seed RIN, as expected from theory. Variation of the output RIN with seed power has been experimentally observed in both the pre-amplifier system and the amplifier system. It was found that the output RIN was highest at the lowest seed power level. In the Nd:YAG based amplifier system, the RIN at low seed power exhibits with a 'bumpy' rise in the 100 Hz- 5 kHz range (logarithmic-logarithmic scale). This could be a vague indication to some kind of corner frequency around $\sim$ 2 kHz but the reason was not clear. Nevertheless, one interesting aspect of the RIN characterization was to compare the MOPA RIN with that of the aLIGO laser system. Although the MOPA system and the injection locked aLIGO laser system are quite different in principle, the RIN characterization of the MOPA system, performed at 160 W linearly polarized output power level, showed a similar noise spectrum to that of the free running (non-

stabilized) aLIGO laser system, in the 1 Hz-100 kHz range. This finding is very promising as, in principle, the MOPA system can also be stabilized by the same acousto-optic modulator (AOM) based beam stabilization scheme as applied to the aLIGO laser system. Apart from the thorough experimental RIN characterization, a simulation was performed to understand the pump and seed noise transfer onto the amplifier output RIN. It was understood that the amplifier output RIN could not be attributed to the pump and seed RINs only and rather some additional sources of noise should also be taken into account and investigated further. It has been hypothesized that one such possible source of additional noise could be the spectral fluctuations in the pump light source, which can affect the gain and hence the output RIN.

Thermally induced aberrations in the Nd:YAG amplifier system were experimentally studied using a commercial Shack-Hartmann wavefront sensor (SHWS). A 976 nm diode laser source was used as a probe. The measurements of thermal lens power at the standard ~ 200 W of pump power level was found to be in good agreement with simulations. More importantly, the primary spherical aberrations were measured at different probe beam sizes, using 4f imaging telescopes with different magnifications. The absolute experimental Zernike spherical aberration coefficients (C_{40}) were found to be higher than the simulated values. However, the trend of variation with probe beam size matched well with the simulated trend. Although, it was clarified by the manufacturer of the SHWS that telescope magnification does not impact the Zernike coefficients, when the Zernike spherical aberration coefficients were divided by the square of magnification concerned, the resulting values were found to be very close to the simulated ones. This could not be explained. Using the simulated spherical aberration coefficients, estimation of TEM_{00} mode contents of the aberrated beams were performed through overlap integration calculations involving pure Gaussian electric fields. These results were compared with the measured TEM_{00} mode contents. However, it has to be kept in mind that the overlap integration calculation starts with the assumption of a beam with 100% TEM_{00} mode content that goes through some aberrations. In reality, the amplifier

system was seeded by a beam with ~ 89.5% TEM_{00} mode contents. Nevertheless, the simple model, which did not take into account the variation of seed size beam propagation and gain saturated amplification, was qualitatively verified. Furthermore, the scaling of Zernike coefficients with pupil size, something that has been primarily known to ophthalmologists through scientific literature [6.1] for a decade now (see sec. 5.8), was shown to be the reason behind the variation of thermal lens power with probe beam size. Such scaling was also verified in case of Zernike spherical aberration coefficients obtained through experiments as well as from a simulation software (LZH Rod Designer) that calculates the thermal lens [6.2]. To the best of my knowledge, the validity and significance of such scaling of Zernike coefficients with pupil size, in the context of thermal lens characterization of an end pumped Nd:YAG amplifier system has been shown for the first time.

6.2 Outlook

In future, different pump optics can be used for the Nd:YAG amplifier in order to investigate aberrations further. For a better understanding of the evolution of aberrations in the chain of amplifiers, a mode cleaner cavity can be used in the seed line so that the amplifier sees a purer TEM_{00} mode content (close to 100%) than the one used in the experiments (with ~ 89.5% TEM_{00} mode content). Even without using the mode cleaner, the output from the NPRO with ~ 97% TEM_{00} mode content can be directly seeded to the amplifier system. However, given the low power of the NPRO (2 W), the power extraction from the Nd:YAG stages would be minimal. Hence the thermal load and thermal lensing would be higher than in case of the normal operating point with a high power seed (~ 60 W). Along with the existing system, two more identical Nd:YAG stages can be added to investigate whether the power scaling comes at the cost of significantly higher aberrations and degradation of TEM_{00} mode content. This will probably determine whether it will be useful to proceed with the same architecture of Nd:YAG stages for further power scaling or develop a better design. For further power scaling, the Nd:YAG amplifier system can also be seeded with an existing single frequency fiber MOPA offering 246 W of output power [6.3].

Frequency noise characterization of the MOPA system should also be performed, which has not been possible so far due to the unavailability of suitable electronics and lack of time as well. For a proper pump noise transfer characterization suitable current modulators will be required. Apart from the seed noise and pump noise, nature of other noise sources should be investigated. For an example, the spectral fluctuations of the pump light source can be monitored by using a high resolution diffraction grating and subsequent monitoring of relative variation of intensity in two distinct ordered diffraction maximas, simultaneously. The most interesting thing would be to investigate the 'bumpy' rise in the amplifier output RIN at low seed power in the ~ 100 Hz- 5 kHz range (logarithmic scale), something that was not observed in the pre-amplifier (block B) and could not be explained.

Apart from the designated operation of the Nd:YAG amplifier system at 1064 nm, generation of other wavelengths (946 nm) in an oscillator configuration will be very interesting from a scientific perspective. This will require different crystal coatings and change in optics. However, given the amount of pump power (~ 800-1000 W) readily available to the system (at 808 nm), achieving a very high power 946 nm lasing is highly feasible. Furthermore, a second harmonic generation scheme can be implemented for a high power output at visible 473 nm. Generation of 938.5 nm and subsequent frequency doubling to generate ~ 469.2 nm are also feasible, keeping in mind the efficient pumping of Pr^{3+} doped materials at 469 nm [6.4].

References Ch.6

6.1) J Schwiegerling, "Scaling Zernike expansion coefficients to different pupil sizes," Journal of Optical Society of America A, Vol. 19, 2002, p 1937-1945

6.2) R Wilhelm, D Freiburg, M Frede, D Kracht and C Fallnich, "Design and comparison of composite rod crystals for power scaling of diode end-pumped Nd:YAG lasers," Optics Express, Vol. 17, 2009, p 8229-8236

6.3) M Karow, C Basu, D Kracht, J Neumann and P Weßels, "TEM_{00} mode content of a two stage single-frequency Yb-doped PCF MOPA with 246 W of output power," Optics Express, Vol. 20, 2012, p 5319-5324

6.4) B Xu, P Camy, J-L Doualan, A Braud, Z Cai, F Balembois and R Moncorgé, "Frequency doubling and sum-frequency mixing operation at 469.2, 471, and 473 nm in Nd:YAG," Journal of the Optical Society of America B, Vol. 29, 2012, p 346-350

List of publications:

Contributions to peer-reviewed conference proceedings

1) J K Sahu, S Yoo, A Boyland, C Basu, M Kalita, A Webb, C L Sones, J Nilsson, D N Payne , "488 nm Irradiation Induced Photodarkening Study of Yb-Doped Aluminosilicate and Phosphosilicate Fibers," JTuA27, CLEO-2008.

2) C Basu, S Yoo, A J Boyland, A S Webb, C L Sones, J K Sahu, "Influence of temperature on the post-irradiation temporal loss evolution in Yb-doped aluminosilicate fibers, photodarkened by 488 nm CW irradiation," CJ1_2, CLEO-Europe & EQEC 2009, Munich, Germany (*Oral presentation*)

3) C Basu, O Puncken, L Winkelmann, P Weßels, J Neumann and Dietmar Kracht, "Development of a solid state laser amplifier source for the third generation of gravitational wave detectors," CA5_3, CLEO Europe & EQEC 2011, Munich, Germany.(*Oral presentation*)

4) M Karow, C Basu, D Kracht, J Neumann, and P Wessels, "Single-frequency Yb-doped PCF MOPA with 294 W of output power for gravitational wave detection," CJ7_4, CLEO Europe & EQEC 2011, Munich, Germany

5) C Basu, O Puncken, LWinkelmann, M Frede, B Schulz, P Weßels, J Neumann, D Kracht; Single Frequency Solid State Laser Amplifier System: Towards 3rd Generation of Gravitational Wave Detectors: 5620-CT-3, IQEC/ CLEO Pacific Rim 2011, Sydney, Australia. (*Oral presentation*)

Contributions to peer-reviewed journals

1) P K Datta**,** C Basu, S Mukhopadhyay, S K Das, G K Samanta and A Agnesi, "Diode array pumped, nonlinear mirror Q-switched and mode-locked Nd:YVO4 laser – a good tool for powder SHG," Pramana-Journal of Physics, Indian Academy of Sciences, vol.**63**, 2004

2) S Yoo, C Basu, A J Boyland, C Sones, J Nilsson, J K Sahu, and D Payne, "Photodarkening in Yb doped aluminosilicate fibers induced by 488 nm irradiation," Optics Letters, Vol. **32**, 2007

3) M Karow, C Basu, D Kracht, J Neumann and P Weßels, "TEM00 mode content of a two stage single-frequency Yb-doped PCF MOPA with 246 W of output power," Optics Express, Vol. **20**, 2012, p 5319-5324

4) C Basu, P Weßels, J Neumann and D Kracht, "High Power Single Frequency Solid State MOPA for Gravitational Wave Detection," Optics Letters, doc. ID 166988 (posted on 1st June 2012, in press).

Curriculum Vitae

Name: Chandrajit Basu

Nationality: Indian

Schooling:

Alipurduar High School, West Bengal, India

College & University:

(2001-2006) Integrated M.Sc in Physics (5 year program; Bachelors and Masters-combined)

at the Indian Institute of Technology (IIT), Kharagpur, India.

(2006-2008) M.Phil in Optoelectronics, University of Southampton, United Kingdom

(M.Phil degree conferred in 2011).

(2009-2012) Doctoral research at the Laser Zentrum Hannover e.V. and QUEST-Centre for Quantum Engineering and Space-Time Research, Leibniz University Hannover.

Work / Research Experience:

2003 Summer Intern at the Laser Laboratory, Dept. of Physics & Meteorology, IIT Kharagpur

2004 PPARC funded International Summer School on Astronomy & Particle Physics, University of Durham, United Kingdom.

2005 Summer intern at Avisere Technology Pvt. Ltd, Kolkata, India

(2006-2008) Post-graduate research student (with full scholarship) at the Optoelectronics Research Centre (ORC), University of Southampton, United Kingdom.

2007 optETH Winter School in Biophotonics at ETH Zurich, Switzerland.

(2007-2008) Lab demonstrator and tutor (part-time), Department of Physics, University of Southampton, United Kingdom.

(2007-2008) Club Ambassador (post-graduate student representative to the ORC graduate board), OSA student chapter, University of Southampton, United Kingdom.

(2007-2008) Sub-warden (part time) at a University hall of residence, Business & Community Services, University of Southampton, United Kingdom.

(2009-2012) Scientific staff (pursuing a PhD project with full scholarship from QUEST, Hannover) at the Laser Zentrum hannover e.V.

Professional membership:

Member- IEEE

Acknowledgements

First of all, I'm thankful to the cluster of excellence, QUEST-Centre for Quantum Engineering and Space-Time Research, Hannover for funding me with a full 'stipendium' to pursue this PhD program.

I express my sincere gratitude to my supervisor, Prof. Karsten Danzmann and my co-assessor, Prof. Uwe Morgner.

I'm extremely grateful to Dr. Peter Weßels, Laser Zentrum Hannover (LZH), for his constant support, mentoring and scientific guidance. His patience to address my innumerable scientific queries was unparalleled and our regular scientific discussions played a key role in the completion of this thesis.

Thanks to Laser Zentrum Hannover, a partner institute of QUEST, for providing me with excellent laboratory facilities and a stimulating work environment. I would like to thank my colleagues at the *Laser Development Department (Abt. EW)* at the LZH for their incessant helpfulness. Special thanks to Dr. Dietmar Kracht, the Director of the LZH and Dr. Jörg Neumann, the Head of the *Laser Development Department*, for their constant support and cooperation.

I'll cherish the experience of working in the *Single Frequency Lasers* (SFL) *group* because of the friendly and helpful group mates, Dr. Oliver Puncken, Dr. Lutz Winkelmann, Mr. Henrik Tünnermann, Mr. Malte Karow, Dr. Vincent Kuhn, Mr. Raphael Kluzik and Mr. Marcin Damjanic. Thanks to all of them and also to my former colleague, Dr. Daniel Sauder who helped me a lot while setting up the lab. Daniel is also remembered thankfully for the painstaking efforts in order to help me with all the mandatory paper works, ranging from the registration at the university to residence permit, on my arrival in Hannover. I would like to thank my friend and former colleague, Mr. Rajat Marwah for his moral support since I joined the PhD program.

I'm grateful to Dr. Maik Frede and Mr. Bastian Schulz at neoLASE GmbH for the invaluable technical and scientific inputs they provided.

Dr. Oliver Puncken is thankfully acknowledged for translating the abstract into Deutsch. I'm grateful to him for enormous help and support throughout.

Special thanks to Ms. Birgit Ohlendorf at QUEST and Ms. Gabi Herold and Ms. Sylvia Gerber at the LZH for their invaluable help in official paper works and beyond.

Within my personal sphere, I would like to thank my parents, grand parents and my friends who inspired and supported me greatly. I'm grateful to my father who motivated me for technical and scientific research through hands-on training in electronics during my childhood and am grateful to my grandpa who funded my 'crazy projects' at home.

I would like to thank my former mentor, Prof. P K Datta, Dept. of Physics & Meteorology, IIT Kharagpur who introduced to me the fascinating world of lasers and also recommended me for this PhD program.

Special thanks to my friend, Ms. Debanjana Chatterjee for being a constant source of encouragement and moral support.